# Chaotic Transport in Phase Space with Applications to Atomic Physics

by

Korana Burke

B.A. (University of California Berkeley) 2002

A dissertation submitted in partial satisfaction of the
requirements for the degree of
Doctor of Philosophy

in

Physics

in the

GRADUATE DIVISION
of the
UNIVERSITY OF CALIFORNIA, MERCED

Committee in charge:
Jay Sharping, Chair
Kevin A. Mitchell
Michael Scheibner
Boaz Ilan

Spring 2011

The dissertation of Korana Burke is approved:

_____

Chair                                                          Date


_____

Date


_____

Date


_____

Date



University of California, Merced


Spring 2011

**Chaotic Transport in Phase Space with Applications to Atomic Physics**

Copyright 2011

by

Korana Burke

# Abstract

Chaotic Transport in Phase Space with Applications to Atomic Physics

by

Korana Burke

Doctor of Philosophy in Physics

University of California, Merced

Jay Sharping, Chair

Chaotic behavior appears in numerous complex systems. It plays a fundamental role in many scientific problems such as the motion of asteroids, the formation of weather patterns, population growth, and even in the firing of neurons. It is characterized by a behavior that to the naked eye appears to be random and unpredictable, but is in fact deterministic. Since it is hard to isolate a chaotic system from random interactions with the environment, the challenges in studying its behavior are both mathematical and experimental. In recent years, atomic gasses have emerged as experimentally accessible systems for observing chaos under controlled conditions. The research in this thesis focuses on the study of chaotic transport in phase space applied to the analysis of ionization in two different atomic systems. The first system consists of an atom exposed to periodic alternating positive and negative external electric field pulses, and the second system consists of an atom placed in constant external electric and magnetic fields. The main

goal of this thesis is to develop a connection between the general mathematical constructs of a dynamical system, and an atomic experiment. As such, this research acts as a bridge between the areas of applied math and experimental physics.

The theoretical results in this research are based on the observation that the ionization of an atom is caused by an underlying geometric structure of phase space that acts as a turnstile which promotes the electron from negative energy (bound) to positive energy (ionized). The turnstile is contained in the Poincaré surface of section, and its position, size, and shape all depend on the parameters of a given chaotic system. Understanding this relationship allows one to draw conclusions about the ionization process.

The major goal of this research is to provide guidance in designing atomic experiments in which one can observe classical chaos effects. The focus of this thesis is on the study of chaotic ionization, but this work also includes novel techniques that can be applied to numerous other phenomena such as trapping, focusing and steering electronic wave packets into desired regions of phase space.

<div style="text-align: right;">

_____

Jay Sharping
Dissertation Committee Chair

</div>

In loving memory of my grandma Katica Škovrlj

To John

# Contents

# List of Figures

# List of Tables

# Acknowledgments

To be included...

# Chapter 1

# Introduction

Roughly three hundred years ago Isaac Newton started using differential equations to describe time evolution of physical systems. He observed that motion of a system at a given time can be connected to its motion at any earlier time via a smooth mathematical function. This led him to believe that the equations of motion would also change smoothly as the initial conditions are varied. He was convinced that the solutions to differential equations describing time evolution of a physical system were analytic functions of both the time and the initial conditions. The idea of a "clockwork universe", where every motion is completely determined by its initial conditions and moves along a smooth path for the rest of the time, was fully adopted by scientists and persisted for a very long time. By improving on Newton's techniques, Lagrange and Hamilton developed their own analytical techniques for finding the equations of motion of a particular physical system. Scientists of the eighteenth and nineteenth century hoped that every mechanical problem could be solved analytically, and they believed that if the analytic solutions to a particular

problem could not be found, it was because a more clever or sophisticated approach still needed to be discovered. This belief persisted until the late nineteenth century when Henri Poincaré, a French mathematician and physicist, proved otherwise.

One of the major problems faced by scientists of that time was a famous three body problem. The solutions for the motion of two bodies in a gravitational potential were well known, but the addition of a third body presented a major challenge. The importance of finding the solution to the three body problem was considered so great that in 1887, in honor of his 60th birthday, Oscar II, King of Sweden, offered a prize of $2,500$ crowns for anyone who could find its solution. Poincaré won the prize by showing that there are no analytic solutions in even simpler problem where the mass of a third body is too small to affect the motion of the remaining two bodies. Later in 1892, Poincaré made an observation that small differences in the initial conditions can produce great differences in the final phenomena. In reaching this conclusion, he discovered deterministic chaos. Due to great advances in quantum mechanics and relativity, Poincaré's discovery was mainly ignored by the physics community until the 1960s when it was rediscovered by computer experiments on systems of differential equations that even the solutions to very simple systems are capable of being sensitive to initial conditions. It was not until 1975 and the paper by James Yorke that the term "chaos" was used to describe these systems [27]. These days chaotic systems are studied in a wide range of disciplines such as physics, applied math, meteorology, chemistry, biology, and even social and finance fields. The work presented in this thesis concerns the study of transport and escape in chaotic systems with a particular focus on the problem of chaotic ionization in atomic systems.

## 1.1   Poincaré return map and surface of section

Scientists now understand that many interesting systems have no analytic solutions and in response they have adopted a variety of different ways to study these systems. One approach, originally introduced by Poincaré, is to reduce a continuous system to a discrete one. If the system is periodic with period $t'$, the simplest way to do this reduction is by taking stroboscopic snapshots in time of the system, and recording the position and momenta coordinates. This creates a map $M$, called a Poincaré return map, which is defined as

$$(\vec{r}(t), \vec{p}_r(t)) \mapsto M(\vec{r}(t), \vec{p}_r(t)) = (\vec{r}(t+t'), \vec{p}_r(t+t')),$$

where $t'$ denotes the separation between two snapshots. We adopt this definition of the Poincaré return map in the system described in Chapters 2, 3, 4, and 5. In systems that are not periodic in time, a common way to define the Poincaré return map is to pick a line or a plane in space and record the position and momentum values at the moment when a trajectory crosses a chosen line or punctures a chosen plane. We adopt a version of this definition in Chapter 6. Hence instead of recording the positions and momenta of all the possible trajectories allowed in a system at a particular time, one records the phase space coordinates at a particular region in space.

More generally, Poincaré return map is defined as the intersection between the orbit in the full dimensional phase space with a surface of a lower dimension, called the Poincaré surface.

The main challenge in defining an appropriate Poincaré return map for a given

system is choosing the correct Poincaré surface. It is important to pick a surface such that every orbit in the system crosses the surface infinitely many times, and that these crossings are transverse, i.e. the orbits "pierce" the surface and do not bounce off it.

A surface of section (SOS) is then defined as an $(n-1)$-dimensional representation of trajectories in an $n$ dimensional system. An important property of a Poincaré return map is that for Hamiltonian systems it is an area preserving map, meaning that the phase space area is preserved as a function of time. This is an important fact used when studying time evolution of Hamiltonian chaos and can be proved using the Liouville's theorem.

## 1.2 KAM tori and fixed points

A fixed point (also known as a stationary point, equilibrium point, or a critical point) of a discrete dynamical system is a point that under Poincaré return map maps to itself, i.e., it is the point that is stationary in the SOS plot. A fixed point of a discrete system is an equivalent to a periodic orbit of a continuous system. Furthermore, there exist points that map back to themselves after $N$ applications of a Poincaré return map. These points are called period-$N$ fixed points and together with fixed points they are used to study various time dependent behaviors of a given chaotic system.

Figure (1.1) shows an example of a SOS plot for a kicked Rydberg system. (Detailed study of this system is included in Chapters 2, 3, 4, and 5.) In most Hamiltonian systems for some initial conditions it is possible to observe smooth, invariant curves in the SOS. Sometimes it is even possible to find explicit analytic expressions describing these curves, but even in the case when this is not possible, the orbit that starts on one of these
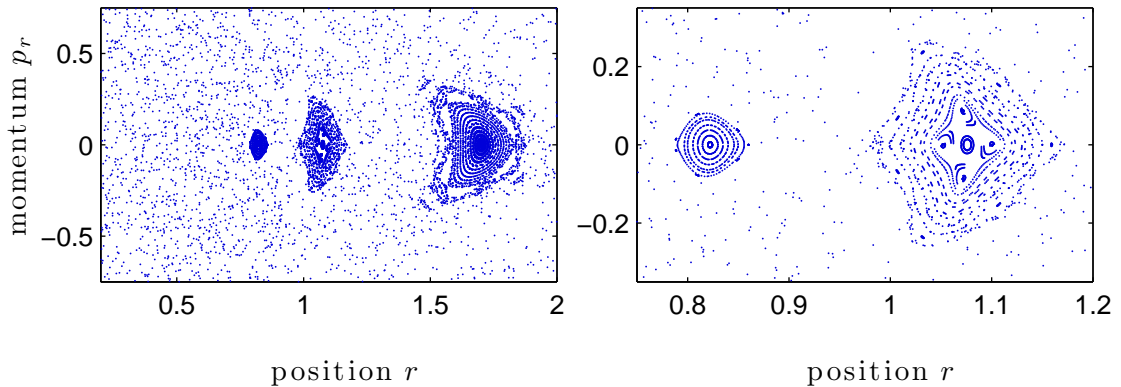
Figure 1.1: Examples of SOS plot for kicked Rydberg system.

curves, will remain on that curve forever or until the dynamics of the system changes. These invariant curves are known as Kolmogorov - Arnold - Moser (KAM) tori, and are also commonly referred to as stable islands. They are important objects because they form a barrier to transport in phase space, meaning that a trajectory that starts on one side of the stable island will never cross to the other side of the island. A few examples of stable islands are shown in Fig. (1.1). Some of the initial conditions used to create this data produced islands that can be observed as closed curves in the SOS plot. A portion of the remaining initial conditions produced islands that can be observed as voids in the SOS plot because they started outside the islands, while a different portion that started inside the island produced islands that can be observed as increased density of points in the SOS plot. The remainder of the SOS plot is populated by chaotic sea whose signature can be observed by a roughly uniform distribution of points.

Increasing the amount of chaos in the system by increasing the size of the perturbation to the nonchaotic Hamiltonian, causes some KAM tori to dissolve, and others to

change size. This process is described by the KAM theorem which states that the KAM tori that have not been destroyed by the perturbation occupy a finite area in SOS.

When the last stable island is dissolved by the perturbation, we need to define additional machinery to understand barriers to transport in phase space.

## 1.3    Stability of fixed points and homoclinic/heteroclinic tangles

A fixed point of a given system can be either stable or unstable. If the point is stable, all the solutions that start near the fixed point after some time converge back to the fixed point. If the point is unstable, we have to consider two different cases. Either the point is elliptic (small perturbation from the fixed point follows an elliptical path around the fixed point), or hyperbolic. A sketch of the behavior of the points in the vicinity of a hyperbolic fixed point is shown in Fig. (1.2), where the arrows mark the direction of the mapping.

Locally there exists a sequence of points that in the asymptotic fashion maps forward onto the unstable fixed point. These points, marked by a red line in Fig. (1.2), form a structure in SOS called the stable manifold. Similarly, the sequence of points that in the asymptotic fashion maps backward onto the unstable fixed point, marked by a blue line in Fig. (1.2), form a structure in SOS called the unstable manifold. Away from the fixed point, stable and unstable manifolds are not necessarily straight lines anymore. Rather, they twist and bend and eventually intersect each other. The point of the intersection
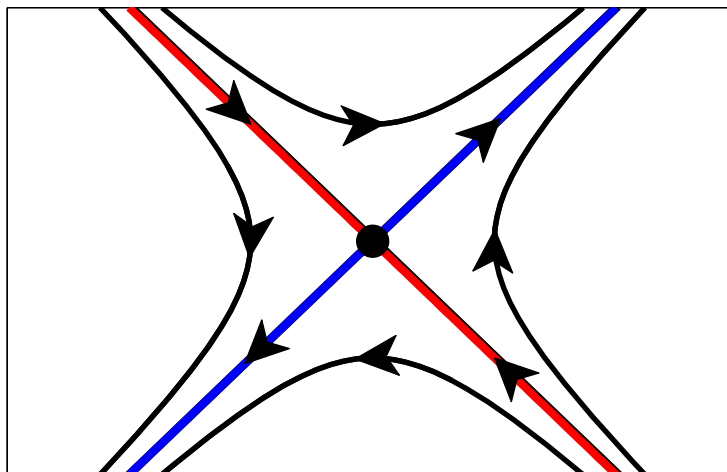
Figure 1.2: A sketch of a hyperbolic fixed point. A big black dot is the unstable fixed point. Red line is the stable manifold and the blue line is the unstable manifold.

is called a homoclinic point if the manifolds originate from the same fixed point, or a heteroclinic point if the manifolds belong to two distinct fixed points. A structure formed by stable and unstable manifolds together with the fixed point is called a homoclinic tangle (or a heteroclinic tangle if the manifolds connect two or more fixed points).

It is important to note that as soon as the stable and unstable manifolds intersect once, they intersect infinitely many times. This can be understood by remembering that a stable/unstable manifold is formed by mapping the points from the vicinity of the fixed point infinitely many times in backward/forward fashion. Hence, once we have found one intersection point, we can find the rest of them by forward and backward mapping. Finally, the stable (and for that matter unstable) manifold cannot have any intersections with itself because that would violate the uniqueness of the solutions to the differential equation describing the system.

## 1.4  Chaos in atomic systems

Atomic systems provide excellent testbeds for studying both classical and quantum chaos because they are readily accessible in laboratories and they can provide valuable insights about chaotic behavior in general. In the past scientists studied processes in chaotic atomic systems with both time dependent and time independent Hamiltonians. These processes included both photoabsorbtion and ionization in atomic gasses. Previous work focused on observing the existence of closed orbits and stable islands in the chaotic sea. Closed orbits have been successfully used to study absorption spectra for atoms in static external fields, while stable islands have been shown to act as barriers to ionization. Stable islands have subsequently also been used to trap, focus and move wave packets in phase space in a controlled manner.

In the 1970s Bayfield and Koch did extensive work on hydrogen atoms in strong microwave fields [2, 3, 26], while Kleppner observed chaos in Rydberg systems [11]. Delos did extensive work on periodic orbit theory and hydrogen in crossed and nearly crossed fields [15, 19, 44]. Later on, Delos and Mitchell performed a thorough study of Rydberg atoms in parallel electric and magnetic fields using homoclinic tangles to explain the ionization process [33, 34, 35, 36, 38]. More recently, Dunning has been able to use the existence of stable islands to focus wave packets in Rydberg atoms [16, 31, 39, 45, 46, 52, 53, 54, 55].

This thesis builds on the previous work in both general chaos theory and the knowledge about chaos in atomic systems, and offers a first observation of a homoclinic tangle in an atomic system experiment. Chapter 2 describes the kicked Rydberg system and presents its SOS, fixed points, and the homoclinic tangle that governs the ionization

process. In Chapter 2 we also present how different system parameters influence the geometry of the homoclinic tangle. Analytical computations, notably a detailed perturbative analysis of the tangle structure using the Melnikov technique [21, 30, 51], are included in Chapter 3. The results from Chapters 2 and 3 are used as a guide to propose two new experiments that directly explore the influence of the homoclinic tangle on the ionization process. These experiments, along with their results, are described in detail in Chapters 4 and 5. Final chapter introduces a novel prescription for defining SOS in hydrogen in crossed fields system which is widely considered as a stepping stone towards understanding the three body problem.

# Chapter 2

# Kicked Rydberg Atoms

The dynamics of Rydberg atoms subjected to periodic external electric field pulses, or kicks, has been the subject of extensive theoretical and experimental interest [1, 2, 3, 4, 16, 24, 26, 31, 39, 45, 46, 52, 53, 54, 55]. This interest stems both from the use of such pulse trains as a means of controlling the electronic state of atoms and because such systems are excellent models for the study of classical and quantum chaos. In particular, techniques for the controlled manipulation of Rydberg wavepackets for very highly excited states ($n > 300$) have been well developed, including the trapping, focusing, and steering of packets into desired regions of phase space [31, 52, 53, 55]. The work presented here has been particularly motivated by the experimental studies of Dunning and coworkers on quasi-one-dimensional Rydberg atoms exposed to periodic external electric field pulses [1, 16, 31, 39, 45, 46, 52, 53, 54, 55]. They have developed experimental techniques for creating highly excited quasi-one-dimensional potassium atoms and then subjecting such atoms to a variety of periodic pulse sequences. They have studied the dependence of

the survival probability (the fraction of unionized atoms after each kick) as a function of the direction, frequency, and strength of the applied kicks. They have also observed the existence of stable islands in the chaotic phase space and used these islands as a tool for wavepacket control. Specifically, they have successfully loaded electron wavepackets inside stable islands, adiabatically moved the islands within phase space, and changed the size of the islands in order to better focus the wavepacket. Importantly, they have demonstrated, using classical trajectory Monte Carlo simulations, that many of the essential features of their experiments on quasi-one-dimensional Rydberg atoms can be modeled using purely one-dimensional simulations along a radial half-line.

In this chapter, we present the work on the ionization of quasi-one-dimensional Rydberg atoms subjected to a periodic sequence of externally applied electric-field pulses that alternate between imparting a kick toward and away from the nucleus. As in Refs. [46, 54], the dynamics can be described by a one-dimensional classical model. As a periodically driven one-dimensional system, this model exhibits classical chaos, which increases with the strength of the applied kicks. This can be observed in the Poincaré surface of section plots. The analysis of the chaotic ionization of this system is based on the novel observation that the escape process is governed by a geometric structure in phase space, called a turnstile [29], and its associated homoclinic tangle. The homoclinic tangle forms a kind of "leaky separatrix", which separates the unionized from the ionized states, and the turnstile is a kind of portal that allows states to pass through the leaky separatrix. Such geometric techniques have previously been used to study chaotic ionization for atoms in parallel electric and magnetic fields [33, 34, 35, 36, 37, 38]. More generally, turnstiles and tangles

are phase space structures that are broadly applicable to chaotic transport and escape processes in a wide array of physical systems [5, 6, 7, 8, 9, 10, 13, 14, 17, 21, 22, 25, 28, 29, 32, 33, 34, 35, 36, 38, 40, 41, 42, 43, 47, 48, 49, 51].

After demonstrating that the ionization process in this system is governed by a phase space turnstile, we present the work on the geometry of the lobes of the turnstile. In particular, we demonstrate how the size, shape, and position of these lobes depends on the experimentally accessible kicking parameters, notably the kick duration, kick strength, and kicking period. (For example, increasing the kick strength stretches the length of a lobe without affecting its width.) In this chapter, we demonstrate this dependence through direct numerical computations of the lobe geometry. Analytical computations that confirm the numeric results presented in this chapter, are included in Chapter 3. The results on the lobe structure from this chapter are used as a guide to propose two new experiments that directly explore the influence of the lobe dynamics on the ionization process. These experiments, along with their results, are described in detail in Chapters 4 and 5.

This chapter is organized as follows. Section 2.1 describes the kicked hydrogen system. In section 2.2 we describe the canonical coordinate transformation used to avoid numerical problems arising from large numbers close to the nucleus which are caused by a singularity at the nucleus in the Coulomb potential. Section 2.3 shows the structure of the chaotic phase space, and section 2.4 provides a prescription for finding the fixed points in this system. Section 2.5 develops the key geometric picture demonstrating how the chaotic ionization process proceeds via a phase space turnstile, and how the turnstile transports the electronic state across a homoclinic tangle. Section 2.6 presents the numerical compu-

tations of the tangle geometry, which show the influence of the experimental parameters (the kick strength $\Delta p$, the kick duration $\tau_k$, and the kicking period $T$) on the size and shape of the lobes.

## 2.1   The system

In this section we describe a classical one-dimensional kicked Rydberg system. Current experimental techniques are capable of creating highly elongated Rydberg states in which the bulk of the electron motion is along a single radial line [1, 16, 31, 39, 45, 46, 52, 53, 54, 55]. In this case, the electron dynamics can be modeled as occurring along a single one-dimensional radial half line. We need a half line, rather than a full line, for the following reason. In two spatial dimensions, classical hydrogen electron orbits are ellipses, with the nucleus at one of the foci. Taking the limit from two to one spatial dimension can be understood as pulling apart the two foci of the ellipse while keeping the energy of the orbit constant. The classical Kepler period of the orbit depends on its energy, so it too is kept constant. Kepler's third law states that the period of an elliptic orbit is proportional to the length of the major axis of the ellipse raised to the 3/2 power. Hence in the process of taking the 2D to 1D limit, we are also keeping the length of the major axis constant. The sketch of this process can be seen in Figure (2.1). Thus, in the one-dimensional limit, the electron orbit collapses onto a half line with the nucleus located at $r = 0$, where $r \geq 0$ represents the electron's distance from the nucleus. The length of the half line is equal to the length of the major axis of the 2D elliptical orbit.
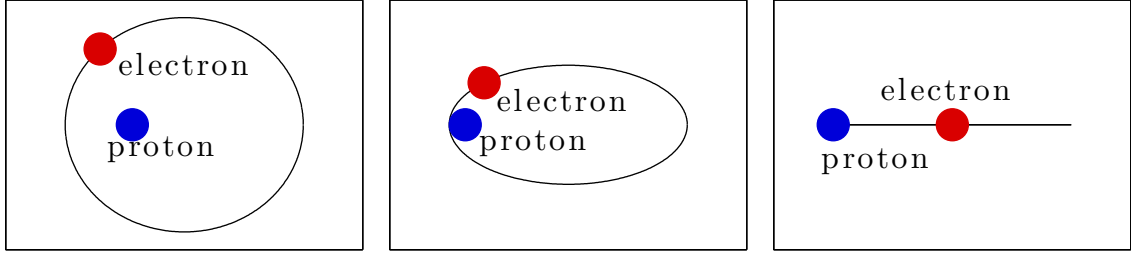
Figure 2.1: A cartoon representation of the 2D to 1D limit. The major axis is kept constant while the minor axis is shrinking. The proton (a big blue dot) is located at one of the foci of the ellipse, and the electron (a big red dot) is orbiting the proton.

The electron's motion is described by the classical one-dimensional Hamiltonian

$$H(r, p_r) = \frac{p_r^2}{2} - \frac{1}{r}, \tag{2.1}$$

where $p_r$ is the electron's momentum a distance $r$ away from the nucleus, and the atomic units ($e = m_e = \hbar = 1$) are used throughout. Figure (2.2) shows the phase space of this unkicked system. Because the system is Hamiltonian and independent of time, the energy $E$ is constant along an electron orbit. For $E < 0$ the orbits are bound, and for $E > 0$ the orbits are unbound. The momentum of each orbit is infinite at the Coulomb singularity ($r = 0$) [1]. An electron with negative momentum $p_r$ speeds up as it approaches the nucleus from the right. It obtains an infinite negative momentum at $r = 0$, but does not pass onto the other side of the singularity, $r < 0$. Rather, it reflects off the singularity, flipping the sign of the momentum to positive infinity. If $E < 0$, the electron then moves away from the nucleus and slows down until it reaches a turning point, and then periodically repeats this motion. As energy increases, the turning point of the bound orbit moves farther away from the nucleus, and the Kepler period increases. At $E = 0$, the turning point $(r, p_r) = (\infty, 0)$

---

[1] We avoid numerical difficulties associated with the infinite momentum at the Coulomb singularity by numerically integrating the kicked system in parabolic coordinates (see section 2.2)
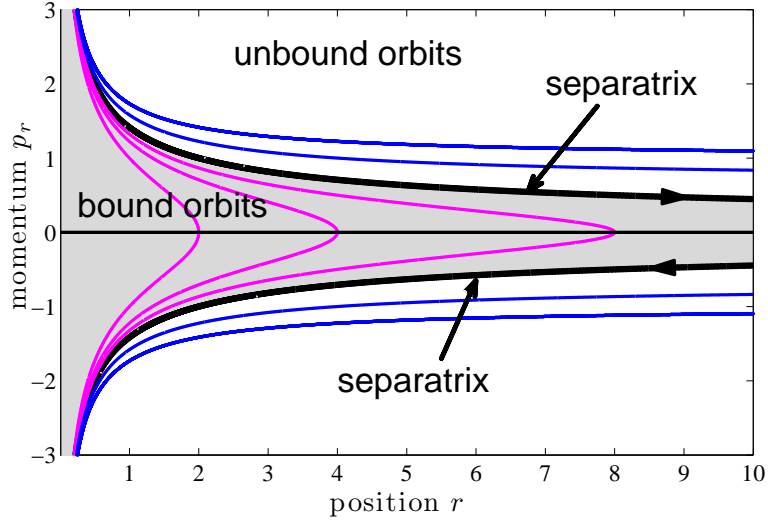
Figure 2.2: Phase space of the unkicked system. The shaded region is the negative energy region where all the orbits are bounded. The separatrix (thick black line) separates the bound orbits (thin magenta lines) from the unbound orbits (thin blue lines).

is at infinity, and the Kepler period is infinite as well. This zero-energy orbit forms a separatrix that acts as a barrier to transport between the bound and unbound orbits in phase space. For $E > 0$, upon bouncing off the nucleus, the electron escapes to infinity with a nonzero asymptotic momentum.

In the current experimental setups [1, 16, 31, 39, 45, 46, 52, 53, 54, 55], the kicks to the electron are applied using an external electric field. Hence in the kicked system, the electron's motion is governed by the following 1D Hamiltonian:

$$H(r, p_r, t) = \frac{p_r^2}{2} - \frac{1}{r} - rF(t), \tag{2.2}$$

where $F(t)$ describes the external force resulting from the applied electric field and is responsible for applying kicks to the electron. The external driving force is periodic, with alternating positive and negative square kicks, as shown in Fig. 2.3. Positive $F(t)$ corresponds to kicking the electron away from the nucleus, and negative $F(t)$ corresponds
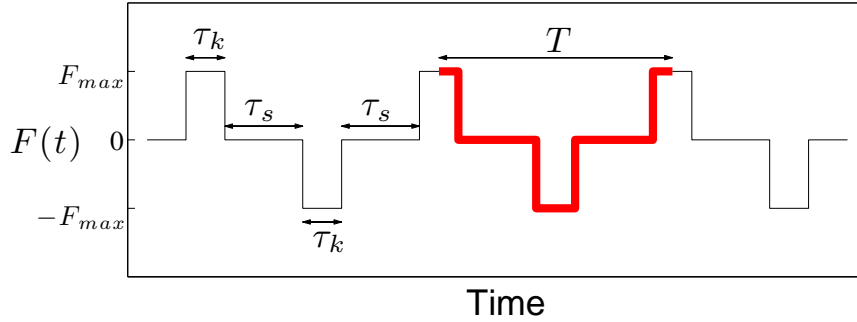
Figure 2.3: The externally applied electric force. The duration of each kick is $\tau_k$ and the separation between consecutive kicks is $\tau_s$. Hence the total kicking period is $T = 2\tau_k + 2\tau_s$. The bold line denotes one cycle of the Poincaré map (i.e. one kicking period).

to kicking the electron towards the nucleus. In Fig. 2.3, $F_{\max}$ is the maximum amplitude of

the force, $\tau_k$ is the kick duration, $\tau_s$ is the separation time between consecutive kicks, and

$T = 2\tau_k + 2\tau_s$ is the total kicking period. Finally, $\Delta p = \tau_k F_{\max}$ is the integrated strength

of each of the kicks. There are only three independent parameters in this system, so in

the remainder of this thesis we focus our attention on how $\tau_k$, $T$, and $\Delta p$ influence the

ionization process. For the reasons that will become apparent later, we choose our kicking

period to be symmetric under time reversal. Even though the total impulse imparted

during one kicking period is zero, the system is still chaotic. Throughout this thesis we will

frequently consider delta-function shaped kicks obtained by taking the limit $\tau_k \to 0$ while

keeping the total impulse $\Delta p$ constant. These delta-function kicks are not reproducible in

the experiment, but they nonetheless provide a useful toy model for understanding various

behaviors observed in this system.

## 2.2 Coordinate Transformations

In this section we define a coordinate transformation that defines the coordinates used in our numerical simulations. In order to avoid any numerical problems associated with the Coulomb singularity at the nucleus we perform a standard canonical coordinate transformation from physical $(r, p_r)$ to parabolic $(u, p_u)$ coordinates. These parabolic coordinates are used mainly to perform numeric simulations presented in this thesis. The transformation is defined by the following relations:

$$u = \sqrt{2r}, \quad p_u = up_r. \tag{2.3}$$

The unkicked Hamiltonian in parabolic coordinates is defined as

$$h(u, p_u) = 2r(H - E) = \frac{1}{2}p_u^2 - Eu^2 - 2, \tag{2.4}$$

where $E$ is the electron energy, and hence $h(u, p_u)$ must equal zero. Time $s$ in parabolic coordinates is determined by the differential equation

$$\frac{ds}{dt} = \frac{1}{2r}. \tag{2.5}$$

Position $u$ and momentum $p_u$ are then functions of $s$.

In the absence of kicks, electron's motion is restricted to a particular energy shell and its time evolution can be calculated exactly in parabolic coordinates. Since the duration of the time evolution for a particular electron is given in physical time $t$, in order to evolve electron forward in time, we first have to find an expression for the time $s$ in parabolic coordinates as a function of physical time $t$. To accomplish this, we start with

Hamilton's equations

$$\frac{dp_u}{ds} = -\frac{\partial h}{\partial u} \qquad \text{and} \qquad \frac{du}{ds} = \frac{\partial h}{\partial p},$$

which result in

$$\dot{p}_u = 2Eu \qquad \text{and} \qquad \dot{u} = p_u,$$

where overdot refers to differentiation with respect to $s$. Combining these two equations we get

$$\ddot{u} = 2Eu. \tag{2.6}$$

The solution to this differential equation provides us with functional expressions for position and momentum

$$u(s) = \text{Re}\left(Ae^{i\left(\sqrt{2|E|}s+\phi\right)}\right)$$

$$p_u(s) = \text{Re}\left(Ai\sqrt{2|E|}e^{i\left(\sqrt{2|E|}s+\phi\right)}\right), \tag{2.7}$$

where $A$ and $\phi$ are constants determined by plugging the solution to $u(s)$ into equation (2.4). For bound orbits (i.e, $E < 0$) the constant $A$ of the integration is

$$A = \pm\sqrt{\frac{2}{|E|}},$$

where the sign of $A$ is equal to the sign of $u$. In contrast to physical coordinates, where $r$ is always greater than zero, parabolic coordinates allow a $u < 0$ solution. In fact, the change in sign of $u$ signals that the electron has hit the nucleus. Since the electron's distance from the nucleus is always a positive number, we identify the point $(u < 0, p_u)$ with $(-u, -p_u)$. A second integration constant $\phi$ is given by

$$\phi_- = \arctan\left[-\frac{p_0}{u_0}\sqrt{-2E}\right],$$

where $p_0$ and $u_0$ are the values of position and momentum in parabolic coordinates at $t = s = 0$. Hence,

$$u(s) = \pm \sqrt{\frac{2}{-E}} \cos\left(\sqrt{-2E}s + \phi_-\right). \tag{2.8}$$

Similarly, when the electron is unbound (i.e, $E > 0$),

$$\phi_+ = \operatorname{arctanh}\left[\frac{p_0}{u_0}\sqrt{2E}\right],$$

and

$$u(s) = \sqrt{\frac{2}{E}} \cosh\left(\sqrt{2E}s + \phi_+\right). \tag{2.9}$$

Since

$$\frac{ds}{dt} = \frac{1}{u^2},$$

for a given value of $t$, $s$ can be calculated by performing the following integrals

$$\int_0^s \left[\cos\left(2\left(\sqrt{-2E}s' + \phi_-\right)\right) + 1\right] ds' = \int_0^t -E\,dt',$$

or

$$\int_0^s \left[\cosh\left(2\left(\sqrt{2E}s' + \phi_+\right)\right) + 1\right] ds' = \int_0^t E\,dt',$$

for $E < 0$ and $E > 0$, respectively. Finally, the time $s$ in the parabolic coordinates can be found by numerically solving the implicit equations:

$$\frac{1}{2\sqrt{-2E}}\left[\sin\left(2\left(\sqrt{-2E}s + \phi_-\right)\right) - \sin\left(2\phi_-\right)\right] + s = -Et, \quad E < 0 \tag{2.10}$$

and

$$\frac{1}{2\sqrt{2E}}\left[\sinh\left(2\left(\sqrt{2E}s + \phi_+\right)\right) - \sinh\left(2\phi_+\right)\right] + s = Et, \quad E > 0 \tag{2.11}$$
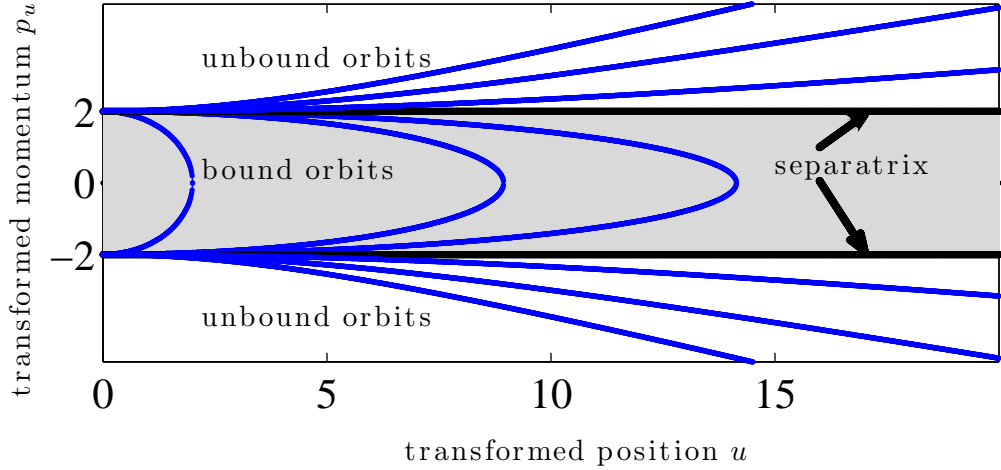
Figure 2.4: Figure shows the phase space of the unkicked system described in Sec. 2.1 in parabolic coordinates.

In the $E = 0$ case, the equations become very simple

$$u = \pm 2s, \qquad p_u = \pm 2 \qquad \text{and} \qquad s = 3/4t^{1/3}.$$

Figure (2.4) shows the phase space in the transformed coordinates for the unkicked case. This canonical transformation "brings in" the value of the momentum at the nucleus from $p_r = \pm\infty$ to $p_u = \pm 2$. The separatrix now consists of two parallel lines with transformed momenta $p_u = \pm 2$.

In the presence of kicks, the Hamiltonian in the parabolic coordinates becomes

$$h(u, p_u) = \frac{1}{2}p_u^2 - Eu^2 - \frac{1}{2}Fu^4 - 2. \tag{2.12}$$

The Hamilton's equation that needs to be solved when $F \neq 0$ is then

$$\ddot{u} = Eu - 2Fu^3.$$

This equation has four different solutions in the form of Jacobi elliptic functions depending on the signs of $E$ and $F$. As we have seen in the $F = 0$ case, the value of time $s$ depends on

the position and momentum at a given time. In order to solve for $s$ we had to find a zero of an implicit function. When the kicks are turned on, and the solutions to $u(s)$ and $p_u(s)$ are Jacobi elliptic functions, the implicit equation for $s$ includes various combinations of Jacobi elliptic functions. In our system, these functions were very steep, and we have not been able to automate root searching routines in MATLAB that would provide us with a value of $s$. Hence, the simulation results in the presence of the kicks presented in this thesis are produced using built in MATLAB ode solvers, and the reader is directed to Appendix A for the Jacobi elliptic solutions to $\ddot{u} = Eu - 2Fu^3$. Thus, our numerical results are a product of a combination of approaches: when the electron is not being kicked we use analytic expressions to propagate it forward in time, and during the duration of the kicks, we use readily available ode solvers.

Finally, we use parabolic coordinates introduced in this section to perform numeric simulations presented in this thesis. However, since it is easier to develop intuition about the effects we explore in this work in physical coordinates, we choose display all the results in physical coordinates.

## 2.3  Surface of Section

In this section we define the Poincaré return map used to obtain the results in this and Chapters 3, 4, and 5. We next use this Poincaré return map to obtain Poincaré surface of section and observe the existence of stable islands in this system.

Instead of continuously tracking electron's classical orbits, we define a discrete-time Poincaré map $(r, p_r) \mapsto (r', p_r')$ by recording $(r, p_r)$ once per kicking period $T$. The

benefit of this approach is that we can utilize geometric structures that arise in phase space to study time evolution of the electrons without keeping track of their complete orbits. Our definition of the Poincaré return map is equivalent to taking stroboscopic "snapshots" of the system, with the strobing period equal to $T$. The snapshots are taken and $(r, p_r)$ is recorded half way through the positive kick (see Fig. 2.3) so that the map is symmetric under time reversal. That is, beginning with the state $(r, p_r)$ we (i) apply half of the kick away from the nucleus, (ii) let the electron evolve freely for time $\tau_s$, (iii) apply the full kick towards the nucleus, (iv) let the electron evolve freely again for time $\tau_s$, (v) apply another half-kick away from the nucleus, and (vi) record the final position and momentum $(r', p_r')$. This particular choice of timing is chosen because it makes for an easy definition of an inverse of the map. Furthermore, as we will show later, it causes the stable and unstable manifolds to be reflections of each other about $p_r = 0$ line.

The electron motion when exposed to external alternating positive and negative kicks is chaotic. This can be confirmed by the surface of section plots which show that the phase space is occupied by the stable islands surrounded by the chaotic sea. Figure (2.5) shows the surface of section plot for delta-function shaped kicks ($\tau_k = 0$) with $\Delta p = 0.1$ and $T = 10$. Stable islands can be detected by either the absence of point density or by its significant increase. Since stable islands form a barrier to transport in phase space, initial conditions that start outside the islands are never allowed to enter the islands, and in the SOS plot we observe the signature of these islands as a void in point distribution. Similarly, the initial conditions that start inside the islands are never allowed to cross the island barrier, and are confined to chaotic trajectories inside these islands. Hence,
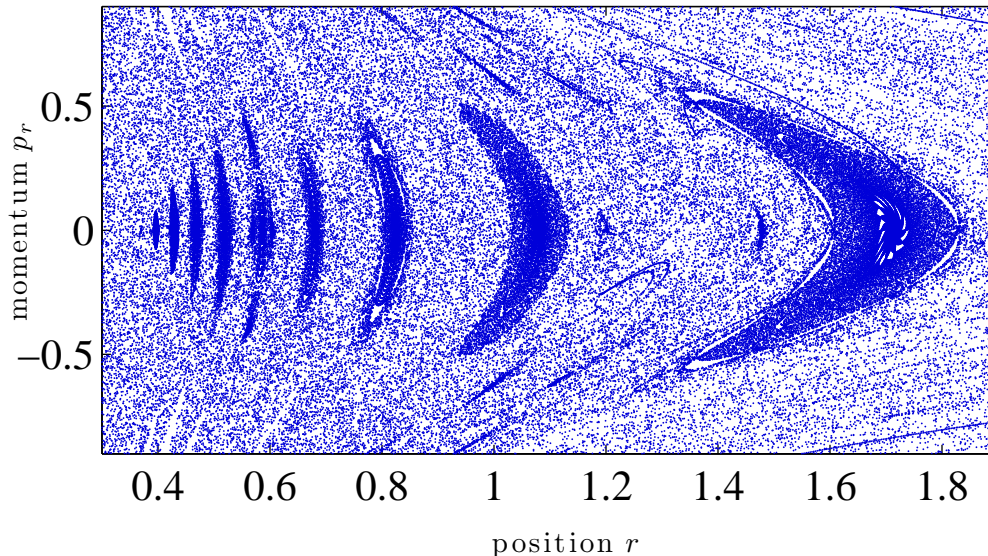
Figure 2.5: Surface of section plot for $\Delta p = 0.1$ and $T = 10$. Notice the existence of the chain of stable islands in the chaotic sea.

these islands appear in the SOS plot as an increase in the density of point distribution. Figure (2.6) shows a close up of some of the islands shown in Fig. (2.5). One can observe a variety of shapes and sizes of stable islands in this system.

As the kick strength increases, so does the amount of chaos in the system. Figure (2.7) shows the islands in the chaotic sea for the same value of $T$, but with $\Delta p$ twice the value as in Fig. (2.5). Most of the islands have dissolved and the size of the remaining ones has shrunk. The phase space is now mostly occupied by the chaotic sea. Further increase in the kick strength dissolves the remaining stable islands and the phase space is fully populated by the chaotic sea.

The stable islands are very small or nonexistent for the values of the system parameters used in the experimental setup. Since the focus of this thesis is on the physical mechanism involved in chaotic ionization, we now move on to examining the fixed points
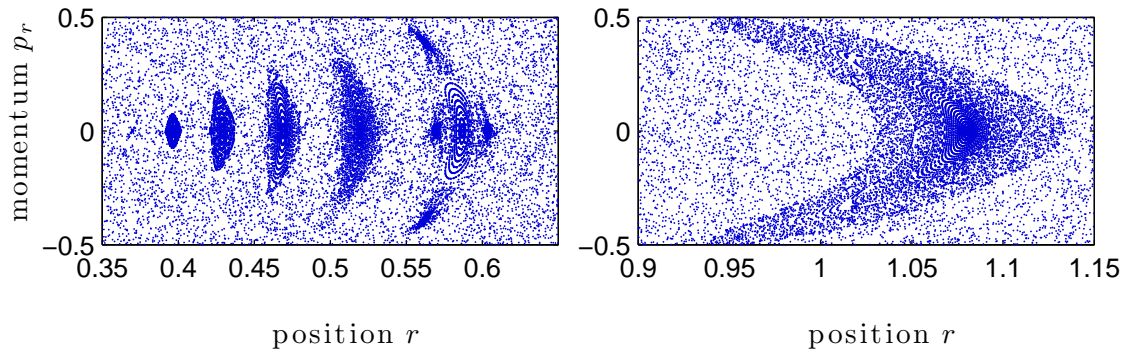
Figure 2.6: Surface of section plot for the zoomed in part of Fig. (2.5) focused onto different stable islands.
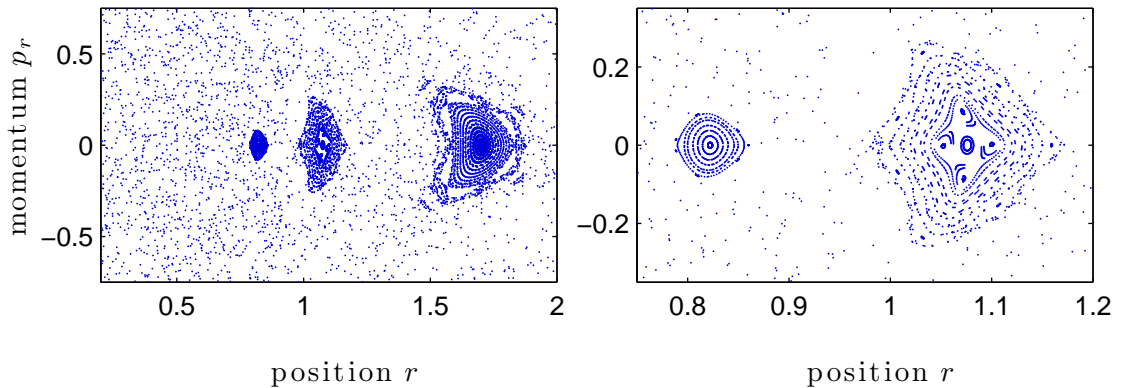


Figure 2.7: Surface of section plot for $\Delta p = 0.2$ and $T = 10$. The figure on the right zooms in on the two stable islands closer to the nucleus.

in this system and their stable and unstable manifolds.

## 2.4  Fixed Points

In this section we use the Poincaré return map defined in the previous section to obtain the fixed points in this system. The main focus of this thesis is on the study of the chaotic ionization of Rydberg atoms exposed to alternating positive and negative kicks. This phenomenon is governed by the homoclinic tangle attached to the fixed point
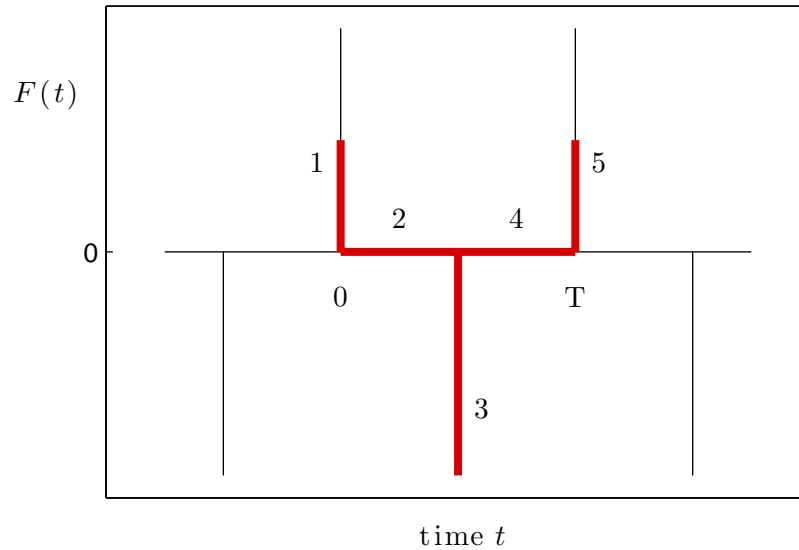
Figure 2.8: A sketch of delta-function shaped kicks. The red line marks one period of the Poincaré return map.

at $(r, p_r) = (\infty, 0)$. However, this system contains infinitely many fixed points. In order to gain physical intuition about the fixed points, we use delta-function-shaped kicks. As we have already mentioned, these kicks are instantaneous, meaning that imparting a delta function kick changes electron's momentum, while keeping its position the same, i.e. $(r, p_r) \mapsto (r, p_r \pm \Delta p)$. One iteration of the Poincaré return map for delta-function kicks is shown in Fig. (2.8) as a thick red line.

Fixed points in this system can be divided into two categories: those whose momentum coordinate is equal to zero, and those with a nonzero momentum coordinate. The latter fixed points always come in pairs. They are equally far away from the nucleus, but their momenta have opposite signs.

We first examine fixed points with the momentum coordinate equal to zero. For the unkicked case, the "turning point" of the separatrix is $(r, p_r) = (\infty, 0)$. This is an
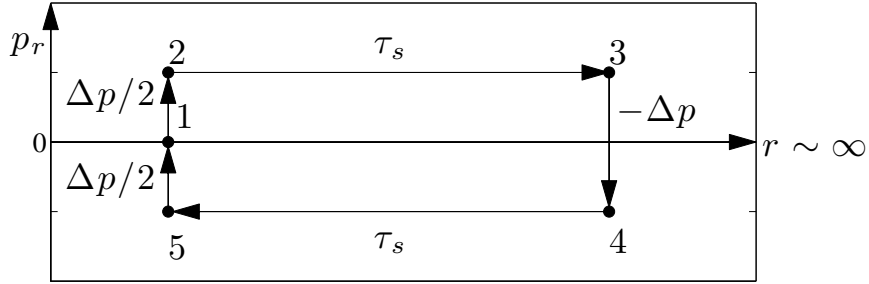
Figure 2.9: Fixed Point at Infinity.  The above is a sketch of the motion of a point $(r \approx \infty, p_r = 0)$ under one iteration of the map specified by the sketch in Fig. (2.8). Each transition between points is understood as follows. 1 to 2: half of the positive kick; 2 to 3: free time evolution; 3 to 4: full negative kick; 4 to 5: free time evolution; 5 to 1: remaining half of the positive kick.

equilibrium point, or a fixed point, of the system, because the Coulomb force vanishes at $r = \infty$. When the kicks are turned on $[F(t) \neq 0]$, the point $(r, p_r) = (\infty, 0)$ remains a fixed point in the kicked system. This can be understood using delta-function kicks and Fig. (2.9). Consider an electron at $r \sim \infty$ and $p = 0$ (position 1 in Fig. (2.9)).  After the initial positive half-kick of the map, the electron moves to position 2. It then moves away from the nucleus as a free particle for time $\tau_s$ to position 3. Next, after the full negative kick the electron moves to position 4. At this point the electron moves again as a free particle, but this time back towards the nucleus, and after time $\tau_s$ it is at position 5. Finally, after the last positive half-kick, it is back at the starting position 1. Hence $(r, p_r) = (\infty, 0)$ maps to itself, and it is thus a fixed point of the system. This argument holds even when $\tau_k \neq 0$, so the fixed point at infinity remains a fixed point in this system.

To examine the position of the rest of the fixed points with zero momentum coordinate, we use Figs. (2.8) and (2.10). The outermost fixed point with zero momentum is the one for which the electron lands after the initial positive half-kick onto an energy

shell whose classical Kepler period is equal to the separation between the positive and negative kicks $\tau_s$. To illustrate this, start with a fixed point on axis (i.e, with an electron at the turning point of its energy shell) shown as a red dot in Fig. (2.10). Next, we apply half of a positive kick (labeled as 1 in Figs. (2.8) and (2.10)). This increases the electron's momentum by $\Delta p/2$, while keeping its position the same. As a result the electron jumps onto an energy shell with a longer Kepler period. After the first positive kick, we let the electron evolve in the Coulomb potential. This is marked as 2 in Figs. (2.8) and (2.10). If the Kepler period of the new energy shell is equal to $\tau_s$, the electron returns back to the same value of $(r, p_r)$ as it was after we applied the first positive kick. Next, we give the electron a full negative kick (marked as 3 in Figs. (2.8) and (2.10)). This negative kick reverses the sign of the electron's momentum while keeping its position and energy unchanged. The electron then again evolves for $\tau_s$ (marked as 4 in Figs. (2.8) and (2.10)). Finally we apply the second half of the positive kick (marked as 5 in Figs. (2.8) and (2.10)), which returns the electron back to the position of the big red dot. Hence the big red dot marks the location of a fixed point in this system. The rest of the fixed points can be found by requiring that $\tau_s = nT_K$, where $n \geq 2$ and $T_K$ is the Kepler period of the energy shell. Using this approach, we can write down the location of fixed points whose momentum coordinate is equal to zero as

$$(r, p_r) = \left( \left( \frac{1}{2} \left( \frac{2\pi n}{\tau_s} \right)^{2/3} + \frac{\Delta p}{8} \right)^{-1}, 0 \right), \tag{2.13}$$

where $n$ is an integer, and $n = 1$ corresponds to the outermost fixed point that is not at infinity.

The same type of analysis is used to locate fixed points with a nonzero momentum
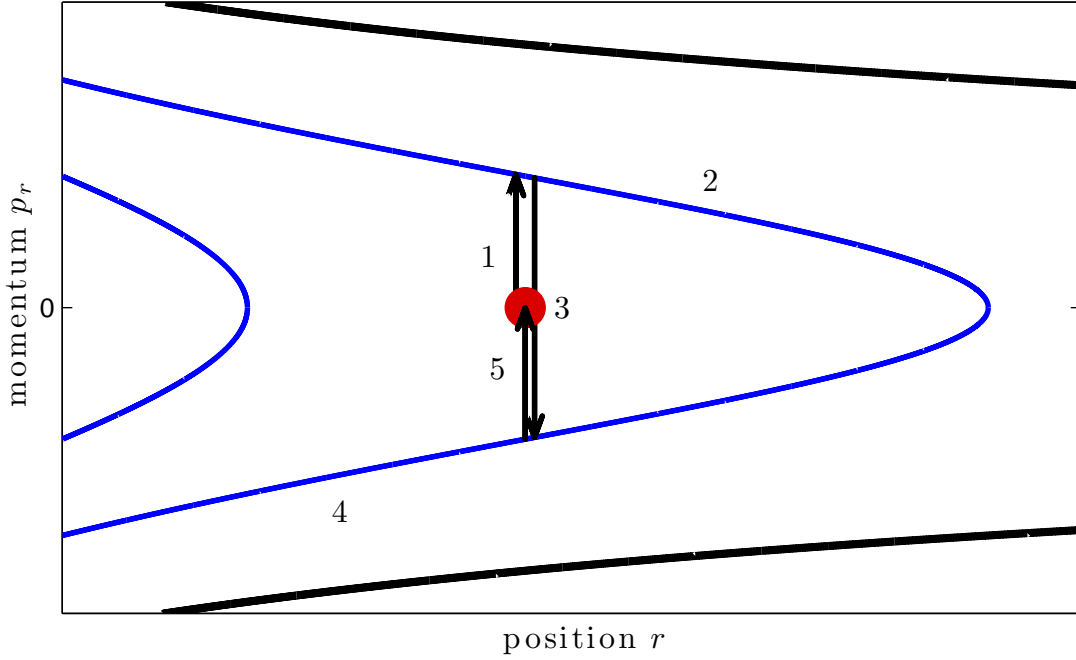
Figure 2.10: The blue lines represent the bound orbits, the black line is a separatrix, and the red dot is a fixed point. The arrows sketch the influence of the positive and negative kicks shown in Fig. (2.8). The numbers correspond to different events marked in Fig. (2.8).

coordinate. A sketch of these fixed points is shown in Fig. (2.11). After the initial positive half kick the electron starting at the fixed point with positive momentum coordinate jumps onto an energy shell that has longer Kepler period than the energy shell which contains the fixed point. In order to find the outermost fixed point with positive momentum coordinate, we need to require that the Kepler period of this energy shell $(T_+)$ is equal to $\tau_s$. After one Kepler period, the electron is exposed to the negative kick which causes it to jump to the lower energy shell with a shorter Kepler period $(T_-)$. Hence, we now require that $\tau_s = 2T_-$, which is the next longest Kepler period. Similarly, the electron starting at the fixed point with negative momentum coordinate jumps onto an energy shell that has shorter Kepler period than the energy shell that contains the fixed point, so the longer
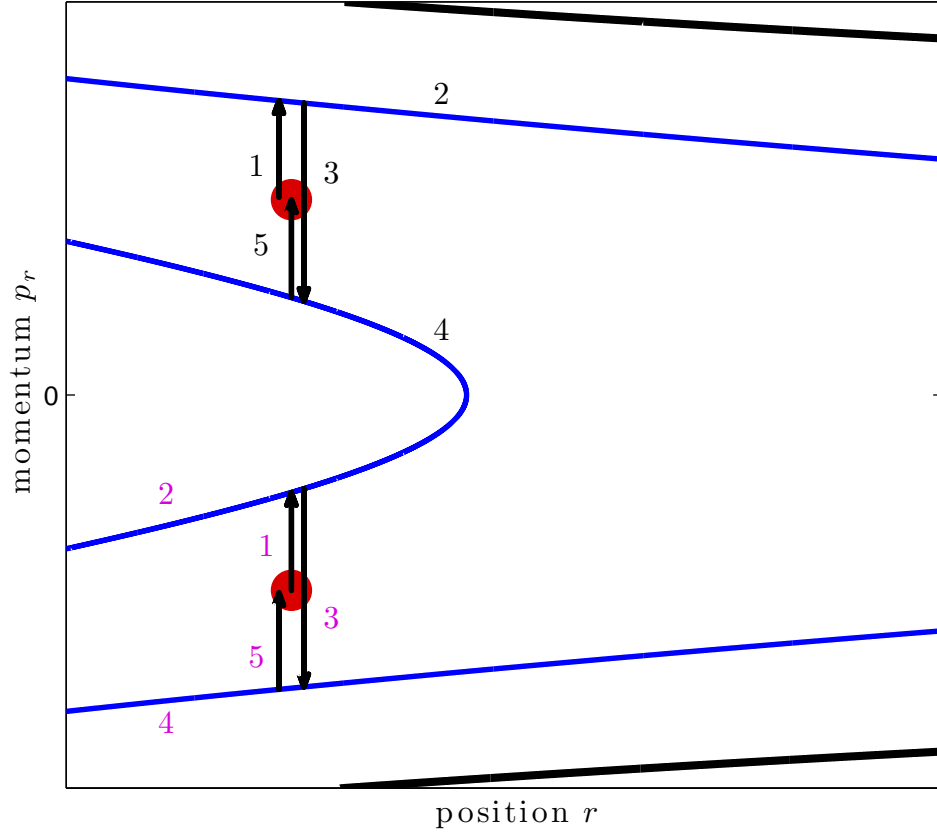
Figure 2.11: The blue lines represent the bound orbits, the black line is a separatrix, and the red dots are fixed points. The arrows sketch the influence of the positive and negative kicks shown in Fig. (2.8). The numbers correspond to different events marked in Fig. (2.8). Black numbers correspond to the fixed point with positive momentum coordinate, and the purple numbers correspond to the fixed point with negative momentum coordinate.

and shorter period shells are swapped. This leads to the following coordinates for the fixed points with nonzero momentum

$$(r, p_r) = \left( \frac{8\Delta p^2 \tau_s^{4/3}}{\left[ (2\pi)^{2/3}(m^{2/3} + n^{2/3}) + \Delta p^2 \tau_s^{2/3} \right]^2 - 4(2\pi m n)^{2/3}}, \pm \left( \frac{2\pi}{\tau_s} \right)^{2/3} \frac{m^{2/3} - n^{2/3}}{2\Delta p} \right),$$

$$(2.14)$$

where $m$ is an integer strictly greater than $n$. The outermost fixed point with nonzero momentum occurs for the ratio $m : n = 2 : 1$.

For the range of the parameters used in the experiment, the position of the fixed points associated with delta-function forcing is rather close to the actual fixed points of the square-shaped forcing enabling us to use the position of the delta-function fixed point as a seed in the fixed point finding routine for the square-shaped forcing. The caveat is that the stability of the fixed point might change as the forcing changes from delta-function to square-shaped.

All the unstable fixed points have their own homoclinic tangle associated with them. The fixed point that is furthest away from the nucleus (in this case that is the fixed point at infinity with zero momentum) along with its stable and unstable manifolds dictates the ionization process, because the homoclinic tangles attached to inner unstable fixed points are contained inside the outermost tangle. The existence of the inner tangles does influence the ionization process [37], but for the parameters used in the experiment this influence is not significant and this study is left for the future.

## 2.5   Homoclinic Tangle

In this section we present the stable and unstable manifolds which together form a homoclinic tangle and a turnstile that governs the ionization process in the kicked Rydberg system. It was shown in the previous section that the fixed point of the unkicked system at $(r, p_r) = (\infty, 0)$ is the turning point of the separatrix. The forward time evolution of every point on the separatrix converges upon the fixed point $(\infty, 0)$. Thus, the separatrix (including both the upper and lower branches) can be interpreted as the stable manifold of the fixed point $(\infty, 0)$. Remember that in general, a stable/unstable manifold consists of

all points whose forward/backward time evolution converges upon a fixed point, or other invariant set. The backward iterates of every point on the separatrix also converge upon $(\infty, 0)$, so the separatrix is also the unstable manifold of $(\infty, 0)$. Thus, for the unkicked case the stable and unstable manifolds of $(\infty, 0)$ coincide with each other and with the separatrix.

Let us now consider the kicked case $[F(t) \neq 0]$. It was shown in section 2.4 that the point $(r, p_r) = (\infty, 0)$ remains a fixed point. As in the unkicked case, the fixed point at infinity has a stable manifold $W^s$ and an unstable manifold $W^u$ attached to it. However, in the kicked case, the structure of these manifolds is drastically different (see Fig. (2.12)). The lower branch of the unstable manifold follows a curve whose shape closely resembles the separatrix for $p_r < 0$ in the unkicked case. Upon reflection off the nucleus though, the upper branch of the unstable manifold does not follow the smooth shape of the separatrix for $p_r > 0$. Rather, it continues along a complicated winding curve that repeatedly crosses the stable manifold $W^s$. The unstable manifold $W^u$ also exhibits sharp points, which we call "horns". Due to the time-reversal symmetry of our map, the stable and unstable manifolds are reflections of one another about the line $p_r = 0$. Hence, the unstable manifold does not coincide with the stable manifold as it did in the unkicked case. Instead, the stable and unstable manifolds together form a complicated pattern of intersecting manifolds, called a homoclinic tangle, which forms a "leaky separatrix" as described below [5, 6, 7, 8, 9, 10, 13, 14, 17, 21, 22, 25, 28, 29, 32, 33, 34, 35, 36, 38, 40, 41, 42, 43, 47, 48, 49, 51].

We define the resonance zone to be the region of phase space bounded from above
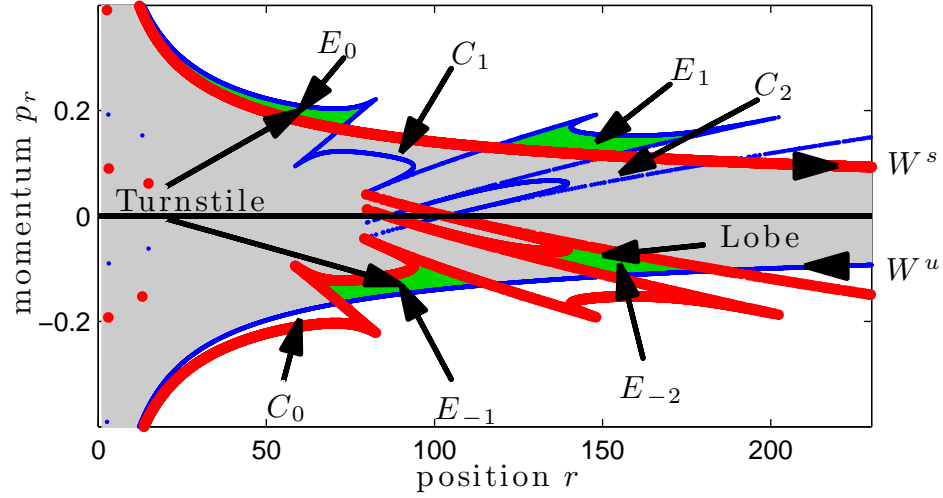
Figure 2.12: A representative homoclinic tangle for the hydrogen atom exposed to alternating positive and negative kicks. The thick red line represents the stable manifold $W^s$, and the thin blue line represents the unstable manifold $W^u$. The escape lobes $E_k$ of the homoclinic tangle are shaded green and the resonance zone is shaded light gray.

by the upper branch of the stable manifold connecting the nucleus to the fixed point at infinity, and from below by the lower branch of the unstable manifold connecting the fixed point to the nucleus (represented by the gray shaded region in Fig. (2.12)). In the unkicked case, the resonance zone consists of the negative energy orbits (the shaded area in Fig. (2.2)), but in the kicked case (the shaded area in Fig. (2.12)) this is no longer true. Note that in both the kicked and unkicked cases, the area of the resonance zone is infinite.

The homoclinic tangle defines regions in phase space called lobes (see Fig. (2.12)), which fall into two categories: those governing the escape from the resonance zone (ionization) and those governing the capture into the resonance zone. The focus of this thesis is on the escape lobes. Escape lobe $E_0$ is the region of phase space bounded by the upper branches of $W^u$ and $W^s$ between the nucleus and the closest $W^s$ and $W^u$ intersection with positive $p_r$. (See Fig. (2.12).) Mapping the lobe $E_0$ forward and backward defines

the escape lobes $E_k$, with $0 < k < \infty$ and $-\infty < k < 0$ respectively. Thus lobe $E_k$ maps to

lobe $E_{k+1}$. In Fig. (2.12), we see that lobe $E_{-2}$, after one kicking period, maps into $E_{-1}$,

which then maps into $E_0$. Mapping from $E_{-1}$ to $E_0$ is the critical step in which an electron

trajectory maps from inside the resonance zone to outside the resonance zone. This step

leads to escape, or ionization, of an electron trajectory. The lobe $E_0$ subsequently maps

to $E_1$, then to $E_2$, $E_3$, and so forth, never to return to the resonance zone. For this reason

we call the $E_k$ lobes, $-\infty < k < \infty$, escape lobes. In summary, the dynamics of the escape

lobes govern the ionization process.

The capture lobe $C_0$ is the region of phase space bounded by the lower branches

of $W^u$ and $W^s$ between the nucleus and the closest $W^s$ and $W^u$ intersection with negative

$p_r$. (See Fig. (2.12).) Mapping the lobe $C_0$ forward and backward defines the sequence

of capture lobes $C_k$ analogous to the escape lobes. For example, the $C_0$ lobe after one

kicking period maps into $C_1$ lobe which corresponds to the electron trajectories mapping

from the outside to the inside of the resonance zone. Note that since we are working with

a Hamiltonian system, the Poincaré map is area-preserving (by Liouville's theorem), and

hence all the lobes have the same area.

In conclusion, the transport into and out of the resonance zone occurs via a

turnstile [29]: the ionization of an electron occurs when its trajectory maps from the $E_{-1}$

lobe (inside the resonance zone) into $E_0$ lobe (outside the resonance zone). Similarly, the

capture takes place when the $C_0$ lobe (outside the resonance zone) maps into $C_1$ lobe

(inside the resonance zone).

Finally, note that each of the lobes exhibits two horn singularities. The horns

are a consequence of the discontinuities in the kicking $F(t)$. We discuss their origin and behavior in greater detail in Sec. 2.6 and Chapter 3.

## 2.6   Parameter Influence on the Size, Shape and Position of the Turnstile

In this section we show using numerical techniques how different kicking parameters ($\Delta p$, $\tau_k$, and $T$) influence the length and width of the lobes, as well as the size of the horns. This section will show the confirmation of the theoretical results presented later in Chapter 3 by numerically measuring the area of the lobes for several sets of parameter values. (Remember that we only need to measure the area of one of the lobes because all the lobes in our system have the same area.) We will show that the escape lobe width, i.e. the separation between the consecutive intersections along $W^u$ (for example, the length of the unstable manifold creating the bottom border of the $E_{-1}$ lobe in Fig. (2.12)) depends only on the kicking period:

$$\text{Lobe Width} \propto T. \tag{2.15}$$

On the other hand, the lobe length, i.e. the splitting distance between the stable and unstable manifolds (for example, the distance between the stable and unstable manifolds in the middle of the $E_{-1}$ lobe in Fig. (2.12)) depends on both the kick strength and the kicking period. In this section we will only show numerical results for the dependance of the lobe length on $\Delta p$. The results from Chapter 3 will show that the actual dependance

of the lobe width on the kicking parameters has the following functional form

$$\text{Lobe Length} \propto \Delta p / T^{1/3}. \tag{2.16}$$

Thus the area (length times width) of a lobe is proportional to $\Delta p T^{2/3}$. More precisely, we will show analytically in Chapter 3 that the area of a lobe is given to leading order in $\Delta p$ by

$$\text{Lobe Area} \approx 1.404 \Delta p T^{2/3}. \tag{2.17}$$

The parameter values in this chapter are restricted to small kick strengths $\Delta p \ll 1$ and short kick durations $\tau_k \ll T$.

### 2.6.1   Variation of the Kick Duration

For large principal quantum number $n$, electron orbits have very long Kepler periods, and hence away from the nucleus, short kicks behave approximately as delta-functions. To explore the influence of a short, but nonzero, kick duration on the dynamics, we vary $\tau_k$ while keeping the kick strength $\Delta p = \tau_k F_{\max}$ and the total period $T = 2(\tau_k + \tau_s)$ fixed. The numerical results are shown in Fig. (2.13) for decreasing values of $\tau_k$. Figure (2.13d) shows the delta-function limit ($\tau_k = 0$).

Notice first that as $\tau_k$ decreases, the intersections between the stable and unstable manifolds (two of which are marked with black dots in the figure) remain approximately stationary in phase space. We will later show analytically in Chapter 3 that the positions of the intersections depend only on the kicking period $T$ in the limit when $\tau_k \ll T$. Hence the lobe width remains constant with changing $\tau_k$. In addition, the lobe length does not appear to vary with $\tau_k$, except in the close proximity of the horns. Away from the horns
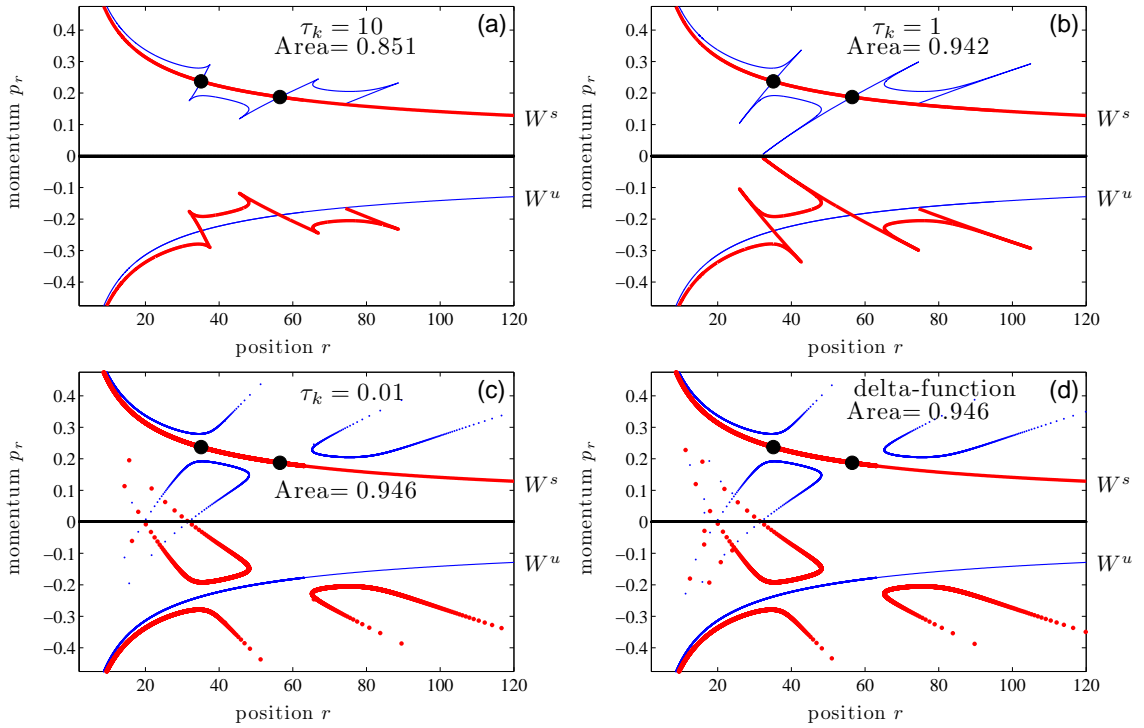
Figure 2.13: The influence of $\tau_k$ on the structure of the homoclinic tangle. The stable manifold $W^s$ is depicted in thick red, and the unstable manifold $W^u$ in thin blue. The final figure (d) corresponds to delta-function kicking. The black dots mark intersections of the stable and unstable manifolds. The kick strength $\Delta p = 0.02$ and kicking period $T = 202$ are kept constant in all four figures. All the figures have been obtained using the same starting point density along $W^s$ and $W^u$ which causes the manifolds to appear "discrete" in figures (c) and (d) because of the elongated horns.

this distance depends only on the kick strength and kicking period (as can be seen in the following subsection), which are kept constant in this numerical experiment. Thus, the width and the length of each of the lobes remains constant, and the numerically measured area of the lobe does not depend on $\tau_k$ for $\tau_k \ll T$. The numerical values of the lobe area can be seen in Fig. (2.13) and are summarized in Table 2.1. These results verify the lack of $\tau_k$ dependance in the Equations (2.15), (2.16), and (2.17).

The primary influence of $\tau_k$ on the size and shape of the homoclinic tangle is on

| $\tau_k$ | Lobe area |
|:---:|:---:|
| 10 | 0.851 |
| 1 | 0.942 |
| 0.01 | 0.946 |
| 0 | 0.946 |

Table 2.1: Area of the lobe as a function of $\tau_k$. The values are associated with Fig. (2.13).

the length of the horns. The horns elongate as $\tau_k$ decreases and actually become infinitely long in the limit of delta-function kicking. However, the horns contribute very little to the total area of the lobe, and hence this singularity is of little physical significance.

Physically, one can understand the behavior of the horns by studying the behavior of the electrons close to the nucleus. Highly excited Rydberg electrons have very long classical Kepler periods. For example, the electron on an energy shell corresponding to the principal quantum number $n = 350$ takes roughly 6.5ns to orbit the nucleus. As we have observed, the area of the lobe and the phase space positions of the intersections between the stable and unstable manifolds do not depend on the kick duration. Hence we use delta-function kicks to understand the behavior of the electrons close to the nucleus. We have mentioned previously that imparting a delta-function kick instantaneously changes the electron's momentum by $\pm\Delta p$, while keeping the electron's distance from the nucleus unchanged. This causes the electron to jump between energy levels. The energy $E$ of the electron is defined as

$$E = \frac{p_r^2}{2} - \frac{1}{r}.$$

Since imparting a delta-function kick instantaneously changes the electron's momentum,

the change in energy immediately after a delta function kick can be written as

$$\Delta E = \frac{\pm 2p_r \Delta p + \Delta p^2}{2},\tag{2.18}$$

where the sign in front of the first term depends on the direction of the imparted kick. Close to the nucleus, the electron's momentum is changing rapidly (electron is either rapidly accelerating or decelerating). Thus if two electrons start on the same energy shell, moving in the same direction and almost equally close to the nucleus, their energies can be drastically different after the application of a delta-function kick. This effect gets magnified with the application of subsequent kicks, and after one iteration of the map (which includes propagation in the Coulomb potential between two subsequent kicks), the two electrons can end very far away from each other in phase space. This in turn causes a drastic elongation of the horns in the case of the delta-function kicks.

As the kick duration increases, a smaller and smaller portion of the imparted kick happens in the region close to the nucleus because the electron is evolving in phase space during the kick application. Since the smaller portion of the kick is imparted in the region of rapid energy change, the horns become shorter, although they never disappear.

### 2.6.2   Variation of the Kick Strength

Next consider the effect of changing the kick strength $\Delta p$ while holding the kick duration $\tau_k$ and the kicking period $T$ constant (Fig. 2.14). Again, the positions of the intersections between the stable and unstable manifolds do not move in phase space, and hence the width of the lobes remains constant with changing $\Delta p$. However, the splitting between the stable and unstable manifolds decreases linearly with decreasing $\Delta p$. This
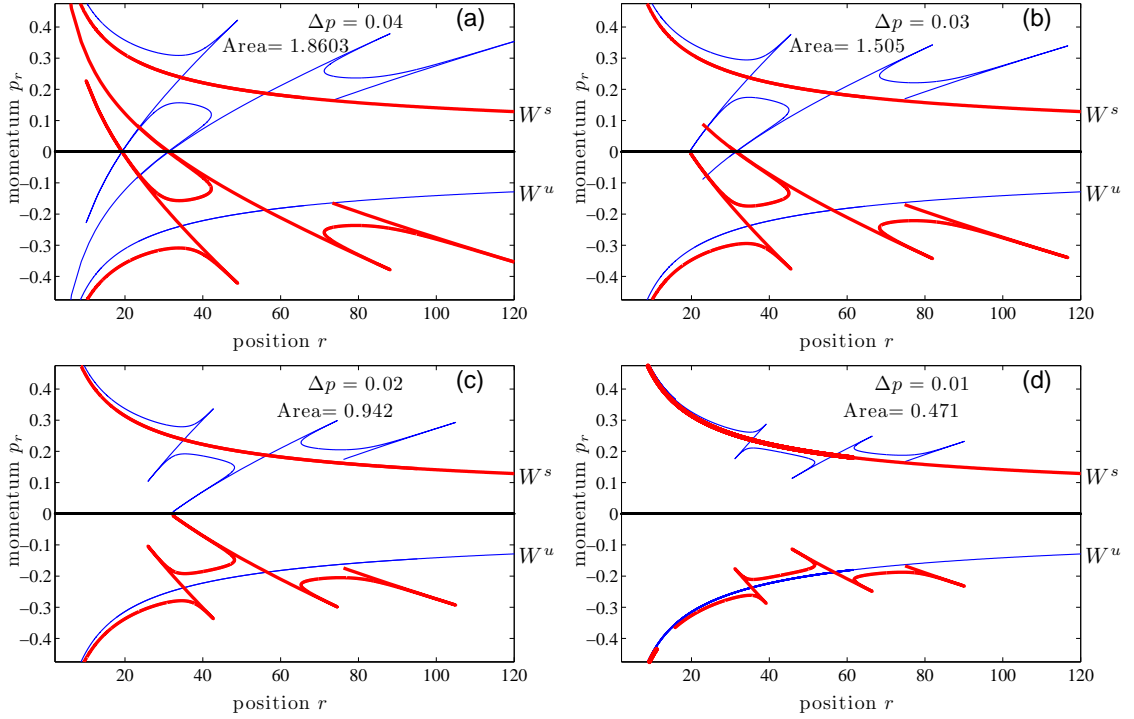
Figure 2.14: The influence of changing the kick strength $\Delta p$ on the size of the lobes in the homoclinic tangle. The kick strength decreases in magnitude from $\Delta p = 0.04$ in figure (a) to $\Delta p = 0.01$ in figure (d). The length of the kick $\tau_k = 1$ and the kicking period $T = 202$ are kept constant in all four figures.

causes a linear decrease in the area of the lobe, which is confirmed by the numerically computed areas shown in Fig. 2.14 and Table 2.2. Thus, these results numerically verify the linear $\Delta p$ dependence in Eqs. (2.16) and (2.17).

| $\Delta p$ | Lobe area |
|------|-------|
| 0.04 | 1.860 |
| 0.03 | 1.505 |
| 0.02 | 0.942 |
| 0.01 | 0.471 |

Table 2.2: Area of the lobe as a function of $\Delta p$. The values are associated with Fig. (2.14).
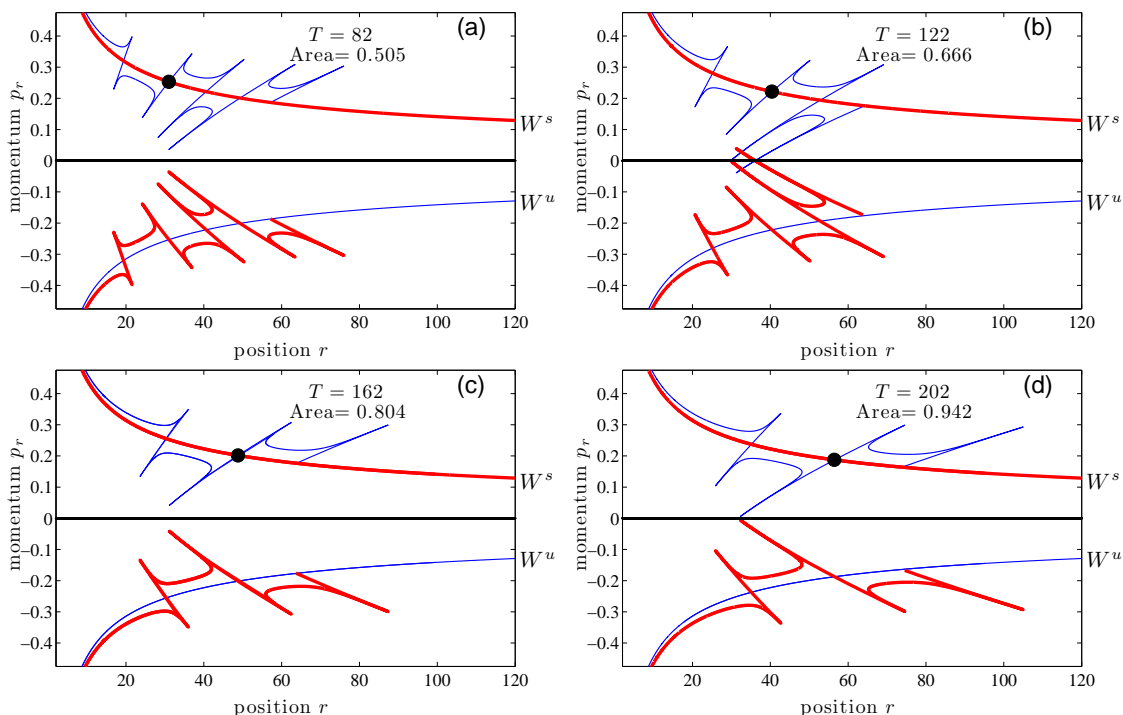
Figure 2.15:   The influence of kicking period $T$ on the lobe area. In figure (a) $T = 82$ ($\tau_s = 40$), and in subsequent figures we increment the value of $T$ by 40, ending with $T = 202$ in figure (d). In all four figures $\Delta p = 0.02$ and $\tau_k = 1$.

### 2.6.3   Variation of the Kicking Period

In the end, we show the influence of the final kicking parameter $T$ on the lobe size and shape. Parameters $\tau_k$ and $\Delta p$ are kept constant, and the kicking period $T$ is adjusted by varying the separation time $\tau_s$ between consecutive positive and negative kicks. Figure (2.15) shows the behavior of the homoclinic tangle for increasing values of $T$. The black dot in each figure is used to guide the eye and marks the intersection between the stable and unstable manifolds just to the left of the $E_1$ lobe. As $T$ increases, the marked intersection (and in fact all intersections) moves away from the nucleus, and furthermore, the lobe widths increase. Hence, though the positions of the intersections do not depend
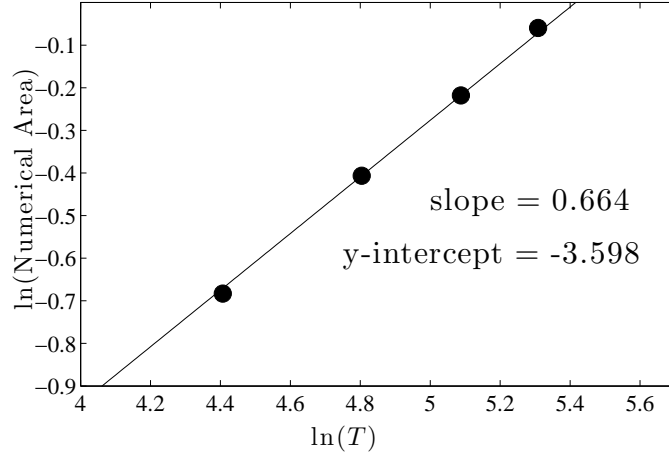
Figure 2.16: The log-log plot of the numerically calculated lobe area versus the kicking period confirms Area $\propto T^{2/3}$. $\Delta p = 0.02$ and $\tau_k = 1$, are held constant.

on $\tau_k$ and $\Delta p$, they do depend on $T$. This is confirmed by Eq. (3.19) in Chapter 3.

Finally, Fig. (2.16) shows a log-log plot of the numerically computed lobe area versus the kicking period $T$ for the data from Fig. (2.15). This plot also shows a line fit to the numerically computed data. The slope of this line is numerically calculated to be equal to 0.664, which is within 1% of the 2/3, thus confirming Lobe Area $\propto T^{2/3}$. The y-intercept of the fitted line is equal to $-3.598$. Using the area expression in Eq. (2.17) along with the numerical value of $\Delta p = 0.02$ from Fig. 2.15, our predicted intercept is $-3.573$, which is also within 1% of the numerical value. Hence we have numerically verified the expression for the lobe area from Eq. (2.17).

# Chapter 3

# Perturbative Analysis of the Homoclinic Tangle Behavior in the Kicked Rydberg System

This chapter describes an analytical method, the Melnikov method [21, 30, 51], used to approximate the lobe geometry in the kicked Rydberg system. We first show a derivation of the Melnikov function which describes the splitting between the stable and unstable manifolds in the presence of kicks. Next we describe how we can use the Melnikov function to understand the behavior of the homoclinic tangle and its dependance on the parameters in the kicked Rydberg system. Since $F_{max} = \Delta p / \tau_k$ and $\tau_s = (T - 2\tau_k)/2$, we again examine only the influence of $\Delta p$, $T$, and $\tau_k$ on the homoclinic tangle. At the end of this chapter we show how to connect the Melnikov function to experimentally observable quantities.

In the absence of any kicks the stable and unstable manifolds attached to the fixed point at infinity coincide with each other and with the separatrix. If one were to pick a generic point along either the stable or unstable manifold (i.e, the separatrix), and then turn on the perturbation (i.e, introduce the kicks in the system), one would notice that at that point the stable and unstable manifolds have separated. The Melnikov method is a perturbative approach for finding the distance between the stable and the unstable manifolds. This distance is described by a Melnikov function. Consequently we can use the Melnikov function to find the intersection points between the stable and unstable manifolds. The intersections are located at zeros of the Melnikov function. Finally, we can also use the Melnikov function to find the area of the lobes by integrating the distance between the stable and unstable manifolds between the two adjacent intersections.

For the modest kick strengths, and kicking periods used in the experimental setups, the Melnikov technique gives excellent agreement with the numerical results, and thus proves to be a powerful tool for determining how the ionization is influenced by changes in the experimental parameters.

## 3.1   Deriving the Melnikov function

The derivation of the expression that measures the splitting in energy between the stable and unstable manifolds starts by rewriting the Hamiltonian from Eq. (2.2) as

$$H = H_0 + H'(t), \tag{3.1}$$
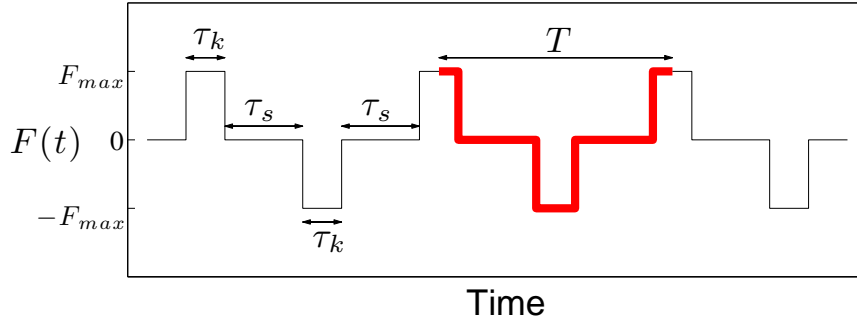
Figure 3.1: The externally applied electric force. The duration of each kick is $\tau_k$ and the separation between consecutive kicks is $\tau_s$. Hence the total kicking period is $T = 2\tau_k + 2\tau_s$. The bold line denotes one cycle of the Poincaré map (the one kicking period). (This is a repeat of Fig. 2.3.)

where $H_0 = p_r^2/2 - 1/r$ is the unkicked Hamiltonian, and $H'(t) = -rF(t)$ is the kicking term. Kicking profile is shown in Fig. (3.1). $F(t)$ can be written as

$$
F(t) = \begin{cases} \frac{\Delta p}{\tau_k} & nT < t < nT + \frac{\tau_k}{2}, \\[2mm] 0 & nT + \frac{\tau_k}{2} < t < nT + \frac{T}{2} - \frac{\tau_k}{2}, \\[2mm] -\frac{\Delta p}{\tau_k} & nT + \frac{T}{2} - \frac{\tau_k}{2} < t < nT + \frac{T}{2} + \frac{\tau_k}{2}, \qquad n \in \mathbb{Z} \\[2mm] 0 & nT + \frac{T}{2} + \frac{\tau_k}{2} < t < nT + T - \frac{\tau_k}{2}, \\[2mm] \frac{\Delta p}{\tau_k} & nT - \frac{\tau_k}{2} < t < nT. \end{cases} \qquad (3.2)
$$

The Melnikov function measures the distance between the stable and unstable manifolds to first order in the strength of the forcing. More precisely, it is the difference in the unperturbed energy $H_0$ between the stable and unstable manifolds. This distance is different from what we have seen in Sec. (2.5) where we first introduced the shape of the homoclinic tangle in the kicked Rydberg system. Figures representing the homoclinic tangle are shown in physical coordinates, whereas the coordinates used in the Melnikov function are canonical energy-time coordinates. The time in the Melnikov function is the time along the unperturbed separatrix where $t = 0$ represents the nucleus. In these

coordinates the lower part of the separatrix ($p_r < 0$) corresponds to $t < 0$, and the upper part of the separatrix ($p_r > 0$) corresponds to $t > 0$. The energy coordinate is found by adding the kinetic and potential energies of a given point in phase space ($E = p_r^2/2 - 1/r$).

We are now ready to write Melnikov function $M(t)$ as

$$M(t) = \int_{-\infty}^{\infty} \{H, H'(t'-t)\} \left(r(t'), p_r(t')\right) dt', \tag{3.3}$$

where the curly brackets denote the Poisson bracket and $(r(t'), p_r(t'))$ is the trajectory that forms the unkicked separatrix [21]. Thus

$$\begin{aligned}
M(t) &= \int_{-\infty}^{\infty} p_r(t') F(t' - t) dt' \\
&= \int_{-\infty}^{\infty} p_r(t + t') F(t') dt' \\
&= \frac{\Delta p}{\tau_k} \sum_{n \in \mathbb{Z}} \int_{nT - \tau_k/2}^{nT + \tau_k/2} p_r(t + t') dt' - \frac{\Delta p}{\tau_k} \sum_{n \in \mathbb{Z}} \int_{(n+1/2)T - \tau_k/2}^{(n+1/2)T + \tau_k/2} p_r(t + t') dt' \\
&= \frac{\Delta p}{\tau_k} \sum_{n \in \mathbb{Z}} r(t + t') \Big|_{t' = nT - \tau_k/2}^{t' = nT + \tau_k/2} - \frac{\Delta p}{\tau_k} \sum_{n \in \mathbb{Z}} r(t + t') \Big|_{t' = (n+1/2)T - \tau_k/2}^{t' = (n+1/2)T + \tau_k/2}. \tag{3.4}
\end{aligned}$$

The next step in deriving the Melnikov function is to find the expression for $r(t)$. Since $r(t)$ measures the position along the unperturbed separatrix, its functional form can be found by remembering that

$$\frac{dr'}{dt'} = \sqrt{2(E - V(r'))},$$

and

$$t = \int_0^r \frac{dr'}{\sqrt{2(E - V(r'))}}, \tag{3.5}$$

where $E = 0$ for the separatrix and $V(r) = -1/r$. Thus

$$t = \int_0^r \frac{dr'}{\sqrt{2/r'}} = \frac{\sqrt{2}}{3} r^{3/2}, \tag{3.6}$$

and hence

$$r(t) = \left(\frac{3}{\sqrt{2}}\right)^{2/3} |t|^{2/3}. \tag{3.7}$$

The above steps lead to the expression for the Melnikov function in the form of an infinite sum:

$$M(t) = \frac{\Delta p}{\tau_k} \left(\frac{9}{2}\right)^{1/3} \sum_{n \in \mathbb{Z}} \left[ \left| t + nT + \frac{\tau_k}{2} \right|^{2/3} - \left| t + nT - \frac{\tau_k}{2} \right|^{2/3} \right.$$
$$\left. - \left| t + \left(n + \frac{1}{2}\right) T + \frac{\tau_k}{2} \right|^{2/3} + \left| t + \left(n + \frac{1}{2}\right) T - \frac{\tau_k}{2} \right|^{2/3} \right]. \tag{3.8}$$

Each term in this infinite sum corresponds to alternating kicks being turned on or off. If we follow the red line marking one period of the map in Fig. 3.1, the first term corresponds to the end of the first positive kick in the map; the second term corresponds to the beginning of the negative kick, the third term marks the end of the negative kick, and the fourth term corresponds to the positive kick turning on.

The next section explores how different parameters influence the behavior of the Melnikov function.

## 3.2 Kicking Parameter Influence on the Melnikov Function Behavior

In the previous section we have derived an expression for the energy splitting between the stable and unstable manifolds for a kicked Rydberg system using the Melnikov function. Melnikov function was expressed in terms of an infinite sum over kicking periods that extend to infinity in both positive and negative time directions. In this section we examine how different kicking parameters ($\Delta p$, $\tau_k$, and $T$) influence the behavior of the Melnikov function.

As a reminder, Melnikov function is given by

$$M(t) = \frac{\Delta p}{\tau_k} \left(\frac{9}{2}\right)^{1/3} \sum_{n \in \mathbb{Z}} \left[ \left| t + nT + \frac{\tau_k}{2} \right|^{2/3} - \left| t + nT - \frac{\tau_k}{2} \right|^{2/3} \right.$$
$$\left. - \left| t + \left(n + \frac{1}{2}\right) T + \frac{\tau_k}{2} \right|^{2/3} + \left| t + \left(n + \frac{1}{2}\right) T - \frac{\tau_k}{2} \right|^{2/3} \right].$$

We first notice that the amplitude of the Melnikov function $M(t)$ depends linearly on $\Delta p$, and hence the splitting between the stable and unstable manifolds has linear dependence on the kick strength (as mentioned in Eq. (2.16) of Sec. 2.6). The dependence on $\tau_k$ and $T$ is not as simple. In order to explore the dependance of the Melnikov function on $\tau_k$ and $T$, we introduce a new parameter

$$\kappa = \frac{\tau_k}{2T}. \tag{3.9}$$

Since the work in this thesis focuses on short pulses ($\tau_k \ll T$), we will later perform a Taylor expansion of the Melnikov function in $\kappa$. Defining $a = t/T$ allows us to rewrite the

Melnikov function from Eq. (3.8) as

$$M(a) = \frac{\Delta p}{2\kappa T^{1/3}} \left(\frac{9}{2}\right)^{1/3}$$

$$\sum_{n\in\mathbb{Z}} \left[ |a+n+\kappa|^{2/3} - |a+n-\kappa|^{2/3} + \right.$$

$$\left. - \left|a+n+\frac{1}{2}+\kappa\right|^{2/3} + \left|a+n+\frac{1}{2}-\kappa\right|^{2/3} \right]. \tag{3.10}$$

Observe that the amplitude of the Melnikov function, i.e. the lobe length, depends on $\Delta p/T^{1/3}$ as mentioned in Sec. 2.6. Furthermore, we can write $M(t)$ in the functional form $M(t) = T^{-1/3}g(t/T)$. Thus, not only does the ampltude of $M$ scale as $T^{-1/3}$, but the horizontal scale of $M(t)$ is proportional to $T$, i.e. multiplying $T$ by a factor of two stretches $M(t)$ by a factor of two in the horizontal direction. This immediately implies that the width of a lobe, defined as the distance beteen two adjacent zeros of $M$, scales as $T$, as cited in Eq. (2.15). The following analysis shows how the actual position of the zeros can be computed.

The Melnikov function exhibits the following symmetries

$$M(-a) = -M(a), \tag{3.11}$$

$$M\left(a+\frac{1}{2}\right) = -M(a). \tag{3.12}$$

This can be both verified analytically in Eq. (3.10) and observed in Fig. 3.2. Due to these symmetries and the fact that $M(a)$ is well defined for all values of $a$, we conclude that its zeros occur whenever $a$ is an integer or half-integer (i.e. when $t$ equals $nT$ or $(n+1/2)T$). Thus, we again see that the width of the lobe scales linearly with kicking period $T$. More-over, for a given value of $T$, the zeros of the Melnikov function are equally spaced so all

the lobes have the same width. This can be reconciled with figures from Chapter 2 depicting the homoclinic tangle in position-momentum coordinates by remembering that the electron that is closer to the nucleus moves faster than the electron that is further away. Hence the distance that the electron closer to the nucleus travels during the same length of time is much longer than the electron that is further away. This causes the lobes closer to the nucleus to be wider than the ones farther away. Since this is a Hamiltonian system, all of the lobes have the same area. Thus, in the physical coordinates, in order to preserve the area of the lobe, the lobes that are further away from the nucleus increase in length to compensate for decrease in their width.

Next we factor out $|a + n|^{2/3}$ from the first two terms in the sum of Eq. (3.10), and $|a + n + 1/2|^{2/3}$ from the last two terms.

$$M(a) = \frac{\Delta p}{2\kappa T^{1/3}} \left(\frac{9}{2}\right)^{1/3} \sum_{n \in \mathbb{Z}} \left[ |a + n|^{2/3} \left( \left|1 + \frac{\kappa}{a + n}\right|^{2/3} - \left|1 - \frac{\kappa}{a + n}\right|^{2/3} \right) \right.$$
$$\left. + \left|a + n + \frac{1}{2}\right|^{2/3} \left( \left|1 - \frac{\kappa}{a + n + \frac{1}{2}}\right|^{2/3} - \left|1 + \frac{\kappa}{a + n + \frac{1}{2}}\right|^{2/3} \right) \right].$$

(3.13)

Furthermore we do a Taylor expansion for small $\kappa$ and we get

$$M(a) = \frac{\Delta p}{2\kappa T^{1/3}} \left(\frac{9}{2}\right)^{1/3} \sum_{n \in \mathbb{Z}} \left[ \frac{4}{3}\kappa \frac{|a + n|^{2/3}}{a + n} - \frac{4}{3}\kappa \frac{|a + n + \frac{1}{2}|^{2/3}}{a + n + \frac{1}{2}} \right] + \mathcal{O}\left(\frac{\kappa^2}{\delta a^{4/3}}\right)$$

$$= \frac{\Delta p}{T^{1/3}} \left(\frac{4}{3}\right)^{1/3} \sum_{n \in \mathbb{Z}} \left[ \frac{|a + n|^{2/3}}{a + n} - \frac{|a + n + \frac{1}{2}|^{2/3}}{a + n + \frac{1}{2}} \right] + \mathcal{O}\left(\frac{\kappa^2}{\delta a^{4/3}}\right)$$

$$= M_1(a) + \mathcal{O}\left(\frac{\kappa^2}{\delta a^{4/3}}\right),$$

(3.14)

where $\delta a$ $(-1/4 \leq \delta a \leq 1/4)$ equals the distance of $a$ from the closest integer or half-
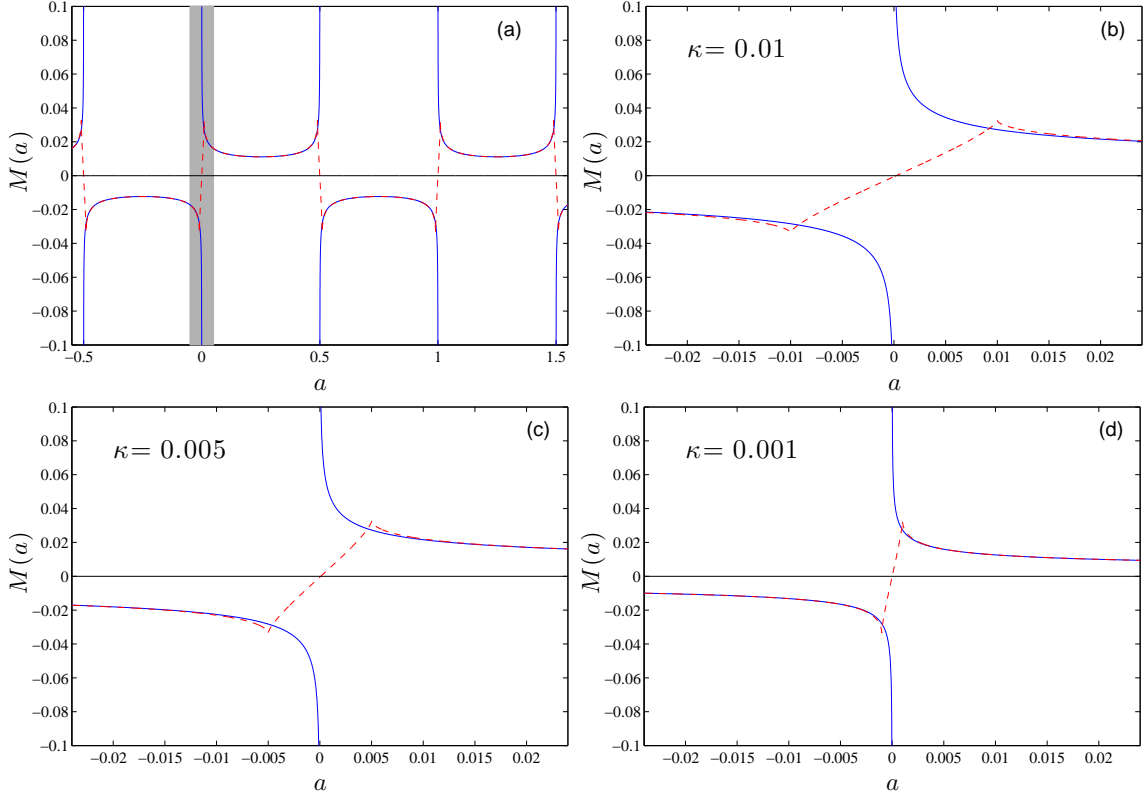
Figure 3.2: Figure (a) shows a few periods of the full Melnikov function $M(a)$ (red dashed line) and the first order approximation $M_1(a)$ (blue solid line). The gray bar marks the expanded region in figures (b), (c), and (d). $\kappa$ decreases as we move from figure (b) to figure (d), while the rest of the parameters are kept constant.

integer, and

$$M_1(a) = \frac{\Delta p}{T^{1/3}} \left(\frac{4}{3}\right)^{1/3} \sum_{n \in \mathbb{Z}} \left[ \frac{|a+n|^{2/3}}{a+n} - \frac{\left|a+n+\frac{1}{2}\right|^{2/3}}{a+n+\frac{1}{2}} \right] \tag{3.15}$$

is the Taylor expansion of $M(a)$ through first order in $\kappa$.

From Eq. (3.15), we see that the function $M_1(a)$ diverges whenever $a$ is either an integer or half-integer. (See Fig. (3.2).) The divergences in $M_1(a)$ are an artifact of the Taylor expansion in Eq. (3.14), which assumes $\kappa \ll |a+n|$ and $\kappa \ll |a+n+1/2|$ for every integer $n \in \mathbb{Z}$, i.e. $\kappa \ll \delta a$; the full expression for $M(a)$ in Eq. (3.10) has no divergences.

The divergences appear as infinitely long horns in $M_1(a)$, while the horns in the full $M(a)$ are of finite length. When $\delta a^{4/3} \approx \kappa^2$, the approximation (3.14) breaks down, and $M_1(a)$ departs from the full Melnikov function $M(a)$. Close to these divergences, the full Melnikov function $M(a)$ does not follow $M_1(a)$, but rather it turns over and passes through zero (Fig. (3.2 b,c,d)). The smaller $\kappa$ is, the closer $M(a)$ tracks $M_1(a)$, and hence the longer are the horns of $M(a)$, with their lengths going to infinity in the limit of delta-function kicks (i.e. $\kappa \to 0$). This phenomenon was already observed in Fig. (2.15) and the physical intuition for its reason was offered in Sec. 2.6.

Now that we understand the behavior of the Melnikov function, we are ready to proceed with calculating the area of the lobes.

## 3.3    Finding the Area of the Lobe

As it was mentioned earlier, the area of the lobe can be calculated by integrating the distance between the stable and unstable manifolds between two adjacent intersections of stable and unstable manifolds. The Melnikov function measures the distance between the stable and unstable manifolds in units of energy, and time is the conjugate variable to energy. Hence, the area of the lobe can be calculated by integrating the Melnikov function between two adjacent zeros

$$\text{Lobe Area} = \int_{t_0}^{t_1} M(t)dt = T \int_{a_0}^{a_1} M(a)da, \tag{3.16}$$

where $a_0$ and $a_1$ are two adjacent zeros of the Melnikov function. Since all the lobes in this system have equal areas, we choose $a_0 = 0$ and $a_1 = 1/2$. Approximating $M(a)$ by

$M_1(a)$,

$$
\begin{aligned}
\text{Lobe Area} &= T \int_0^{\frac{1}{2}} M_1(a) da \\
&= \left(\frac{4}{3}\right)^{1/3} \Delta p T^{2/3} \int_0^{\frac{1}{2}} da \sum_{n \in \mathbb{Z}} \left[ \frac{|a+n|^{2/3}}{a+n} - \frac{\left|a+n+\frac{1}{2}\right|^{2/3}}{a+n+\frac{1}{2}} \right] \\
&= \left(\frac{4}{3}\right)^{1/3} \Delta p T^{2/3} \sum_{n \in \mathbb{Z}} \frac{3}{2} \left[ 2\left|n+\frac{1}{2}\right|^{2/3} - |n+1|^{2/3} - |n|^{2/3} \right] \\
&= 2\left(\frac{9}{2}\right)^{1/3} \Delta p T^{2/3} \sum_{n \geq 0} \left[ 2\left(n+\frac{1}{2}\right)^{2/3} - (n+1)^{2/3} - n^{2/3} \right]. \quad (3.17)
\end{aligned}
$$

The sum in the above expression converges with the rate $1/n^{4/3}$ to 0.4252, and hence

$$
\text{Lobe Area} = 1.404 \Delta p T^{2/3}. \quad (3.18)
$$

Observe that the area of the lobe does not depend on the length of the kicks $\tau_k$ in the case when $\tau_k/T \ll 1$. These are the same results that were observed in numerical calculations presented in Section 2.6 and shown in Figures (2.15) and (2.16).

## 3.4 Finding the Critical Value of the Kick Strength for Which the Lobe Fully Intersects a Given Energy Shell

In the rest of this chapter we focus on using the Melnikov function to make conclusions about experimentally observable quantities. Ionization is defined by the process of transporting from the $E_{-1}$ to $E_0$ lobe. Only the trajectories that are contained inside the $E_{-1}$ lobe ionize after one kicking period. For that reason, we now concentrate on using the Melnikov function to understand the overlap between the starting ensemble used in the experiments and the $E_{-1}$ lobe. Chapter 4 presents the numerical and experimental results

for observing the dependance of the fraction of the electrons that ionizes after application of one pair of positive and negative kicks as a function of the kick strength. Those results show that the ionization fraction as a function of the kick strength exhibits step-function-like behavior. The step occurs when the $E_{-1}$ lobe fully overlaps with the starting energy shell. In this section we present the analytic computation of the critical value of the kick strength at which the step occurs.

The results in this chapter are obtained by treating the kicks as a perturbation to the unkicked separatrix, hence the positions of the intersections between the stable and unstable manifolds can be approximated by finding the points on the unkicked separatrix that have traveled for time $(n/2)T$ ($n \in \mathbb{Z}$) away from the nucleus. The positions of the two closest intersections are obtained by setting $t = \pm T/2$

$$(r, p_r) = \left( \frac{(3T)^{2/3}}{2}, \pm \frac{2}{(3T)^{1/3}} \right).$$ (3.19)

Finally, we can use the expression for the first order Taylor expansion of the Melnikov function in Eq. (3.15) to predict the critical value of the kick strength where the ionization fraction reaches the plateau in Fig. (4.4). The top of the step occurs when the initial ensemble first overlaps with the $E_{-1}$ lobe at the local minimum between the two zeros of the Melnikov function. The Melnikov function describes the distance in energy between the stable and unstable manifolds. The two intersections that define the lobe are separated by half the kicking period. The middle of the lobe occurs one quarter of a period after the intersection to the left/right of it. The initial ensemble has scaled energy

$E = -1/2$, so we conclude that the step occurs when $M_1(1/4) = 1/2$, and thus

$$\Delta p_{\text{critical}} \approx \left(\frac{3T}{32}\right)^{1/3} \left(\sum_{n \in \mathbb{Z}} \left[\frac{|1/4 + n|^{2/3}}{1/4 + n} - \frac{\left|1/4 + n + \frac{1}{2}\right|^{2/3}}{1/4 + n + \frac{1}{2}}\right]\right)^{-1}$$

$$= 0.285 \, T^{1/3}. \tag{3.20}$$

To summarize, for $\Delta p < \Delta p_{critical}$, only the horns overlap with the initial ensemble and the fraction of the ensemble that ionizes is very small. When $\Delta p$ reaches the critical value, the overlap increases drastically which can be observed in the experiment as a rapid increase in the ionization fraction.

## 3.5   Approximating the Slope of the Melnikov Function at $t = 0$

The portion of a given energy shell that ionizes after one map application (i.e. after one kicking period $T$) is the fraction of the energy shell that overlaps with the $E_{-1}$ lobe. The wider the $E_{-1}$ lobe, the larger the overlap and hence, the larger the ionization fraction. For low values of the kick strength $\Delta p$, it is possible to estimate this ionization fraction after one kicking period. In energy-time canonical coordinates, Melnikov function $M(a)$ behavior is rather linear in the vicinity of its zeros. Using the linear approximation to the shape of $M(a)$, one is able to estimate the width of the lobe when it crosses a given energy shell.

In order to find the slope, start with the full Melnikov function

$$M(a) = \frac{\Delta p}{2\kappa T^{1/3}} \left(\frac{9}{2}\right)^{1/3} \sum_{n=-\infty}^{\infty} [|a+n+\kappa|^{2/3} - |a+n-\kappa|^{2/3} - |a+n+\tfrac{1}{2}+\kappa|^{2/3} + |a+n+\tfrac{1}{2}-\kappa|^{2/3}]$$

(3.21)

where $a = \frac{t}{T}$ and $\kappa = \frac{\tau_k}{2T}$ (T is the kicking period, and $\tau_k$ is the length of the kick). In order to connect the results to the physical values, the derivative is performed with respect to time $t$

$$M'(a) = \frac{dM(a)}{dt} = \frac{1}{T}\frac{dM(a)}{da}.$$

Since we are interested in evaluating the derivative at $a = 0$ ($t = 0$), we can assume that $a$ is close to zero while taking the derivative. $\kappa$ is always less than 0.5, and without the loss of generality we can also assume that $|a| \ll \kappa$. There are four terms in the infinite sum that need to be differentiated, while keeping in mind the signs associated with differentiating the absolute value.

First term: $|a + n + \kappa|^{2/3}$

when $n \geqq 0$

$$\frac{d}{da}|a + n + \kappa|^{2/3} = \frac{2}{3}\frac{1}{(a + n + \kappa)^{1/3}}$$

when $n \leqq -1$

$$\frac{d}{da}|a + n + \kappa|^{2/3} = -\frac{2}{3}\frac{1}{|a + n + \kappa|^{1/3}}$$

Second term: $|a + n - \kappa|^{2/3}$

when $n \geqq 1$

$$\frac{d}{da}|a + n - \kappa|^{2/3} = \frac{2}{3}\frac{1}{(a + n - \kappa)^{1/3}}$$

when $n \leqq 0$

$$\frac{d}{da}|a + n - \kappa|^{2/3} = -\frac{2}{3}\frac{1}{|a + n - \kappa|^{1/3}}$$

Third term: $|a + n + \frac{1}{2} + \kappa|^{2/3}$

when $n \geqq 0$

$$\frac{d}{da}|a + n + \frac{1}{2} + \kappa|^{2/3} = \frac{2}{3}\frac{1}{(a + n + \frac{1}{2} + \kappa)^{1/3}}$$

when $n \leqq -1$

$$\frac{d}{da}|a + n + \frac{1}{2} + \kappa|^{2/3} = -\frac{2}{3}\frac{1}{|a + n + \frac{1}{2} + \kappa|^{1/3}}$$

Fourth term: $|a + n + \frac{1}{2} + \kappa|^{2/3}$

when $n \geqq 0$

$$\frac{d}{da}|a + n + \frac{1}{2} - \kappa|^{2/3} = \frac{2}{3}\frac{1}{(a + n + \frac{1}{2} - \kappa)^{1/3}}$$

when $n \leqq -1$

$$\frac{d}{da}|a + n + \frac{1}{2} - \kappa|^{2/3} = -\frac{2}{3}\frac{1}{|a + n + \frac{1}{2} - \kappa|^{1/3}}$$

Putting the above derivatives together and evaluating the expression at $a = t = 0$, results with

$$M'(0) = \frac{\Delta p}{2\kappa T^{4/3}}\left(\frac{9}{2}\right)^{1/3}\frac{2}{3}\left[\sum_{0}^{\infty}\frac{1}{(n + \kappa)^{1/3}} - \sum_{-\infty}^{-1}\frac{1}{|n + \kappa|^{1/3}} - \sum_{1}^{\infty}\frac{1}{(n - \kappa)^{1/3}} + \sum_{-\infty}^{0}\frac{1}{|n - \kappa|^{1/3}}\right.$$

$$\left. - \sum_{0}^{\infty}\frac{1}{(n + \frac{1}{2} + \kappa)^{1/3}} + \sum_{-\infty}^{-1}\frac{1}{|n + \frac{1}{2} + \kappa|^{1/3}} + \sum_{0}^{\infty}\frac{1}{(n + \frac{1}{2} - \kappa)^{1/3}} - \sum_{-\infty}^{-1}\frac{1}{|n + \frac{1}{2} - \kappa|^{1/3}}\right].$$

Grouping the common terms together gives

$$
M'(0) = \frac{\Delta p}{2\kappa T^{4/3}} \left(\frac{9}{2}\right)^{1/3} \frac{2}{3} \left[ \frac{1}{\kappa^{1/3}} + \frac{1}{\kappa^{1/3}} - \frac{1}{(\kappa + \frac{1}{2})^{1/3}} + \frac{1}{(\frac{1}{2} - \kappa)^{1/3}} \right.
$$

$$
+ \sum_1^{\infty} \left[ \frac{1}{(n+\kappa)^{1/3}} - \frac{1}{(n-\kappa)^{1/3}} - \frac{1}{(n+\frac{1}{2}+\kappa)^{1/3}} + \frac{1}{(n+\frac{1}{2}-\kappa)^{1/3}} \right]
$$

$$
\left. + \sum_{-\infty}^{-1} \left[ -\frac{1}{|n+\kappa|^{1/3}} + \frac{1}{|n-\kappa|^{1/3}} + \frac{1}{|n+\frac{1}{2}+\kappa|^{1/3}} - \frac{1}{|n+\frac{1}{2}-\kappa|^{1/3}} \right] \right].
$$

Now make both sums cover the same range

$$
M'(0) = \frac{\Delta p}{2\kappa T^{4/3}} \left(\frac{9}{2}\right)^{1/3} \frac{2}{3} \left[ \frac{2}{\kappa^{1/3}} - \frac{1}{(\kappa + \frac{1}{2})^{1/3}} + \frac{1}{(\frac{1}{2} - \kappa)^{1/3}} \right.
$$

$$
+ \sum_1^{\infty} \left[ \frac{1}{(n+\kappa)^{1/3}} - \frac{1}{(n-\kappa)^{1/3}} - \frac{1}{(n+\frac{1}{2}+\kappa)^{1/3}} + \frac{1}{(n+\frac{1}{2}-\kappa)^{1/3}} \right]
$$

$$
\left. + \sum_1^{\infty} \left[ -\frac{1}{|-n+\kappa|^{1/3}} + \frac{1}{|-n-\kappa|^{1/3}} + \frac{1}{|-n+\frac{1}{2}+\kappa|^{1/3}} - \frac{1}{|-n+\frac{1}{2}-\kappa|^{1/3}} \right] \right].
$$

Next, get rid of the absolute values and combine all the sum terms

$$
M'(0) = \frac{\Delta p}{2\kappa T^{4/3}} \left(\frac{9}{2}\right)^{1/3} \frac{2}{3} \left[ \frac{2}{\kappa^{1/3}} - \frac{1}{(\kappa + \frac{1}{2})^{1/3}} + \frac{1}{(\frac{1}{2} - \kappa)^{1/3}} \right.
$$

$$
+ \sum_1^{\infty} \left[ \frac{1}{(n+\kappa)^{1/3}} - \frac{1}{(n-\kappa)^{1/3}} - \frac{1}{(n+\frac{1}{2}+\kappa)^{1/3}} + \frac{1}{(n+\frac{1}{2}-\kappa)^{1/3}} \right.
$$

$$
\left. \left. + \frac{1}{(n-\kappa)^{1/3}} - \frac{1}{(n+\kappa)^{1/3}} - \frac{1}{(n-\frac{1}{2}-\kappa)^{1/3}} + \frac{1}{(n-\frac{1}{2}+\kappa)^{1/3}} \right] \right].
$$

Adding up the terms gives

$$
M'(0) = \frac{\Delta p}{2\kappa T^{4/3}} \left(\frac{9}{2}\right)^{1/3} \frac{2}{3} \left[ \frac{2}{\kappa^{1/3}} - \frac{1}{(\kappa + \frac{1}{2})^{1/3}} + \frac{1}{(\frac{1}{2} - \kappa)^{1/3}} \right.
$$

$$
\left. + \sum_1^{\infty} \left[ -\frac{1}{(n+\frac{1}{2}+\kappa)^{1/3}} + \frac{1}{(n+\frac{1}{2}-\kappa)^{1/3}} - \frac{1}{(n-\frac{1}{2}-\kappa)^{1/3}} + \frac{1}{(n-\frac{1}{2}+\kappa)^{1/3}} \right] \right].
$$

We can now rearrange the sum to get

$$M'(0) = \frac{\Delta p}{2\kappa T^{4/3}} \left(\frac{9}{2}\right)^{1/3} \frac{2}{3} \left[ \frac{2}{\kappa^{1/3}} - \frac{1}{(\kappa + \frac{1}{2})^{1/3}} + \frac{1}{(\frac{1}{2} - \kappa)^{1/3}} \right.$$

$$+ \sum_{1}^{\infty} \left[ -\frac{1}{(n + \frac{1}{2} + \kappa)^{1/3}} + \frac{1}{(n + \frac{1}{2} - \kappa)^{1/3}} \right]$$

$$+ \left. \sum_{0}^{\infty} \left[ -\frac{1}{(n + \frac{1}{2} - \kappa)^{1/3}} + \frac{1}{(n + \frac{1}{2} + \kappa)^{1/3}} \right] \right].$$

Finally, expand and combine the sums

$$M'(0) = \frac{\Delta p}{2\kappa T^{4/3}} \left(\frac{9}{2}\right)^{1/3} \frac{2}{3} \left[ \frac{2}{\kappa^{1/3}} - \frac{1}{(\kappa + \frac{1}{2})^{1/3}} + \frac{1}{(\frac{1}{2} - \kappa)^{1/3}} \right.$$

$$+ \sum_{1}^{\infty} \left[ -\frac{1}{(n + \frac{1}{2} + \kappa)^{1/3}} + \frac{1}{(n + \frac{1}{2} - \kappa)^{1/3}} - \frac{1}{(n + \frac{1}{2} - \kappa)^{1/3}} + \frac{1}{(n + \frac{1}{2} + \kappa)^{1/3}} \right]$$

$$\left. - \frac{1}{(\frac{1}{2} - \kappa)^{1/3}} + \frac{1}{(\frac{1}{2} + \kappa)^{1/3}} \right].$$

The terms inside the sum cancel and we are left with

$$M'(0) = \frac{\Delta p}{2\kappa T^{4/3}} \left(\frac{9}{2}\right)^{1/3} \frac{2}{3} \left[ \frac{2}{\kappa^{1/3}} - \frac{1}{(\kappa + \frac{1}{2})^{1/3}} + \frac{1}{(\frac{1}{2} - \kappa)^{1/3}} - \frac{1}{(\frac{1}{2} - \kappa)^{1/3}} + \frac{1}{(\frac{1}{2} + \kappa)^{1/3}} \right],$$

which simplifies to

$$M'(0) = \frac{\Delta p}{2\kappa T^{4/3}} \left(\frac{9}{2}\right)^{1/3} \frac{2}{3} \frac{2}{\kappa^{1/3}}.$$

Or finally,

$$M'(0) = \left(\frac{4}{3}\right)^{1/3} \frac{\Delta p}{(\kappa T)^{4/3}}. \tag{3.22}$$

The values from Fig. (3.2) in Section (3.2) are $\Delta p = 0.02$ and $T = 50$. Using the above expression gives the slope 2.77 when $\kappa = 0.01$, 6.99 when $\kappa = 0.005$, and 59.75 when $\kappa = 0.001$. These three values agree with the slope of the full Melnikov function shown in Fig. (3.2). This agreement is also shown in Fig. (3.3), where the red line represents the
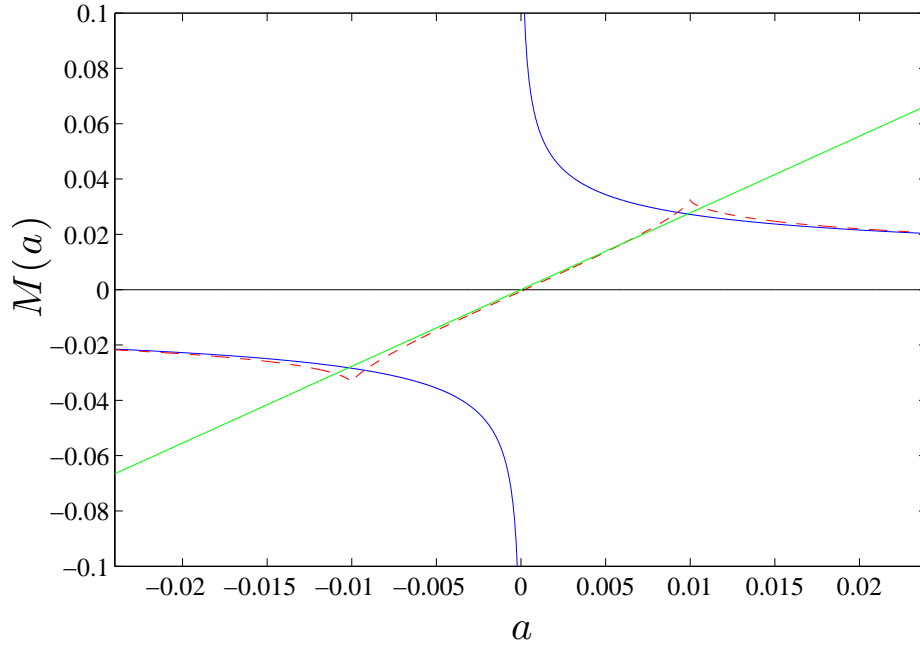
Figure 3.3: The red line represents the full Melnikov function, the blue line is the first order approximation and the green line is the slope we have found using the above approximation for the slope.

full Melnikov function $M(a)$, the blue line is the first order approximation $M_1(a)$, and the green line has the slope calculated from the equation (3.22).

Unfortunately, the experimental values of the kicking period $T$ require the kicking strength $\Delta p$ value to be on the order of 0.4 in order for the $E_{-1}$ lobe to intersect with the energy shell. At this value of $\Delta p$, one cannot use the perturbative method anymore and the width of the $E_{-1}$ lobe does not accurately predict the ionization fraction. However, we are still able to use the knowledge from this chapter to get the physical intuition about qualitative behavior of the ionization fraction as a function of $\Delta p$ and $T$.

## 3.6  Melnikov-Like Function for Single Pair of Positive and Negative Kicks

Chapters 4 and 5 describe the two experiments performed by Barry Dunning's group at Rice University. In the experiment, electron ensembles are exposed to only one iterate of the map, while Melnikov method assumes that the map has been performed infinitely many times in both positive and negative time directions. Hence, in order to better describe the experimental results, we perform a similar analysis as in the beginning of this chapter, but this time assuming only one application of the map. The resulting function is Melnikov-like and instead of producing the homoclinic tangle with infinitely many lobes, it only produces a turnstile responsible for the ionization process.

The forcing $F(t)$ can now be written as

$$
F(t) = \begin{cases}
\frac{\Delta p}{\tau_k} & 0 < t < \frac{\tau_k}{2}, \\[2mm]
0 & \frac{\tau_k}{2} < t < \frac{T}{2} - \frac{\tau_k}{2}, \\[2mm]
-\frac{\Delta p}{\tau_k} & \frac{T}{2} - \frac{\tau_k}{2} < t < \frac{T}{2} + \frac{\tau_k}{2}, \\[2mm]
0 & \frac{T}{2} + \frac{\tau_k}{2} < t < T - \frac{\tau_k}{2}, \\[2mm]
\frac{\Delta p}{\tau_k} & T - \frac{\tau_k}{2} < t < T.
\end{cases}
$$

Again, assuming that $\Delta p$ is small, we can use a perturbative method where the kicks are treated as a perturbation to the unkicked separatrix. The Melnikov-like function $N(t)$ that describes the separation between the stable and unstable manifolds can then be written as

$$
N(t) = \int_{-\infty}^{\infty} \{H, H'(t' - t)\} \left( r(t'), p_r(t') \right) dt',
$$

where the curly brackets denote the Poisson bracket and $(r(t'), p_r(t'))$ is the trajectory that forms the unkicked separatrix. Thus

$$N(t) = \int_{-\infty}^{\infty} p_r(t')F(t'-t)dt'.$$

Since we are only applying one iterate of the map, $F(t) = 0$ for $t < 0$ and $t > T$.

Then using the expression that finds the position along the separatrix as a function of time

$$r(t) = \left(\frac{3}{\sqrt{2}}\right)^{2/3} |t|^{2/3},$$

$N(t)$ can be written as

$$N(t) = \frac{\Delta p}{\tau_k} \left[ r(t+t')\Big|_0^{\tau_k/2} - r(t+t')\Big|_{T/2-\tau_k/2}^{T/2+\tau_k/2} + r(t+t')\Big|_{T-\tau_k/2}^{T} \right].$$

Evaluating $N(t)$ gives

$$N(t) = \frac{\Delta p}{\tau_k} \left(\frac{3}{\sqrt{2}}\right)^{2/3} \left[ |t + \frac{\tau_k}{2}|^{2/3} - |t|^{2/3} - |t + \frac{T}{2} + \frac{\tau_k}{2}|^{2/3} + |t + \frac{T}{2} - \frac{\tau_k}{2}|^{2/3} \right.$$
$$\left. + |t + T|^{2/3} - |t + T - \frac{\tau_k}{2}|^{2/3} \right]$$

$$= \frac{\Delta p}{\tau_k} \left(\frac{9}{2}\right)^{1/3} \left[ |t + \frac{\tau_k}{2}|^{2/3} - |t|^{2/3} - |t + \frac{T}{2} + \frac{\tau_k}{2}|^{2/3} + |t + \frac{T}{2} - \frac{\tau_k}{2}|^{2/3} \right.$$
$$\left. + |t + T|^{2/3} - |t + T - \frac{\tau_k}{2}|^{2/3} \right]$$

$$= \frac{\Delta p}{\tau_k} \left(\frac{9}{2}\right)^{1/3} \left[ |t + \kappa T|^{2/3} - |t|^{2/3} - |t + \frac{T}{2} + \kappa T|^{2/3} + |t + \frac{T}{2} - \kappa T|^{2/3} \right.$$
$$\left. + |t + T|^{2/3} - |t + T - \kappa T|^{2/3} \right],$$

where again $\kappa = \frac{\tau_k}{2T}$. Next we factor out the kicking period by defining $a = \frac{t}{T}$. Thus,

$$
N(a) = \left(\frac{9}{2}\right)^{1/3} \frac{\Delta p T^{2/3}}{\tau_k} \left[ |a + \kappa|^{2/3} - |a|^{2/3} - |a + \frac{1}{2} + \kappa|^{2/3} + |a + \frac{1}{2} - \kappa|^{2/3} \right.
$$
$$
\left. + |a + 1|^{2/3} - |a + 1 - \kappa|^{2/3} \right]
$$
$$
= \left(\frac{9}{2}\right)^{1/3} \frac{\Delta p}{2T^{1/3}\kappa} \left[ |a + \kappa|^{2/3} - |a|^{2/3} - |a + \frac{1}{2} + \kappa|^{2/3} + |a + \frac{1}{2} - \kappa|^{2/3} \right.
$$
$$
\left. + |a + 1|^{2/3} - |a + 1 - \kappa|^{2/3} \right].
$$

The above expression has six terms. Each term represents the kicks turning on and off and it causes a cusp which can be seen in Fig. 3.4. These cusps occur whenever each of the terms in the above expression is equal to zero ($a = -1, -1 + \kappa, -\frac{1}{2} + \kappa, -\frac{1}{2} - \kappa, -\kappa, 0$).

Remember that the zeros of the Melnikov function $M(a)$ occur whenever $a$ is equal to either integer or half integer. Melnikov-like function $N(a)$ is antisymmetric about $a = -\frac{1}{2}$. Hence, the zero of $N(a)$ at $a = -\frac{1}{2}$ coincides with a zero of the Melnikov function. The remaining two zeros of $N(a)$ do not coincide with the corresponding zeros of the Melnikov function. The zero corresponding to the $a = -1$ zero of the Melnikov function, occurs just to the right of it (so $a > -1$ for this zero), and the zero that corresponding to the $a = 0$ zero of the Melnikov function, occurs just to the left of it (so $a < 0$ for this zero). For $a > 0$ and $a < -1$, $N(a)$ quickly approaches zero. Hence, one iterate of the map perturbs the separatrix only close to the nucleus. Away from the nucleus, the kicks do not have much influence on the separatrix.

The function $N(a)$ is a better approximation to the experimental setup than the Melnikov function because in the experiment, the escape is measured as crossing the separatrix instead of mapping from $E_{-1}$ into the $E_0$ lobe. Furthermore, Melnikov function
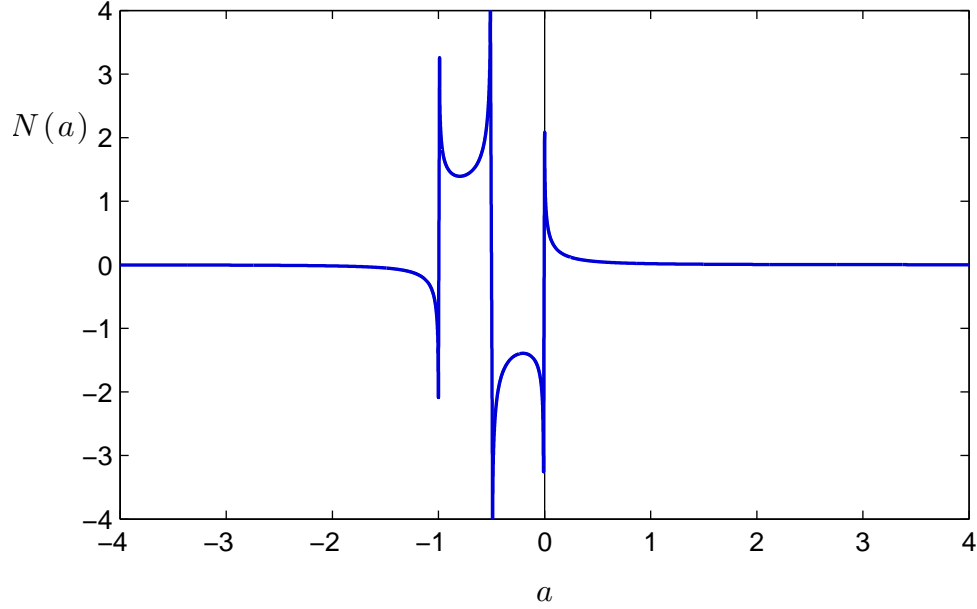
Figure 3.4: Figure shows the plot in energy-time coordinate system of N(a) vs.  a, for $\Delta p = 1.5$, $T = 10$, and $\kappa = 0.01$.

(and the homoclinic tangle approach) are based on the assumption that the kicks extend to infinity in both time directions. This idealized situation is impossible to achieve in the experiment, and the experiments are performed by applying only one kicking period to the starting distribution. However, $N(a)$ does not deviate much from the turnstile portion of the actual homoclinic tangle, so we are still justified to use the full homoclinic tangle approach when designing the experiments and explaining their results.

Melnikov-like function is useful because it can explain the ionization fraction behavior for small values of $\Delta p$. In the proposed experiment discussed in Chapter 4, the value of $\tau_k$ is fixed, and for a given period $T$ we are interested in how the ionization fraction changes as a function of $\Delta p$. Numerical and experimental data in Chapter 4 show that for small values of $\Delta p$ the ionization fraction has the same dependance on $\Delta p$ (the curves

actually fall on top of each other) for all values of the kicking period $T$. This can be explained by observing that the beginning of the rise in the ionization fraction is due to the overlap between the horns with the starting energy shell. In the case when we are considering infinitely many kicks, in the energy-time coordinate system, all the lobes are symmetric about the line going through their midpoint. This is not true anymore in the $N(a)$ (or $N(t)$) case. Now, the horns closest to $a = -\frac{1}{2}$ zero are longer than the rest of them, and hence, they are the first ones to intersect the starting energy shell and are thus the ones that first trigger the rise in the ionization fraction. As $\Delta p$ increases, the second horn extends enough that it also starts intersecting the energy shell and thus adds to the ionization fraction rise. Hence, the initial rise in the ionization fraction is governed by the behavior of $N(a)$ close to the tip of the horn, or the cusp.

In order to understand the behavior of the ionization fraction, we need to understand the behavior of the width of the horn close to the cusp. We start with

$$N(t) = \frac{\Delta p}{\tau_k} \left(\frac{9}{2}\right)^{1/3} \left[ |t + \frac{\tau_k}{2}|^{2/3} - |t|^{2/3} - |t + \frac{T}{2} + \frac{\tau_k}{2}|^{2/3} + |t + \frac{T}{2} - \frac{\tau_k}{2}|^{2/3} \right. $$
$$\left. + |t + T|^{2/3} - |t + T - \frac{\tau_k}{2}|^{2/3} \right].$$

Locally, only the term that produces the cusp is influencing the width of the horn. Hence, we pick one of the terms from the above expression and treat the rest of the terms as a constant. Now, $N(t)$ can be written as

$$N(t) = C_1 \left[ C_2 - |t + \frac{T}{2} + \frac{\tau_k}{2}|^{2/3} \right],$$

where $C_1$ and $C_2$ are constants that represent the rest of the terms. In order to study the ionization process, we set $N(t)$ to $1/2$, which is equal to the energy of a starting
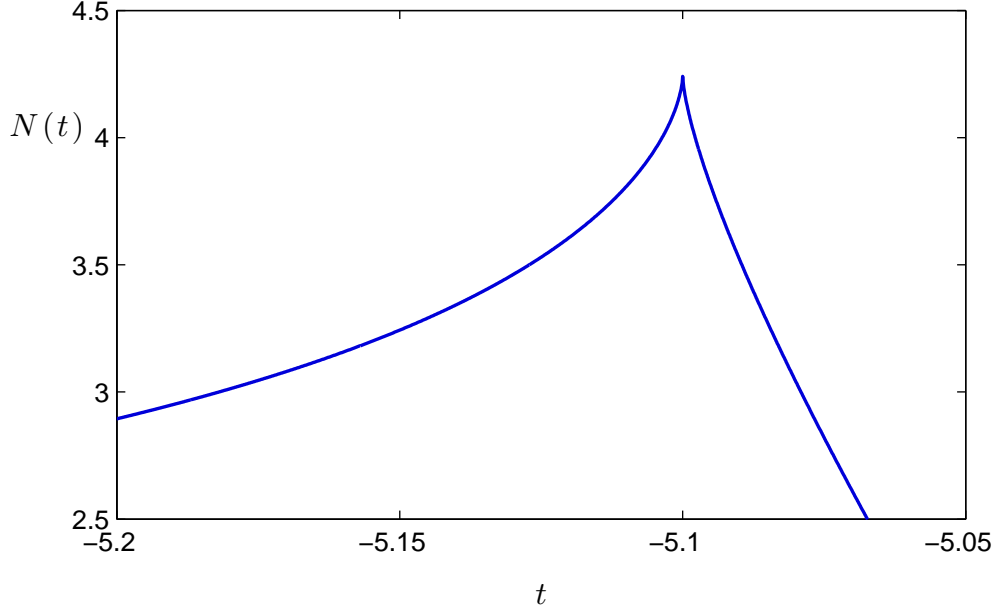
Figure 3.5: Figure a shows the plot in energy-time coordinate system of N(t) vs. t of a cusp just to the left of the $a = -\frac{1}{2}$ $(t = -5)$ zero. The parameters used are the same as in Fig. (3.4) $T = 10$, $\Delta p = 1.5$, and $\tau_k = 0.2$ (which is equivalent to $\kappa = 0.01$).

energy shell. Zoomed in plot of a cusp is shown in Fig. 3.5. The cusp then intersects the energy shell at the time coordinate equal to $-\left(\frac{T}{2} + \frac{\tau_k}{2}\right)$. Notice that the position of the intersection is independent of the kicking strength $\Delta p$. Furthermore, changing the kicking period $T$ does not change the width of the cusp. Rather, it only changes its position in time. Hence for a fixed value of kicking length $\tau_k$, the behavior of the initial rise in the ionization fraction is independent of the kicking period or the kicking strength. Once the kick strength increases enough that the second cusp begins to overlap with the energy shell, the analysis does not change because the position of one cusp is independent of the positions of the rest of the cusps. The same is true for the local behavior of the width of the horn in the vicinity of the cusp. When the second cusp starts to overlap with the line of constant energy representing the energy shell, the ionization fraction increases faster

because the contributions of the two cusps add together, but the overall behavior is still independent of the kicking period and the kicking strength. Hence, we have an analytic explanation for the independence of the initial rise in the ionization fraction on the kicking period $T$.

# Chapter 4

# Experiment Involving a Stationary Ensemble

In this chapter we use a stationary ensemble as an initial condition that allows us to observe the numerical and experimental signature of the dependance of the lobe length on the kicking strength. We narrow our parameter space to experimentally realistic parameter values as determined from [16, 31, 39, 45, 46, 52, 53, 54, 55]. This restricts the shortest separation $\tau_s$ between successive positive and negative kicks to a few nanoseconds and the shortest kick duration $\tau_k$ to 500-600ps. The experiment is performed by exposing the electronic state to one kicking period after which we measure the fraction of electron trajectories that ionize. We show and explain how this ionization fraction depends on the kick strength $\Delta p$ and kicking period $T$. This chapter is organized as follows. In Section 4.1, we introduce scaled coordinates used throughout this thesis. Section 4.2 briefly describes the experimental setup used in this chapter as well as in Chapter 5. Section 4.3

presents numerical calculations used to guide the experiment, while Section 4.4 shows the

experimental results obtained by Barry Dunning's group at Rice University in Houston.

## 4.1 Scaled Coordinates

The first step in both numerical and experimental protocols is to place the atom

in a highly excited Rydberg energy eigenstate, with eigenenergy $\tilde{E}_n = -1/2n^2$ in atomic

units, and principal quantum number $n = 306$ or $n = 350$. Next, we apply a series of

kicks, to be described below. In describing the subsequent evolution of this system under

the kicks, it is convenient to remove the explicit dependance on the principal quantum

number $n$ of the initial Rydberg state. We thus define scaled variables

$$E = n^2 \tilde{E}, \tag{4.1}$$

$$r = \frac{\tilde{r}}{n^2}, \tag{4.2}$$

$$p_r = n\tilde{p}_r, \tag{4.3}$$

$$t = \frac{\tilde{t}}{n^3}, \tag{4.4}$$

where the variables with tildes on the right are the original physical quantities in atomic

units. In scaled variables the energy of the initial Rydberg state is thus simply $E_n = E =$

$-1/2$. In most of what follows in this thesis we present $\Delta p$ and $E$ in scaled units, while

for physical intuition we report time in seconds.

## 4.2 Experimental Setup

The experiments presented in this chapter and in Chapter 5 were performed at Rice University in Houston by Barry Dunning, Shuzhen Ye, and Brendan Wyker. Figure (4.1) shows the sketch of the experimental setup. A thick black line represents the box that isolates the experiment from stray external electric and magnetic fields. A beam of alkali atoms, shown as a gray strip, is shot inside the box. A laser beam, shown as a darker gray circle, perpendicular to the beam of atoms is used to create highly excited Rydberg atoms by photoexciting potassium atoms to selected $n\ell$ states ($n = 306$, $\ell = 2$ or $n = 350$, $\ell = 2$). The atoms are excited near the center of the cavity, where the electrons are exposed to periodic alternating positive and negative kicks. The kicks are produced
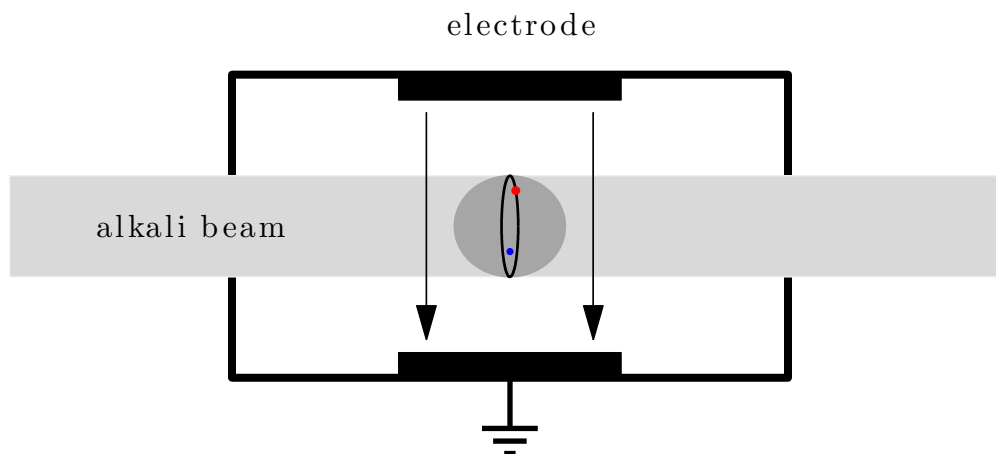


Figure 4.1: A (gray) beam of alkali atoms is shot inside a cavity. A laser beam (darker gray circle) used to photoexcite the electrons is perpendicular to the beam of atoms. A highly excited quasi-one-dimensional Rydberg atom is formed at the center of the cavity where it is exposed to kicks created by a uniform electric field (black arrows). The electric field is a product of applying positive or negative potentials to the electrode at the top of the cavity. Red dot represents a highly excited Rydberg electron and a blue dot represents the core.

by applying positive or negative potentials to the electrode on top of the cavity. The electrode together with the grounded plate at the bottom of the cavity acts as a capacitor and creates a uniform electric field in the center of the cavity. The direction of the electric field depends on the sign of the potential applied to the electrode. A sketch of a highly excited quasi-one-dimensional Rydberg atom is shown using the same convention as in Fig. (2.1) of Chapter 2 (the nucleus is represented by a blue dot, and a Rydberg electron is shown as a red dot). The major axis of the ellipse describing the electron orbit is aligned with the electric field used to apply positive or negative kicks to the electron. After the application of positive and negative kicks, the number of the surviving Rydberg atoms is measured using selective field ionization. This number is then converted either into a survival probability (number of Rydberg electrons that did not get ionized divided with total number of Rydberg electrons at the beginning of the experiment) or the ionization fraction (one minus the survival probability). This experimental setup is described in full detail in the paper by Tannian *et al* [46].

A sketch of the kicking sequence corresponding to one map iterate is shown in Fig. (4.2). In order to stay as close to the impulsive regime (where the duration of the kicks is short in comparison to the classical Kepler period of the starting energy shell), the length of the kicks is kept at 600ps, which is the current lower limit for the uniform kick profile in the experiment. Since it is not possible to probe the system in the middle of the kicks, we adjust the kicking sequence so that the positive kicks are half as tall as the negative kick instead of being half as long. This keeps the overall impulse imparted during the positive kicks the same as in one iterate of the map shown in Fig. (2.3).
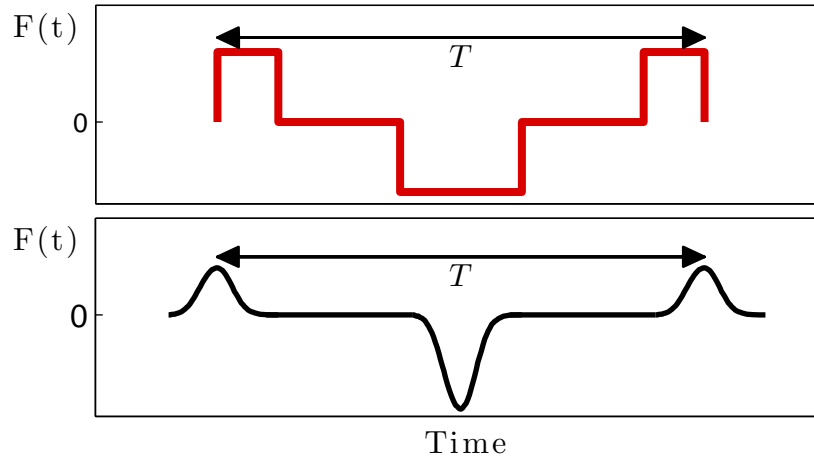
Figure 4.2: The top figure shows the kick profile used in 1D classical simulations, and the bottom figure shows the sketch of the kicking sequence applied in the experiment and used in 3D simulations.

## 4.3 Dependence of Ionization on the Lobe Length

As we have observed earlier in Sec. 2.6.2, increasing $\Delta p$ increases the splitting between the stable and unstable manifolds. In this section, we simulate the experiment described in the previous section and give predictions about the trends in the experimental data that show the signature of the dependance of the lobe length on the kicking strength. Since the initial state is highly excited (either $n = 306$ or $n = 350$), we are justified in adopting a classical model in which the initial state is represented by an invariant classical distribution on the energy shell $E = -1/2$. We expose this state to one kicking period and measure the fraction $f$ of the electron trajectories that ionize. Recall that ionization corresponds to mapping from the $E_{-1}$ lobe to the $E_0$ lobe (Fig. 2.12) [1]. Hence, the only trajectories that ionize after one kicking period are the ones that start within the $E_{-1}$

---

[1]For the simulations in Figs. 4.4, 4.8, 5.3 and 5.4, we say that a trajectory has ionized if $E > 0$ which is experimentally relevant criterion. This criterion is almost the same as saying that a trajectory has ionized when it resides in any of $E_0$, $E_1$, $E_2$, ... because the upper (stable) boundary of the resonance zone (Fig. 2.12) is nearly indistinguishable from the line $E = 0$.
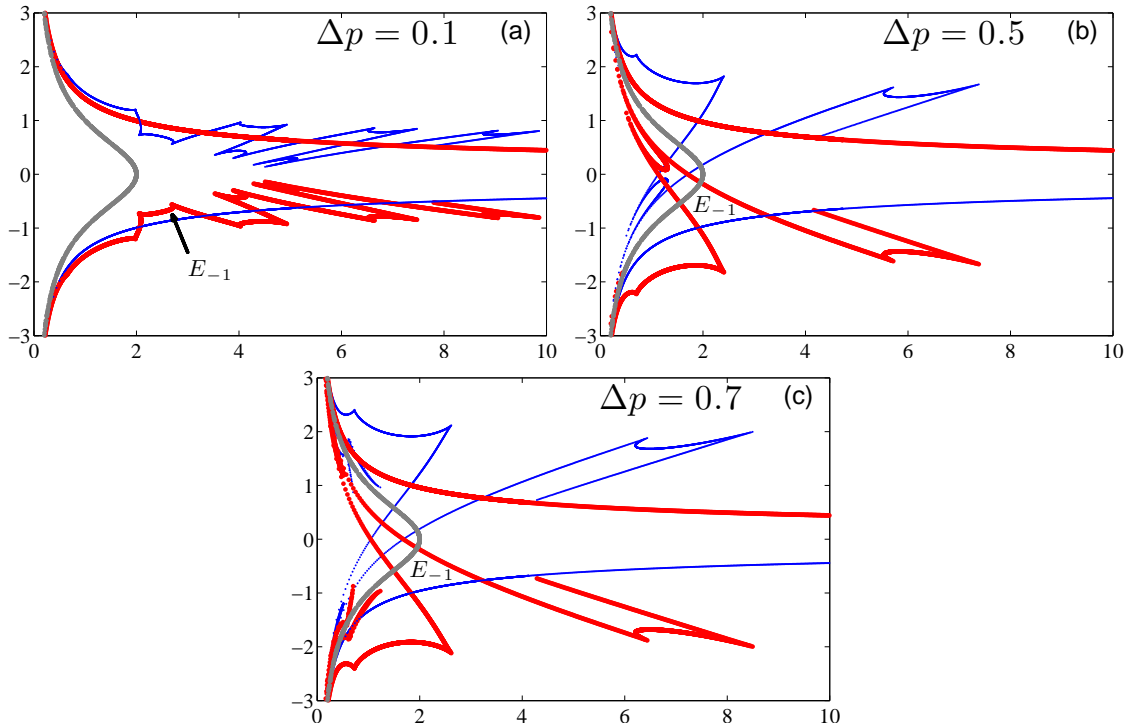
Figure 4.3: For all three figures $\tilde{\tau}_k = 500$ps and $\tilde{T} = 3$ns. The gray curve represents the invariant classical distribution on the energy shell $E = -1/2$ corresponding to $n = 350$ state. For clarity, only the escape lobe $E_{-1}$ is labeled.

lobe. If the starting ensemble does not overlap with the $E_{-1}$ lobe, no trajectories ionize after one kicking period.

### 4.3.1  Short kicking periods

In Fig. (4.3) we show the initial ensemble along with the homoclinic tangle for three values of increasing kick strength with $\tilde{\tau}_k = 500$ps ($\tau_k = 0.482$ in scaled coordinates) and $\tilde{T} = 3$ns ($T = 2.893$ in scaled coordinates). For $\Delta p = 0.1$ there is no overlap between the $E_{-1}$ lobe and the starting distribution. Hence no trajectories are ionized after one kicking period. Increasing $\Delta p$ to 0.5 increases the splitting between the stable and unstable
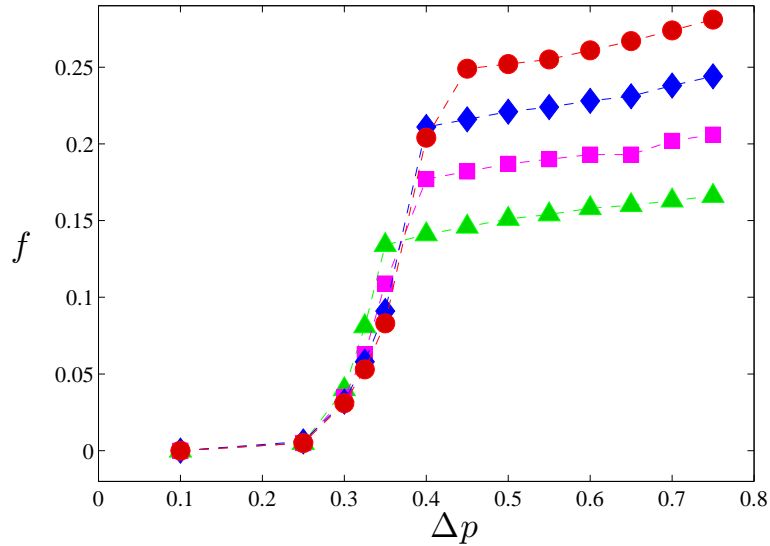
Figure 4.4: The figure shows the fraction of ionized electron trajectories $f$ after one kicking period versus $\Delta p$ for $\tilde{T} = 2.5$ns ($\triangle$), $\tilde{T} = 3$ns ($\square$), $\tilde{T} = 3.5$ns ($\diamond$), and $\tilde{T} = 4$ns ($\bigcirc$); $\tilde{\tau}_s = 500$ps and the starting energy shell $n = 350$ are kept constant.

manifolds so that the $E_{-1}$ lobe intersects the starting distribution. Further increase in $\Delta p$

to 0.7 does not drastically change the overlap between the $E_{-1}$ lobe and the starting

distribution.

In Fig. (4.4) we show the quantitative influence of the changing kick strength

on the ionization fraction. We choose four different $T$ values, and for each $T$ value we

incrementally increase $\Delta p$ from 0.1 to 0.75. For all four sets of data, one observes a sharp

transition in the ionization fraction. For example, following the data set that corresponds

to $\tilde{T} = 3$ns, we notice that for low values of $\Delta p$ the ionization fraction is very small or zero.

At these low values of $\Delta p$, there is no significant overlap between the starting distribution

and the $E_{-1}$ lobe (see Fig. 4.3a). However, around $\Delta p = 0.25$ we notice the onset of a

sharp increase in the ionization fraction. The onset is a signal that the length of $E_{-1}$ has

increased to the point that it is beginning to overlap the starting distribution. Initially,

only the very tips of the horns overlap with the starting distribution. As the kick strength

increases, the length of the lobe also increases and the starting distribution intersects the

$E_{-1}$ lobe closer to the main body of the lobe. At the critical value of $\Delta p_{\text{critical}} = 0.4$, the

starting distribution passes through the dip between the two horns. (The dip occurs at the

local minimum in the separation between the stable and unstable manifolds.) At $\Delta p_{\text{critical}}$

the ionization fraction reaches a plateau. Once the ionization fraction reaches the plateau,

it continues to increase, but at a much slower rate than during the sharp increase. Even

though the kick strength does not influence the width of the lobe, increasing $\Delta p$, does

change the relative position along the lobe where the overlap happens. For larger values

of $\Delta p$ the overlap occurs at the wider part of the $E_{-1}$ lobe, resulting in slight increase in

ionization fraction. This increase is very small for a large window of kick strength values.

For $\tilde{T} = 3$ns, the ionization fraction increases from $f = 0.177$ at $\Delta p = 0.4$ to $f = 0.2$ at

$\Delta p = 0.75$. For practical purposes, we thus view the ionization fraction as exhibiting a

step-function-like behavior as a function of kick strength. Later throughout the text for

this reason we refer to this experiment as the step-function experiment.

As we have already mentioned in Chapter 3, the critical kick strength signals that

the $E_{-1}$ lobe overlaps with the starting energy shell even in the region where the splitting

between the stable and unstable manifolds is the smallest. Section 3.4 showed that the

value of the critical kick strength can be analytically expressed as

$$\Delta p_{\text{critical}} = 0.285 \, T^{1/3}. \tag{4.5}$$

Looking back at Fig. (4.4), notice that the critical value of the kick strength is smaller for

$\tilde{T} = 2.5$ns than for $\tilde{T} = 4$ns, i.e., the electrons exposed to the shorter kicking period reach

the ionization fraction plateau before the ones exposed to the longer kicking period. We can use the above expression to find the $\Delta p_{\text{critical}}$ for the four values of the kicking period shown in Fig.(4.4). For $\tilde{T} = 2.5$ns, $\Delta p_{\text{critical}} = 0.382$, for $\tilde{T} = 3$ns, $\Delta p_{\text{critical}} = 0.406$, for $\tilde{T} = 3.5$ns, $\Delta p_{\text{critical}} = 0.427$, and for $\tilde{T} = 4$ns, $\Delta p_{\text{critical}} = 0.447$, which is in a good agreement with Fig. (4.4).

Along with the value of the critical $\Delta p$, the plateau height is also different for different kicking periods. In Sec. 2.6.3 and Sec. 3.2 we have seen that the lobe width depends linearly on $T$. Thus, the larger the kicking period, the larger the overlap between the $E_{-1}$ lobe and the energy shell, and consequently, a larger fraction of the electron trajectories ionizes after one kicking period. The signature of this phenomenon manifests itself in the linear dependance on $T$ of the ionization fraction value at the plateau. This can also be observed in Fig. (4.4).

### 4.3.2 Long kicking periods

Experimentally it is very hard to produce true square shaped pulses. The full width at half maximum of the pulses used in experiment is 600ps, meaning that the time over which the electrons are being kicked is much longer. Hence, any kicking period smaller than 5ns does not allow the electrons to evolve for a very long time between two consecutive kicks. For that reason, we now show how the ionization fraction behaves as a function of $\Delta p$ and $T$, for $T \geq 5$ns. Figure (4.5) shows the behavior of the ionization fraction as a function of $\Delta p$ and $\tilde{T}$ for $n = 306$ starting energy shell and Fig. (4.6) shows the similar results for $n = 350$ energy shell.
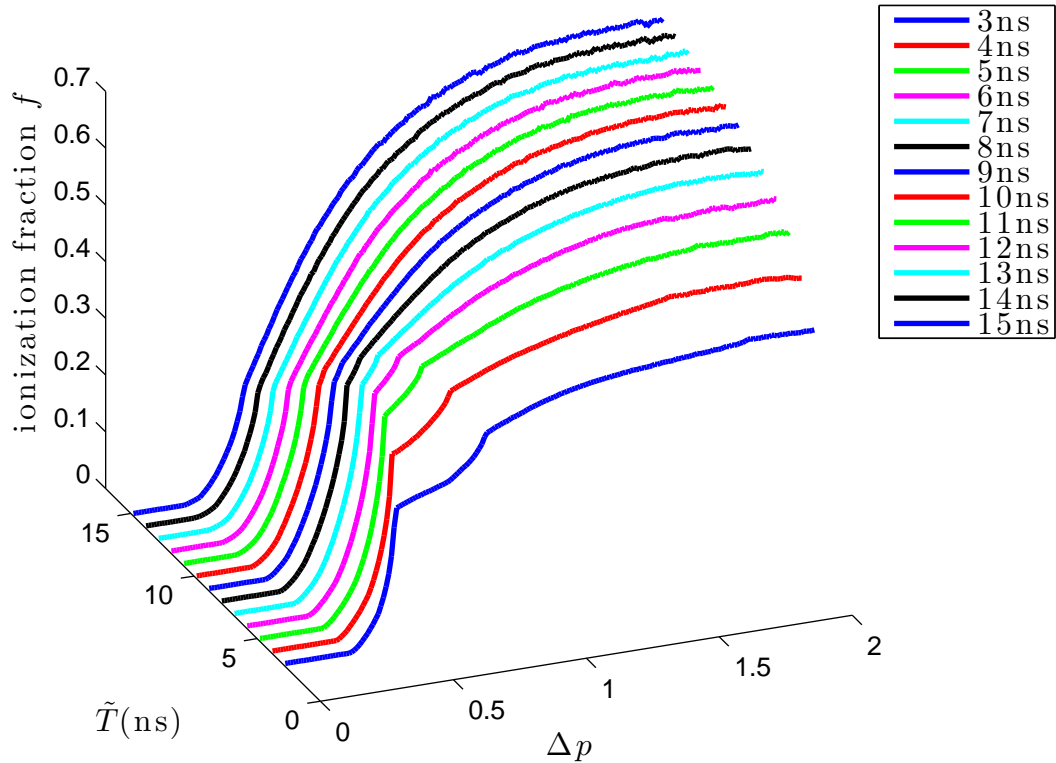
Figure 4.5: The figure shows the fraction of ionized electron trajectories $f$ after one kicking period versus $\Delta p$ for $\tilde{T}$ ranging from 3ns, to 15ns. $\tilde{\tau}_s = 500$ps and the starting energy shell $n = 306$ are kept constant.

The following trends can be observed in the Figs. (4.5) and (4.6): (i) for small values of the kicking period $T$, the ionization fraction resembles a step-function, with an initial rapid rise, followed by a sharp transition (at the shoulder) into a much more gradually rising plateau; (ii) for larger values of $T$, the sharp transition at the shoulder becomes more subtle, and eventually disappears; (iii) at a given kick strength, the ionization fraction increases with increasing $T$; (iv) the sharp transition at the shoulder moves to larger kick strength and larger ionization fraction as $T$ increases; and (v) the initial shape of the rise of the curve up to the shoulder is largely independent of $T$.
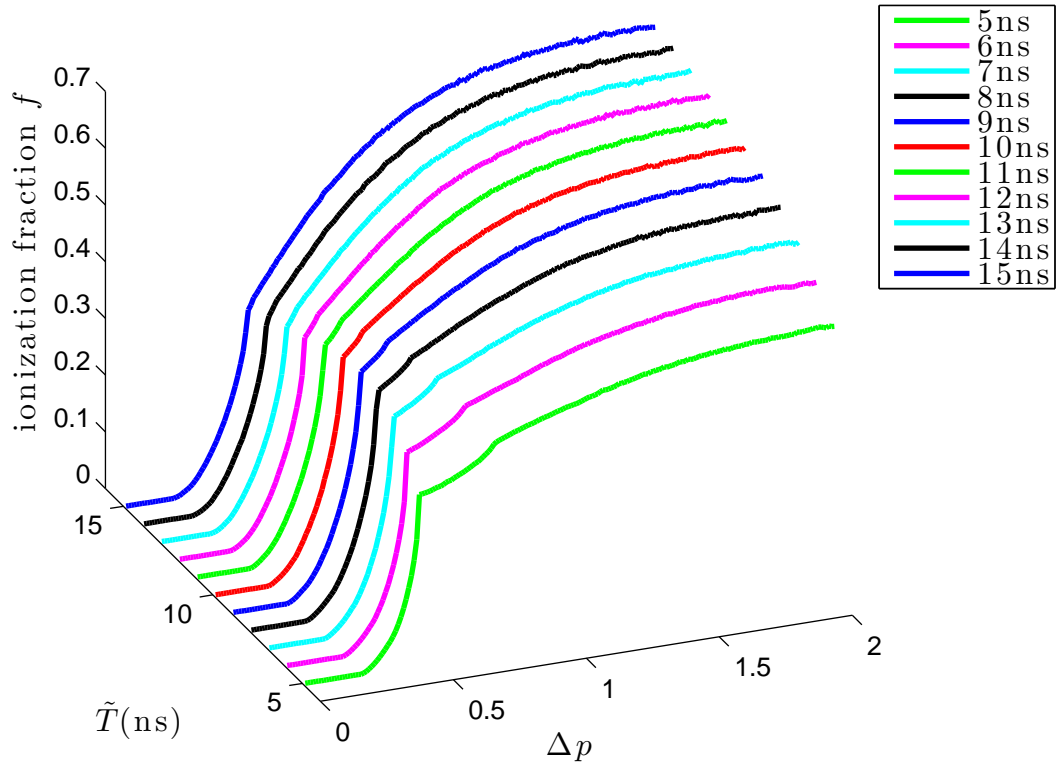
Figure 4.6: The figure shows the fraction of ionized electron trajectories $f$ after one kicking period versus $\Delta p$ for $\tilde{T}$ ranging from 5ns, to 15ns. $\tilde{\tau}_s = 500$ps and the starting energy shell $n = 350$ are kept constant.

Trends mentioned in (i), (iii), and (iv) have already been explained in the previous section, while trend (v) has been explained using Melnikov-like analysis for application of a single map iterate to an energy shell in Section 3.6. We now proceed to explain the disappearance of the shoulder for large values of the kicking period.

As it has been mentioned in Sections 2.6 and 3.2, increasing $T$ increases the width of the lobe. Figure (4.7) shows the overlap of the $E_{-1}$ lobe with an energy shell (a thick black line) in energy-time canonical coordinates. Energy corresponds to the energy $E = p_r^2/2 - 1/r$ of a given, while the time coordinate represents the time it takes for
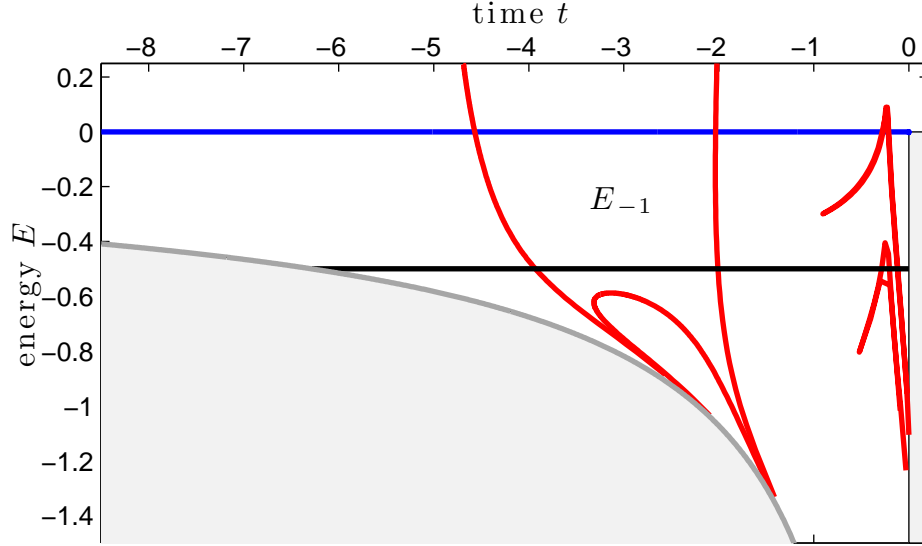
Figure 4.7: Overlap between an energy shell and the $E_{-1}$ lobe in energy-time canonical coordinates.

that point to reach the nucleus, which is set at $t = 0$. The motion along an energy shell then corresponds to moving from left to right where the points $t = 0$ and the point on the gray boundary are identified and correspond to electron bouncing off the nucleus. In these coordinates the Kepler period of the energy shell with $E = -1/2$ represented by the thick black line is $2\pi$. The portion of the energy shell that ionizes after one map iteration corresponds to the portion of the black line that overlaps with the $E_{-1}$ lobe. The region shaded gray in Fig. (4.7) represents the forbidden region for an electron on a given energy shell. Hence, all the lobes also have to fit inside the unshaded region.

As $T$ increases, the $E_{-1}$ lobe moves to the left and becomes wider. At the same time the ratio of the widths of the two horns moves away from unity, with the horn closer to the nucleus becoming wider with respect to the horn further away from the nucleus. The onset of this phenomenon can be seen in Fig. (4.7). Thus, as $\Delta p$ increases and lengthens

the $E_{-1}$ lobe, the energy shell first intersects with the lobe closer to the nucleus, then at an even higher value of $\Delta p$, it starts to intersect with the horn further away from the nucleus. Finally, at the critical value of $\Delta p$ the energy shell intersects with the $E_{-1}$ lobe at the dip in the middle of the lobe. As the discrepancy in the widths of the two horns increases, the horn closer to the nucleus contributes more and more to the total ionization fraction, causing a gradual increase in the overlap between the initial ensemble and the $E_{-1}$ lobe. This phenomenon is responsible for the disappearance of the shoulder present in the ionization fraction for short $T$ values. The critical value of $T$ at which this phenomenon happens occurs roughly when $T$ reaches the value equal to twice the Kepler period of the starting energy shell. This is confirmed by the numerical results shown in Figs. (4.5) and (4.6), which show that the shoulder in $n = 306$ data disappears for a lower value of $T$ than it does for $n = 350$ data. (The Kepler period of $n = 306$ energy shell is 4.35ns, while for $n = 350$, the Kepler period is equal to 6.52ns.)

### 4.3.3   Observing the signature of $E_{-n}$ lobes, with $n \geq 2$

Next we consider exposing the initial state to multiple kicking periods. In Fig. (4.8a), we show the number of kicking periods $N$ needed to escape the resonance zone versus the starting momentum along an energy shell. This figure shows only a small range of momenta because the electron momentum along the starting energy shell takes on values between $\pm\infty$. We avoid this problem in Fig. (4.8b), where we plot $N$ versus the time $t$ it takes a trajectory to move from the right classical turning point to the point on the energy shell. (We choose zero of time to be the right classical turning point.) The

Kepler period of the $n = 350$ energy shell is 6.5ns, so the time ranges between $-3.25$ns and 3.5ns. We now focus on Fig. (4.8b). At every value of $N$ there exists at least one interval that corresponds to an intersection of the energy shell with $E_{-N}$ ($N \geq 1$) and that escapes from the resonance zone after $N$ kicking periods. Notice the existence of large continuous intervals that escape for low values of $N$. At $N = 1$ there is one long interval which corresponds to the intersection between the energy shell and $E_{-1}$, as shown in Figs. (4.3b) and (4.3c). This segment corresponds to the observed ionization fraction $f = 0.177$ at the critical value of kick strength in Fig. (4.4). At $N = 2$, there is another long segment along
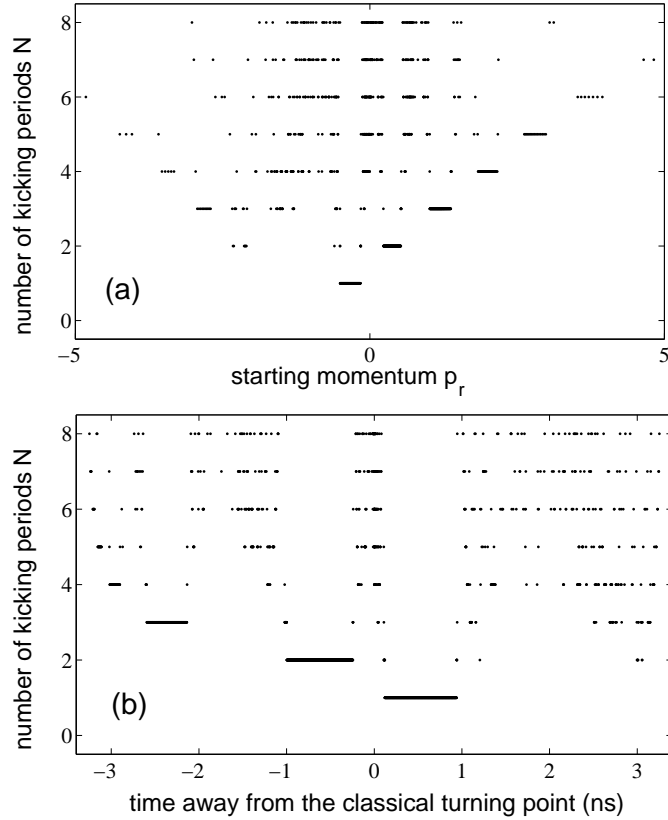


Figure 4.8: The vertical axis represents the number of iterates, and the horizontal one represents the initial value of the momentum along an energy shell (a), and time away from the classical turning point (b). ($\Delta p = 0.4$, $\tilde{\tau}_k = 500$ps, $\tilde{T} = 3$ns)

with a few very short segments. This corresponds to energy shell intervals that overlap the $E_{-2}$ lobe.

As we have already seen, the ionization fraction after one kicking period exhibits step-function-like behavior as a function of $\Delta p$. Similarly, we can measure the ionization fraction as a function of $\Delta p$ after two kicking periods. At $N = 2$ in Fig. (4.8b) there exists one long segment about the same length as the single segment at $N = 1$ and a few very short ones. Hence the proposed experiment would yield the same step-function like behavior of the ionization fraction as a function of the kick strength after two kicking periods. For larger number of kicking periods, the number of escape segments increases greatly, which complicates this simple analysis and would prevent us from observing a clear step-function-like behavior.

## 4.4 Experimental observation of Lobe Length

In this experiment we observe the influence of increasing the kick strength on the splitting in energy between the stable and unstable manifolds, and the influence of the kicking period on the width of the lobes. The experiment is designed as follows. We start by exciting potassium Rydberg atoms into $n = 306$, $\ell = 2$ state. This creates an ensemble of quasi-one-dimensional highly excited electronic states which can be effectively modeled by a uniform classical one-dimensional electron distribution corresponding to $n = 306$ energy shell. Next, we apply one kicking period to this energy shell after which we measure the fraction ($f$) of the electrons that have ionized. In order to observe interesting trends in the ionization fraction behavior, we repeat this experiment for different values of kicking
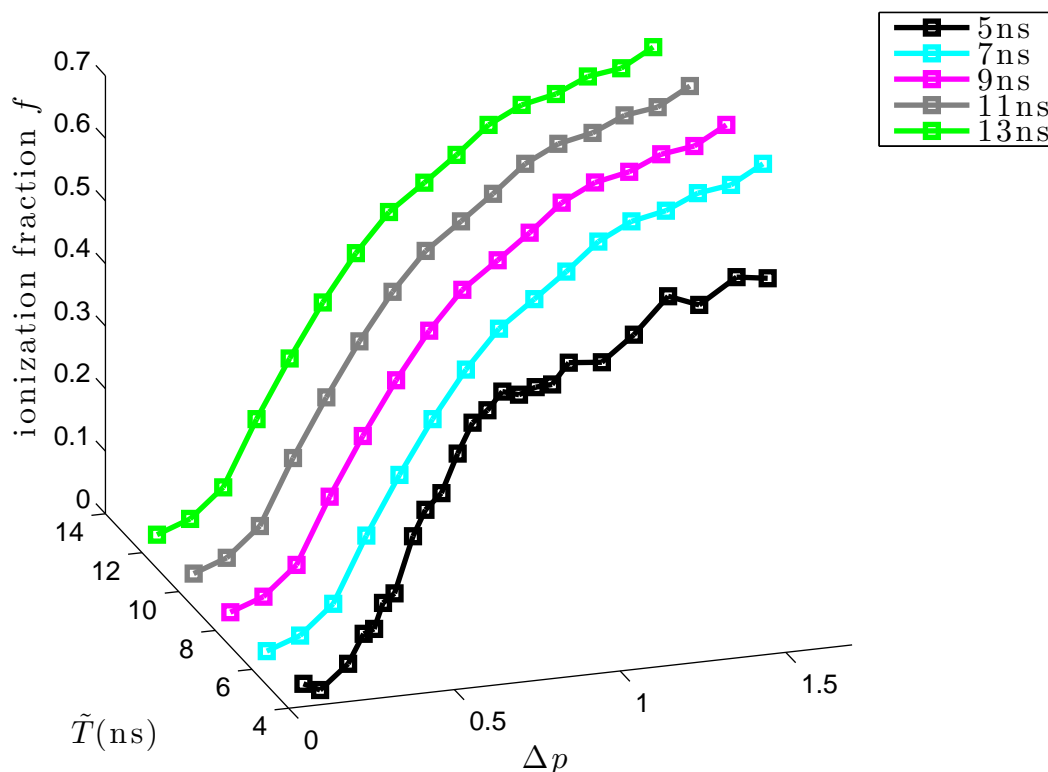
Figure 4.9: Experimental results for ionization fraction as a function of $\Delta p$ and $\tilde{T}$. $n = 306$, and $\tilde{\tau}_k$ are kept constant.

period and kicking strength.

Figure (4.9) shows the experimental results for $\tilde{T}$ ranging from 5ns to 13ns. In order to better see the trends in the experimental results, we show a series of figures in Fig. (4.10) for each value of $\tilde{T}$ comparing the classical 1D predictions with the experimental results and with the full 3D calculations. 3D calculations were done by Brendan Wyker at Rice University in Houston and they include full 3D feature of the atom as well as the direct output from the oscilloscope measuring the shape of the imparted kicks. The ionization cutoff in 3D results is taken to be $n = 1000$ energy shell. These 3D calculations have been shown in the past to have good agreement with experimental results on highly

excited quasi-one-dimensional kicked Rydberg atoms.
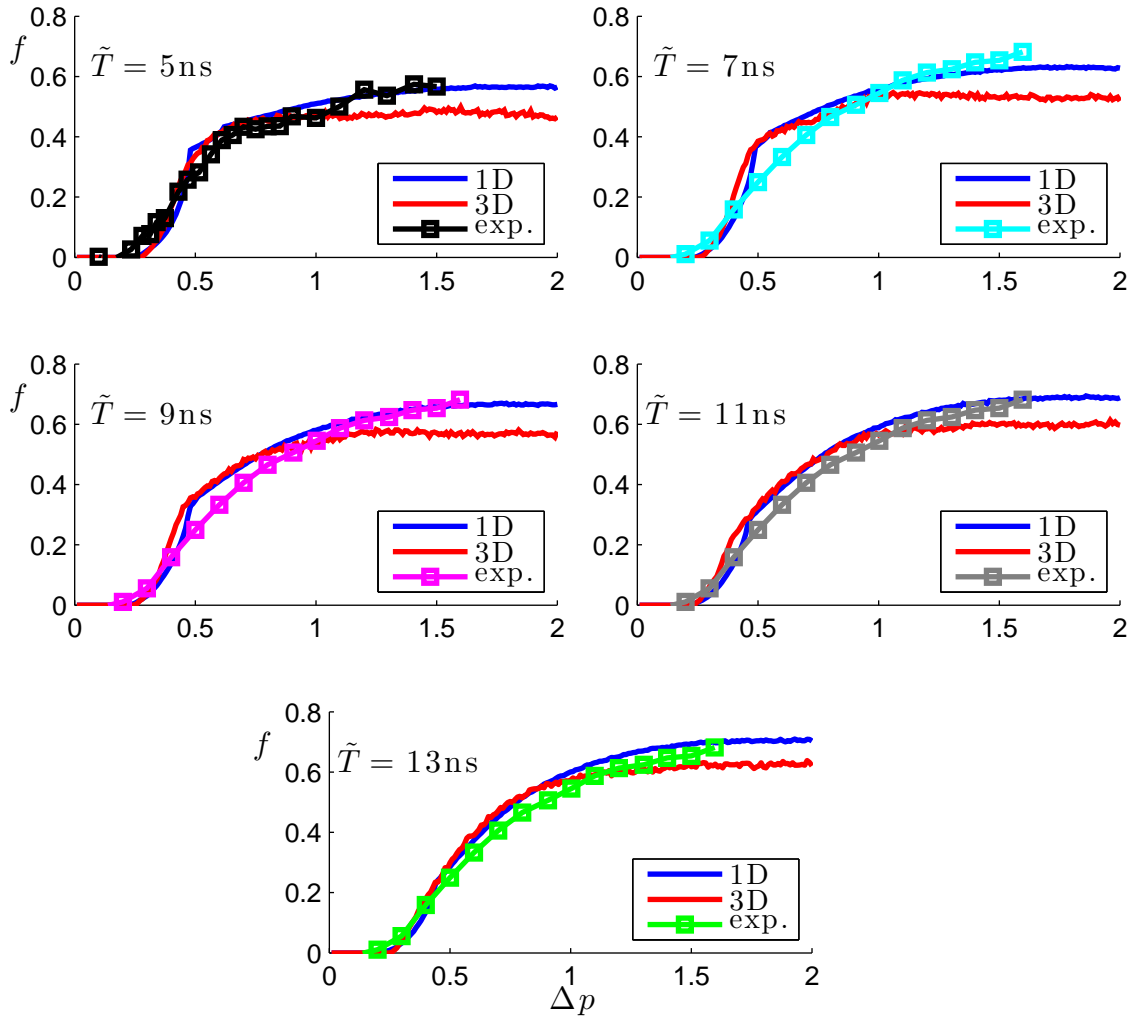


Figure 4.10: A comparison of the ionization fraction results for experiment, 3D, and 1D.

Both the experimental and 3D results show good qualitative agreement with our classical 1D predictions. Similarly to 1D simulations, in the experimental results we are also able to observe an initial slow rise in the ionization fraction, followed by the sharp one which at a critical value of the kicking strength turns again into a more gradual increase

in ionization fraction. We also observed the independence of the initial rise on $T$ and the

increase in the ionization fraction with increasing $T$ at a fixed value of kick strength.

# Chapter 5

# Experiment Involving a Time Dependent Ensemble

In this chapter we present numerical and experimental results on the chaotic ionization of a time dependent ensemble composed of quasi-one-dimensional potassium Rydberg wavepackets. The fundamental difference between the experiment presented in this chapter and the step-function experiment can be understood by observing that in the step-function experiment a particular data set was obtained by incrementally changing the size of the turnstile lobe while keeping the initial ensemble fixed. In contrast to the step-function experiment, in this chapter we keep the turnstile lobe fixed and use the time evolving initial ensemble to "find" the location of the turnstile lobe in phase space. We have already observed (both numerically and experimentally), that only the electrons that occupy the portion of the energy shell that overlaps with the $E_{-1}$ lobe at the time the kicks are turned on get ionized after a single application of the kicking map. Now we proceed

to show how the ionization depends on the relative position of the electronic ensemble in phase space with respect to the position and size of the turnstile (i.e., the $E_{-1}$ lobe). In order to do this, we first create time dependent Rydberg wavepackets, subject them to alternating applied electric field kicks, and measure the survival probability (a fraction of the electrons that did not get ionized with respect to the total number of electrons that we started with). We show that the ionization of the electron depends not only on the initial electron energy, but also on the phase space position of the electron with respect to the turnstile - only the portion of the electron distribution located inside the turnstile ionizes after one period of the applied kicks.

This chapter is organized as follows. In Section 5.1 we present numerical results that show the dependance of the survival probability on the number of applied kicking periods and the position of the time dependent ensemble. Section 5.2 describes the numerical results used to design the experiment as well as the numerical predictions for the experimental behavior of the survival probability as a function of the kicking period and the position of the time dependent ensemble. Finally in Section 5.3 we present the experimental results obtained at Barry Dunning's lab at Rice University in Houston.

## 5.1 Dependance of Ionization on the Position of the Electronic State Relative to the Escape Lobe

In this section, in each set of data we keep the kicking parameters $\tau_k$, $T$ and $\Delta p$ fixed and selectively place the initial ensemble into different areas of phase space. The
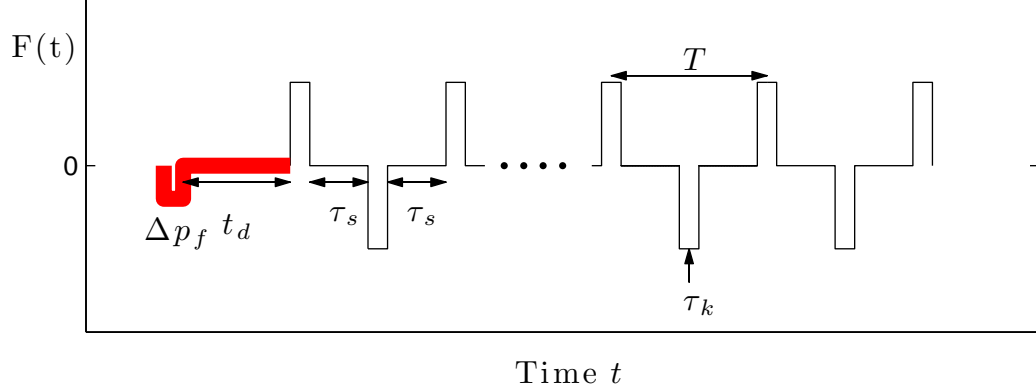
Figure 5.1: Kicking sequence with focusing kick. Red line marks the protocol that creates a time dependent ensemble.

kicking sequence used in this section is shown in Fig. (5.1). We start with an invariant classical distribution of electrons on the energy shell corresponding to $n = 350$ ($E = -1/2$ in scaled atomic units). Next, we apply a small "focusing" kick $n\Delta p_f = 0.08$ towards the origin (i.e. in the negative direction). This causes all the electron trajectories with positive momentum to slow down and the trajectories with negative momentum to speed up. Next we let this distribution evolve for some delay time $t_d$, allowing the electrons that sped up to catch up to the electrons that slowed down, resulting in a partial focusing in phase space. (See Fig. (5.2).) This protocol creates a time dependent ensemble whose orbit tracks the orbit of the starting energy shell. Varying the delay time allows us then to selectively place the focused state mostly just above, inside, or just below the $E_{-1}$ lobe by adjusting $\tilde{t}_d$ to 4.7ns, 6.1ns, and 8.1ns respectively, as shown in Figs. (5.2 b), (5.2 c), and (5.2 d). (For comparison, classical Kepler period of the $n = 350$ energy shell is 6.5ns.)

After the focusing step, we turn on the alternating kicks for N kicking periods, and measure the survival probability (the fraction of unionized electron trajectories) after
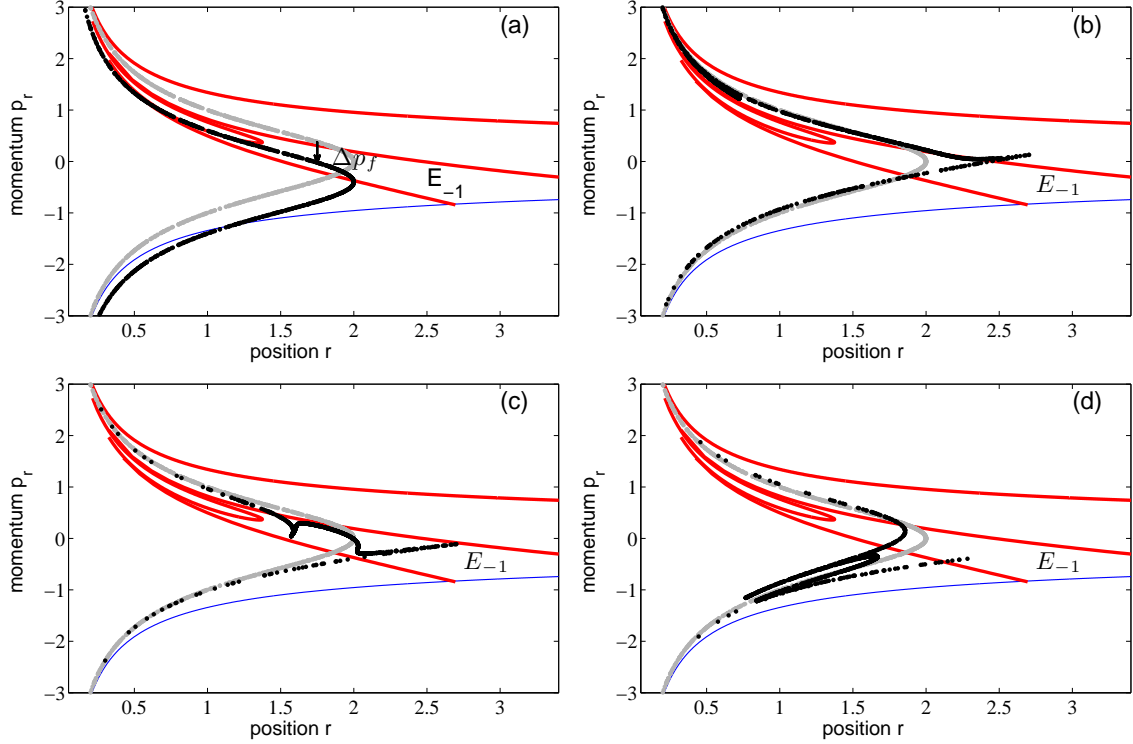
Figure 5.2: Figure (a) shows the initial ensemble on the energy shell $E = -1/2$ in light gray, and the shifted ensemble immediately after the negative kick $\Delta p_f$ in black. (The actual $\Delta p_f$ is 5 times smaller than shown; we have magnified it here to show the shift more clearly.) Figures b, c and d show the new ensemble focused just above ($\tilde{t}_d = 4.7$ns), inside ($\tilde{t}_d = 6.1$ns), and just below ($\tilde{t}_d = 8.1$ns) the $E_{-1}$ lobe.

each kicking period. (See Fig. 5.3.) The $E_{-1}$ lobe manifests itself in the sharp drop of the survival probability for $\tilde{t}_d = 6.1$ns, when most of the points start within the $E_{-1}$ escape lobe. Notice that the survival probability drops by about $83.7\%$ after just one kicking period in this case. For the other two cases, it drops by much less (about $5\%$ and $20\%$). Thus even though we start with the same energy distribution in all three focused states, and apply the same alternating kicks in all three cases, the survival probability shows strong dependence on $t_d$ and hence on the starting position in phase space of the focused distribution.
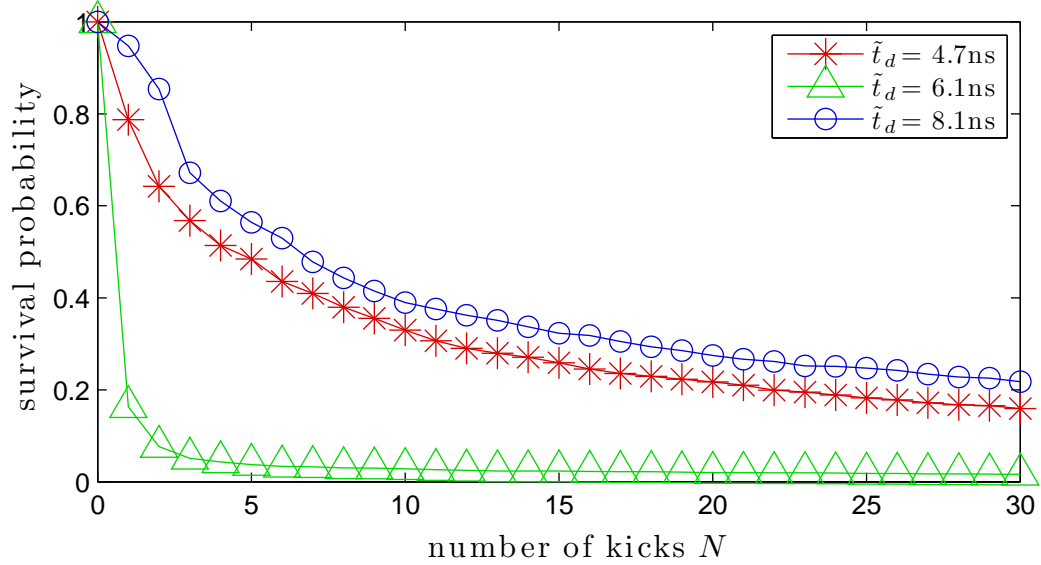
Figure 5.3: Survival probability for focused ensemble located just above ($*$), mostly inside ($\triangle$), or just below ($\bigcirc$) the $E_{-1}$ lobe.

More detailed survival probability data is shown in Fig. (5.4). We create this figure by incrementally increasing $\tilde{t}_d$ from zero to 8.5ns, depicting the survival probability by the shading. Notice that after any given number of kicking periods, the survival probability depends on $\tilde{t}_d$. This is best illustrated with a small number of kicking periods (for example, two kicking periods, as depicted by the gray line in Fig. 5.4). For low values of $\tilde{t}_d$ there are very few electrons inside the $E_{-1}$ lobe when the kicking is turned on, and after two kicking periods the survival probability is still rather high. The survival probability drops quickly around $\tilde{t}_d = 1$ns because the $n = 350$ shell partially intersects the $E_{-1}$ lobe. Right after the focusing kick, most of the top half of the energy shell overlaps the $E_{-1}$ lobe. (See Fig. (5.2a).) For low values of $\tilde{t}_d$, the slow moving electrons do not have enough time to move out of the $E_{-1}$ lobe while some of the fast moving electrons have moved into the $E_{-1}$ lobe. Even though the electrons are not very focused in phase space, there is still
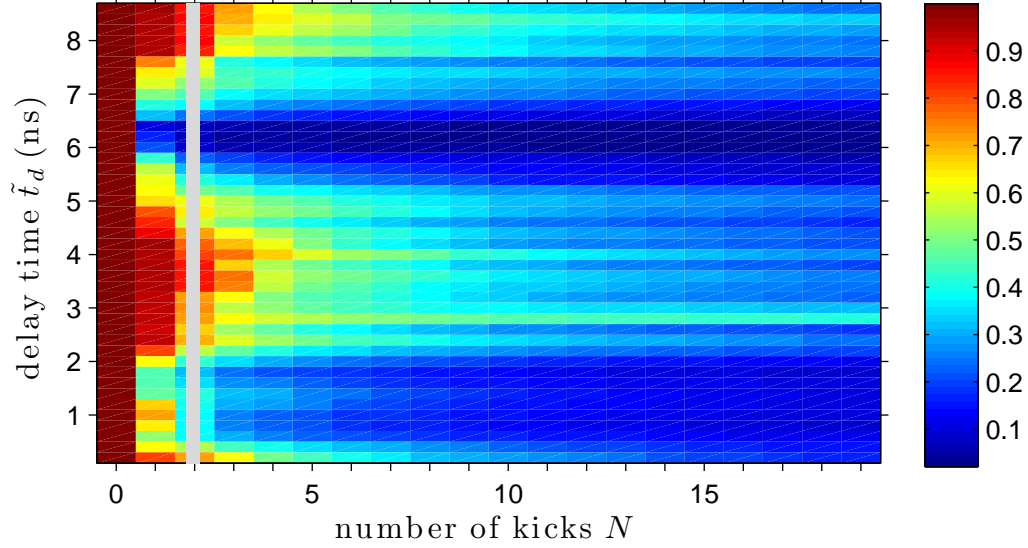
Figure 5.4: Survival probability, as denoted by the color scale, as a function of the focusing time $\tilde{t}_d$ and the number of subsequent kicking periods. This allows us to track the change in survival probability as the focused ensemble moves in and out of the $E_{-1}$ lobe.

a significant overlap between the $E_{-1}$ lobe and the electron trajectories at this time, and the survival probability suppression is the signature of this phenomenon. Around $\tilde{t}_d = 2$ns the slowed trajectories move out of $E_{-1}$, and the survival probability decays slowly as a function of the number of kicking periods. For values of $\tilde{t}_d$ around 6.1ns, the survival probability drops close to zero immediately after the first kicking period, thus signaling that the starting distribution has focused mostly inside the $E_{-1}$ lobe (Fig. (5.2 c)). This ionization enhancement occurs at $t_d$ close to the classical Kepler period for the $n = 350$ energy shell. (The classical Kepler period of the $n = 350$ shell is 6.5ns.) Further increasing $\tilde{t}_d$ causes the focused electron trajectories to pass through the $E_{-1}$ lobe before the kicking is turned on and the survival probability increases again (Fig. (5.2 d)).

## 5.2   Influence of the kick separation on the survival probability

As we have shown in Chapters 2 and 3, changing the kicking period $T$, widens the lobes and it shifts them away from the nucleus. In this section we show numerical predictions for observing the influence of the separation between the kicks on the survival probability of the time dependent electronic ensemble. For the rest of this chapter we focus on applying a single kicking period before measuring the survival probability. The full kicking sequence used to obtain the survival probability in 1D classical simulations is shown in Fig. (5.5). First the ensemble is exposed to the small focusing kick $n\Delta p_f = 0.08$, which creates the spread in electron energies. After the focusing kick, the electrons evolve in the Coulomb potential for $t_d$. After the electrons have been free to evolve for $t_d$, they are exposed to the sequence of positive and negative kicks shown in red in Fig. (5.5). The total impulses imparted by the kicks drawn in red are 0.25, $-0.5$ and 0.25. (The duration of the focusing kick and the negative kick are set to 500ps, while the duration of the two positive kicks is set to 250ps.) At the end of the second positive kick, we measure the survival probability. This process is then repeated for different values of $t_d$ ranging from 0 to 20ns, different values of $\tilde{T}$ ranging from 5 to 15ns and for $n = 306$ and $n = 350$ starting energy shells. We change the value of $T$ by varying the separation between the positive and negative kicks drawn in red in Fig. (5.5).

Figure (5.6) shows a sample trace of the survival probability as a function of the delay time. These are the similar results as the ones corresponding to the gray vertical line
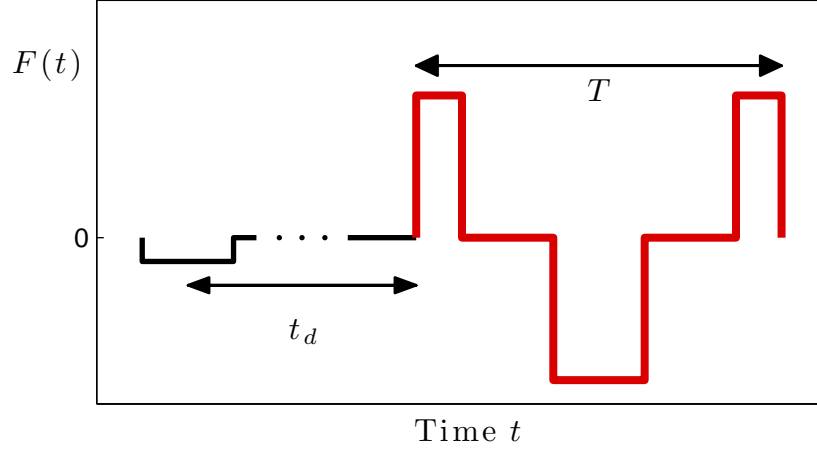
Figure 5.5: Kicking sequence in 1D simulation.

in Fig. (5.4), extended to longer delay time. Figures (5.7) and (5.8) show the behavior of the survival probability for different values of $\tilde{T}$, and different starting energy shells. Observe that the survival probability as a function of the delay time exhibits periodic dips. In order to qualitatively compare the behavior of the survival probability for different values of $\tilde{T}$, we choose to fit the data to the functional form $P(t_d) = P_0 + A\sin(2\pi t_d/T_0 + \phi)$, where $P(t_d)$ represents the survival probability at a given value of the delay time, $P_0$ is the average survival probability, $A$ is the amplitude, $T_0$ is the period of the sinusoidal fit, and $\phi$ is the phase. This fit is represented by a red curve in our figures.

The following features can be observed in both Figs. (5.7) and (5.8): (i) the oscillation period $T_0$ is nearly independent of $T$, and it is approximately equal to the classical Kepler period $T_K$ of the starting energy shell (for $n = 306$, $T_K = 4.35$ns, and for $n = 350$, $T_K = 6.52$ns); (ii) for a given starting energy shell, the average survival probability $P_0$ and the amplitude $A$ do not vary much with $T$; (iii) the phase shift $\phi$
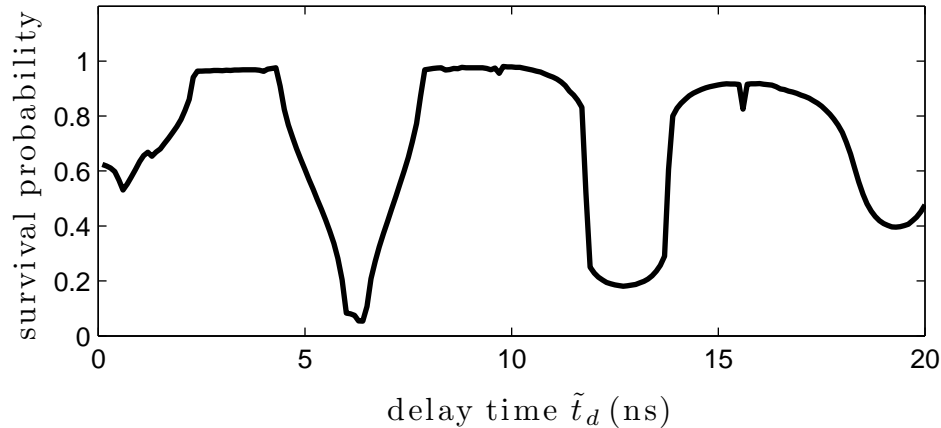
Figure 5.6: Survival probability as a function of delay time for $n = 350$ and $\tilde{T} = 5$ns.

increases with increasing $T$. The increase in phase shift can be observed by following the movement of the peaks in the fitted sinusoid to shorter delay times.

These same features can be observed in the 3D simulations performed at Rice University by Brendan Wyker. (See Fig.(5.9).) 3D simulations take into account the full 3D nature of the electron's orbit and they also include the real experimental shape of the electric field pulses.

Table (5.1) summarizes the values of the fit parameters for results shown in Figs. (5.7), (5.8) and (5.9). We now proceed to explain how the homoclinic tangle geometry offers a qualitative and quantitative explanation of the trends observed in the data. In our explanations we will frequently refer to Table (5.1) when we are talking about the observed trends in the data.

We now proceed to explain how the data shown in Figs. (5.7),(5.8), and (5.9), as well as in the Table (5.1) reveals the presence of the homoclinic tangle, and how the homoclinic tangle geometry offers a qualitative and quantitative explanation of the trends
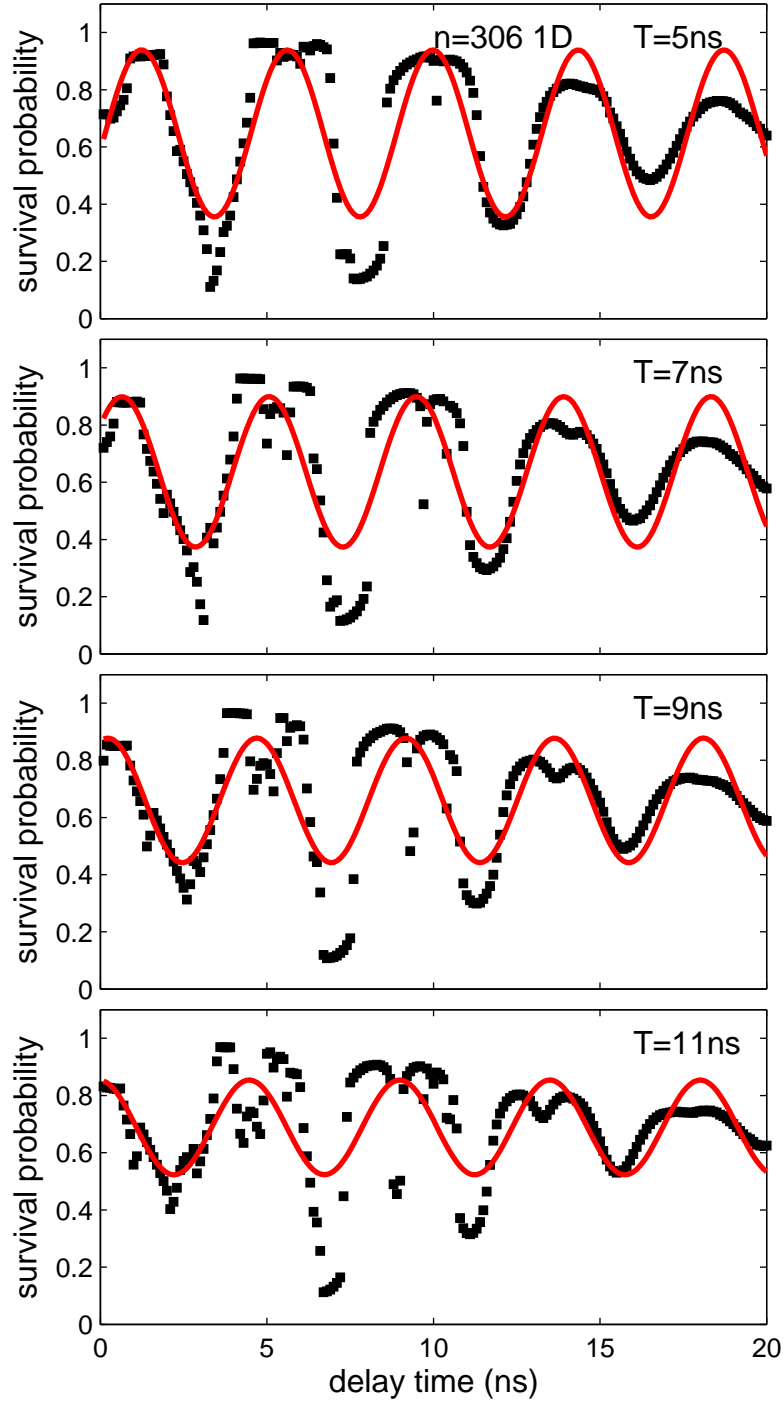
Figure 5.7: Survival probability as a function of delay time for different values of $\tilde{T}$ ($n = 306$). The black squares represent the numerical data and the red line shows the fit to the functional form $P(t_d) = P_0 + A\sin(2\pi t_d/T_0 + \phi)$. The fitting parameters are summarized in Table 5.1.
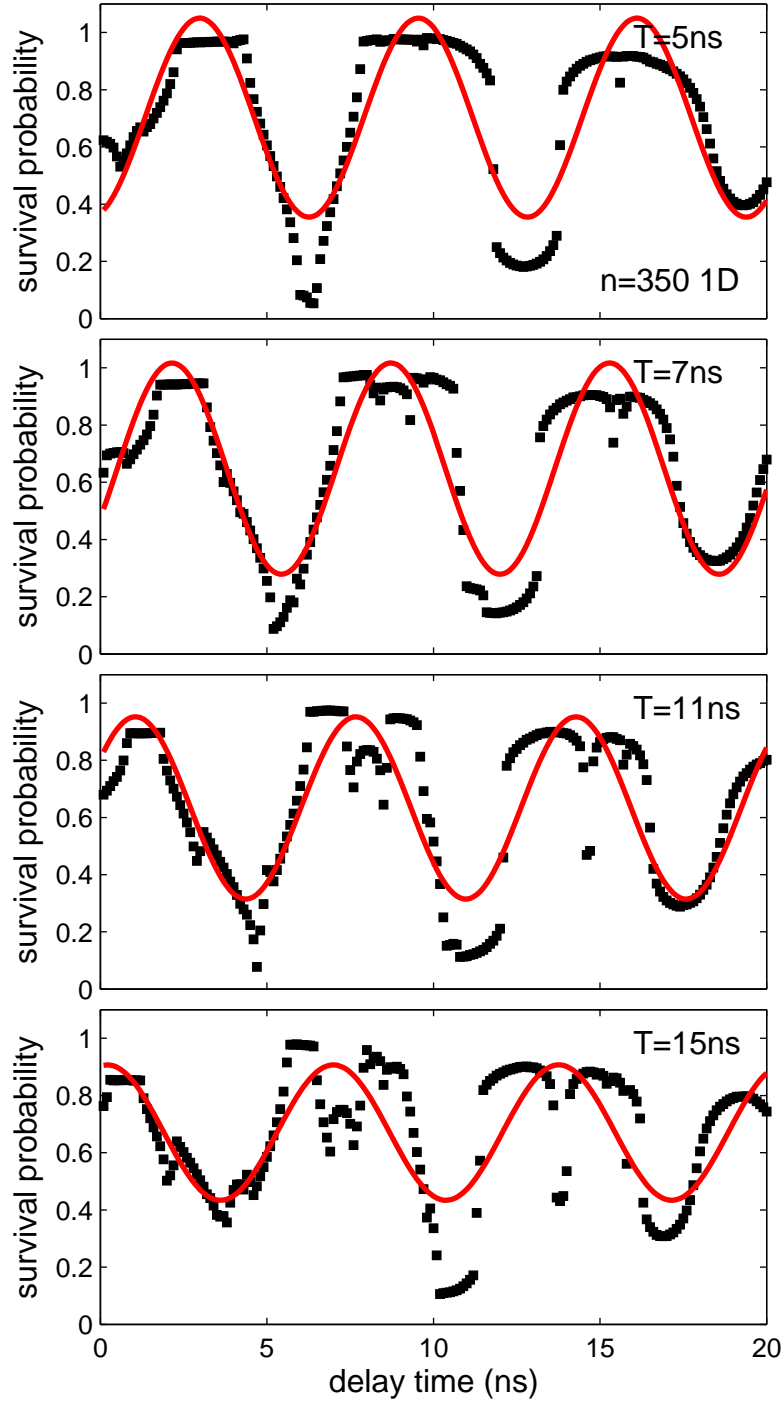
Figure 5.8: Survival probability as a function of delay time for different values of $\tilde{T}$ ($n =$ 350). The black squares represent the numerical data and the red line shows the fit to the functional form $P(t_d) = P_0 + A\sin(2\pi t_d/T_0 + \phi)$. The fitting parameters are summarized in Table 5.1.
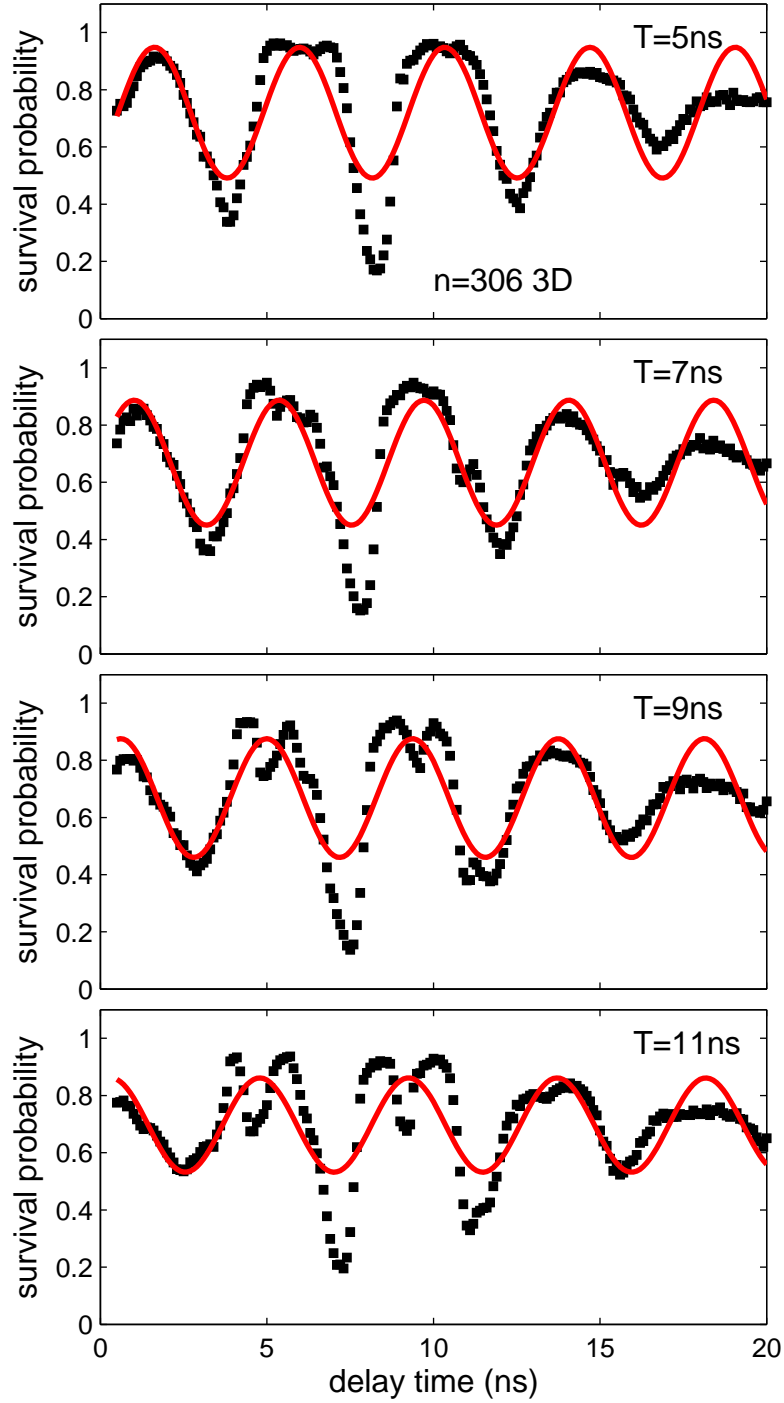
Figure 5.9: Survival probability as a function of delay time for different values of $\tilde{T}$ ($n =$ 306), 3D simulations performed by Brendan Wyker at Rice University. The black squares represent the numerical data and the red line shows the fit to the functional form $P(t_d) = P_0 + A\sin(2\pi t_d/T_0 + \phi)$. The fitting parameters are summarized in Table 5.1.

| $n$ | $T$(ns) | $P_0$ | | | $A$ | | $T_0$(ns) | | $\phi$ | |
|-----|---------|------|------|------|------|------|------|------|------|------|
| | | 1D | 1D' | 3D | 1D | 3D | 1D | 3D | 1D | 3D |
| 306 | 5 | 0.647 | 0.633 | 0.720 | 0.292 | 0.229 | 4.369 | 4.357 | -0.213 | -0.344 |
| | 7 | 0.636 | 0.630 | 0.668 | 0.263 | 0.219 | 4.419 | 4.348 | 0.647 | 0.532 |
| | 9 | 0.659 | 0.663 | 0.668 | 0.218 | 0.208 | 4.459 | 4.378 | 1.249 | 1.119 |
| | 11 | 0.688 | 0.693 | 0.697 | 0.166 | 0.165 | 4.514 | 4.466 | 1.629 | 1.541 |
| 350 | 5 | 0.702 | 0.692 | 0.760 | 0.348 | 0.287 | 6.559 | 6.742 | -1.287 | -1.325 |
| | 7 | 0.648 | 0.623 | 0.703 | 0.369 | 0.304 | 6.566 | 6.749 | -0.489 | -0.612 |
| | 11 | 0.633 | 0.624 | 0.664 | 0.319 | 0.265 | 6.607 | 6.684 | 0.564 | 0.405 |
| | 15 | 0.670 | 0.669 | 0.678 | 0.237 | 0.215 | 6.771 | 6.785 | 1.367 | 1.184 |

Table 5.1: The values are obtained by fitting the 1D and 3D simulation results to the functional form $P(t_d) = P_0 + A\sin(t_d 2\pi/T_0 + \phi)$, where $P_0$ is the average value of the survival probability, $A$ is the amplitude, $T_0$ is the fitted period, and $\phi$ is the phase. The errors in $P_0$ are on the order of 1%, while in $A$ and $T_0$ they are on the order of 5% and less than 1%, respectively.

observed in the data.

After the focusing kick is applied, the electronic state is no longer stationary, but has an energy spread $\Delta E = 0.053$ centered at $E = -0.5$. The energy distribution after the focusing kick is depicted by a histogram $\rho(E)$ shown in Fig. (5.10). (Unless otherwise noted, the remainder of the section focuses on $n = 350$ case.) The corresponding classical distribution is no longer uniform along the $E = -0.5$ shell, but forms a partially localized, or focused, ensemble that moves along the $E = -0.5$ shell. As we have already seen in Fig.(5.2), the oscillations in survival probability observed in Figs. (5.7), (5.8), and (5.9) can be understood as reflecting the motion of the ensemble passing in and out of the $E_{-1}$ lobe. The survival probability is higher when the bulk of the ensemble is outside $E_{-1}$ lobe and smaller when it is inside. Since the ensemble trajectories lie close to the original energy shell, the survival probability oscillation period $T_0$ is approximately the Kepler period $T_K$, explaining our prior observations.
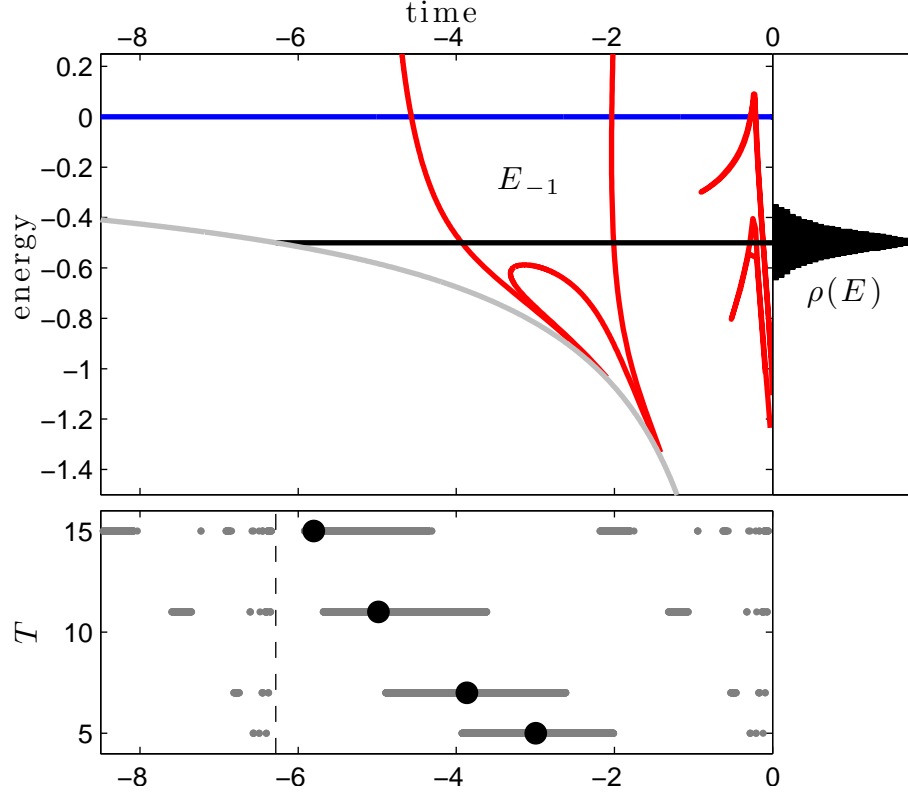
Figure 5.10: The top panel shows the $E_{-1}$ lobe in energy-time coordinates. $\rho(E)$ illustrates the distribution of energies in the focused ensemble. The bottom panel shows the intersections of the $E_{-1}$ lobe with the $E = -0.5$ line for different kicking times $T$. The dashed line is positioned at the negative Kepler period and the rightmost segments are repeated on the left taking advantage of the periodic boundary conditions. The Kepler period of the $E = -0.5$ shell is equal to $2\pi$. The large dots are the average positions of the intersection points.

We next consider the average survival probability $P_0$. $1 - P_0$ can now be interpreted as the fraction of time a trajectory spends inside the $E_{-1}$ lobe, averaged over the focused ensemble. To visualize this, it is easiest to work in the energy-time canonical coordinates. Recall that $E$ is the electron energy $p_r^2/2 - 1/r$ and $t$ is time needed for the electron to reach the nucleus. Figure (5.10) shows a portion of the phase space in these coordinates. The lower left boundary of the phase space consists of the curve $t = -T_K(E)$,

corresponding to the Kepler period of each energy shell. (Remember that as the energy becomes more negative, the electron becomes more closely bound to the nucleus and its Kepler period decreases.) It is physically identified with the right vertical boundary line $t = 0$, with both curves representing electron bouncing off the nucleus. Time evolution in these coordinates consists of uniform motion rightward along horizontal lines; when a trajectory reaches $t = 0$, it jumps back to $t = -T_K$. Figure (5.10) also includes the $E_{-1}$ lobe which is bounded from above by a blue unstable manifold and from below by the red stable manifold. The horns of the lobe continue to extend downward, intersecting the left boundary and reemerging from the right boundary. The lobe $E_{-1}$ intersects the energy shell $E = -0.5$ in one large interval ($-4 \lesssim t \lesssim -2$) and a few short intervals close to the nucleus. These short intervals are the result of the intersection between the horns and the energy shell. (See Fig.(5.10), $T = 5$ns, for intersection segments.) In energy-time coordinates, the fraction of time a trajectory of given energy $E$ spends inside the $E_{-1}$ lobe equals the total length of the intersection between $E_{-1}$ and the line of constant $E$, divided by $T_K$. Since $\Delta E$ for the focused ensemble is small, we need only consider $E = -0.5$, with $T_K = 2\pi$. Thus, $1 - P_0 \approx L/2\pi$, where $L = 0.308$ is the total length of the intersection segments in Fig.(5.10) for $T = 5$ns. Thereby, $P_0 = 0.692$, as recorded in Table 5.1 column 1D'. This result is in excellent agreement with the 1D and 3D values of 0.702 and 0.760.

The story becomes more interesting as $T$ is varied. We have shown in previous chapters that as $T$ increases (with kick strength and duration fixed), the lobe $E_{-1}$ shifts away from the nucleus. The bottom panel in Fig.(5.10) confirms this, as the large interval shifts left with increasing $T$. However, another critical effect is the relative increase in

the smaller intervals on the right, representing intersections with the horns wrapping around. Physically, the large interval contains trajectories striking the nucleus once during ionization, whereas the smaller intervals contain trajectories striking the nucleus multiple times during ionization. This makes sense - as we wait longer between the ionization pulses, there is more time for trajectories to strike the nucleus, and the relative importance of these ionization pathways increases. By $T = 15$ns, 24% of the ionizing trajectories have multiple impacts with the nucleus. The corresponding results for $P_0$ are recorded in Table 5.1 column 1D', showing good agreement with the 1D data. If ionization via multiple impacts were not included, this agreement would be notably worse, especially for $T = 15$ns.

The leftward shift of the intervals in the bottom panel of Fig.(5.10) with increasing $T$ also explains the phase shift in Figs. (5.7), (5.8), and (5.9). The large dots in the bottom panel of Fig.(5.10) are the average positions of the escaping points (where the average is computed by only including the long segment and the repeated segments on the left of the phase space boundary). We again note the importance of the multiple impact trajectories in shifting the average dot leftward in the bottom panel of Fig.(5.10) (especially for $T = 15$ns.)

## 5.3   Experimental results showing the signature of the homoclinic tangle

The experimental setup used in this experiment has already been described in Chapter 4. The kicking sequence is shown in Fig. (5.11 a). (For comparison to the
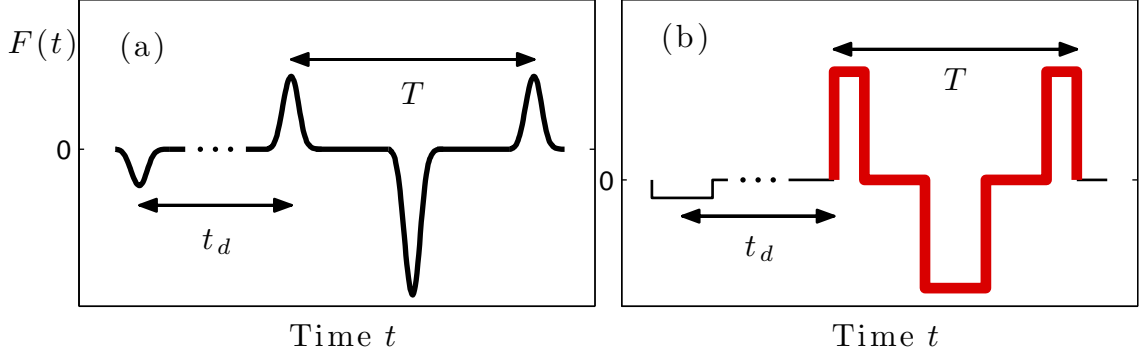
Figure 5.11: Sketch of the experimental kicking sequence.

previous two sections in this chapter, in Fig. (5.11 b) we also include the sketch of the

kicking sequence used in 1D simulations.) The duration of the kicks in the experiment

at full width half maximum is set to 600ps. The focusing impulse is set to $n\Delta p = 0.08$,

and the subsequent kicks impart the impulse equal to 0.25, $-0.5$, and 0.25. Figure (5.12)

shows traces for both $n \approx 306$ (left column) and $n \approx 350$ (right column). Delay time $\tilde{t}_d$ is

increased from 0ns to 20ns, and the peak-to-peak duration $\tilde{T}$ of the ionization sequence is

adjusted between 5ns and 15ns. (The kick durations are all fixed at 600ps.)

The experimental results are shown in Fig. (5.12). They follow the same features

we have observed in the previous section in 1D and 3D simulations. (The gray line in

Fig. (5.12) is there to help guide the eye in observing the phase shift with increasing $T$.)

The fitted parameters $P_0$, $A$, and $T_0$ for the experimental data are summarized in Ta-

ble 5.2, and the fitted phase data is shown in Fig. (5.13). Notice that the fitted values for

$P_0$, $T_0$ and $\phi$ for the the experimental results are in excellent agreement with the predicted

1D simulations. As we have seen in the previous section, these are the parameters that

reflect the underlying phase space geometry. A simple theoretical analysis for the change
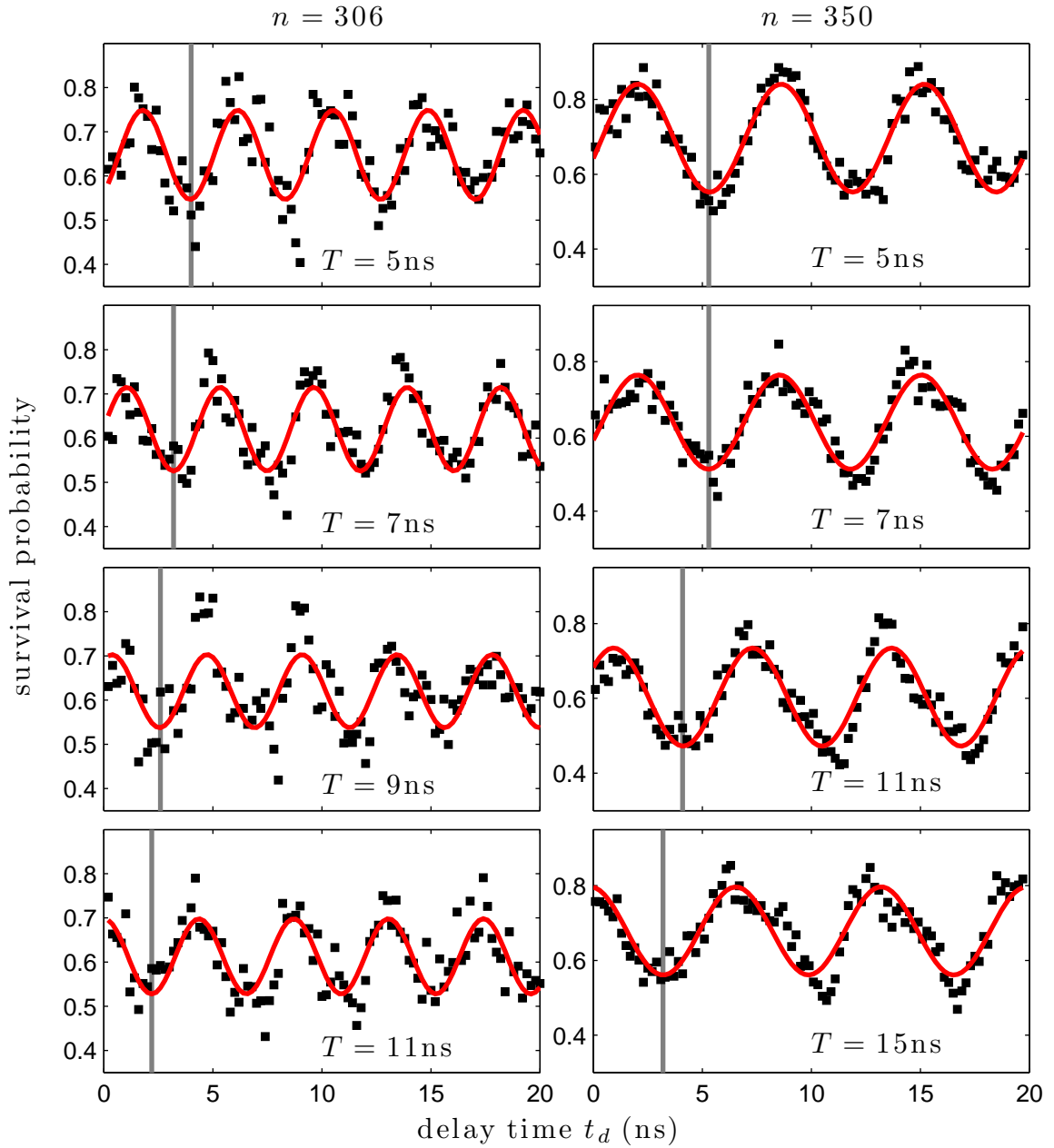
Figure 5.12: Black squares denote the experimental results, and the red line is the sinusoidal fit described in Sec. 5.2

| $n$ | $T$(ns) | $P_0$ | | | | $A$ | | | $T_0$(ns) | | |
|---|---|---|---|---|---|---|---|---|---|---|---|
| | | exp | 1D | 3D | 1D' | exp | 1D | 3D | exp | 1D | 3D |
| 306 | 5 | 0.648 | 0.647 | 0.720 | 0.633 | 0.10 | 0.29 | 0.23 | 4.363 | 4.369 | 4.357 |
| | 7 | 0.620 | 0.636 | 0.668 | 0.630 | 0.09 | 0.26 | 0.22 | 4.286 | 4.419 | 4.348 |
| | 9 | 0.620 | 0.659 | 0.668 | 0.663 | 0.08 | 0.22 | 0.21 | 4.357 | 4.459 | 4.378 |
| | 11 | 0.613 | 0.688 | 0.697 | 0.693 | 0.09 | 0.17 | 0.17 | 4.348 | 4.514 | 4.466 |
| 350 | 5 | 0.697 | 0.702 | 0.760 | 0.692 | 0.14 | 0.35 | 0.29 | 6.572 | 6.559 | 6.742 |
| | 7 | 0.638 | 0.648 | 0.703 | 0.623 | 0.13 | 0.37 | 0.30 | 6.504 | 6.566 | 6.749 |
| | 11 | 0.603 | 0.633 | 0.664 | 0.624 | 0.13 | 0.32 | 0.27 | 6.372 | 6.607 | 6.684 |
| | 15 | 0.679 | 0.670 | 0.678 | 0.669 | 0.12 | 0.24 | 0.22 | 6.663 | 6.771 | 6.785 |

Table 5.2: The values are obtained by fitting the experimental results to the functional form $P(t_d) = P_0 + A\sin(t_d 2\pi/T_0 + \phi)$, where $P_0$ is the average value of the survival probability, $A$ is the amplitude, $T_0$ is the fitted period, and $\phi$ is the phase. The errors in $P_0$ are on the order of 1%, while in $A$ and $T_0$ they are on the order of 5% and less than 1%, respectively.

in lobe geometry when $T$ is small predicts the slope $\Delta T/\Delta\phi = 4T_K/2\pi$, which is shown

by the right triangles in Fig. (5.13) and nicely matches the small $T$ data. The ampli-

tude $A$, however, involves a stronger convolution with the details of the electronic state

itself. Perhaps not surprisingly, then, the experimental oscillation amplitude is somewhat
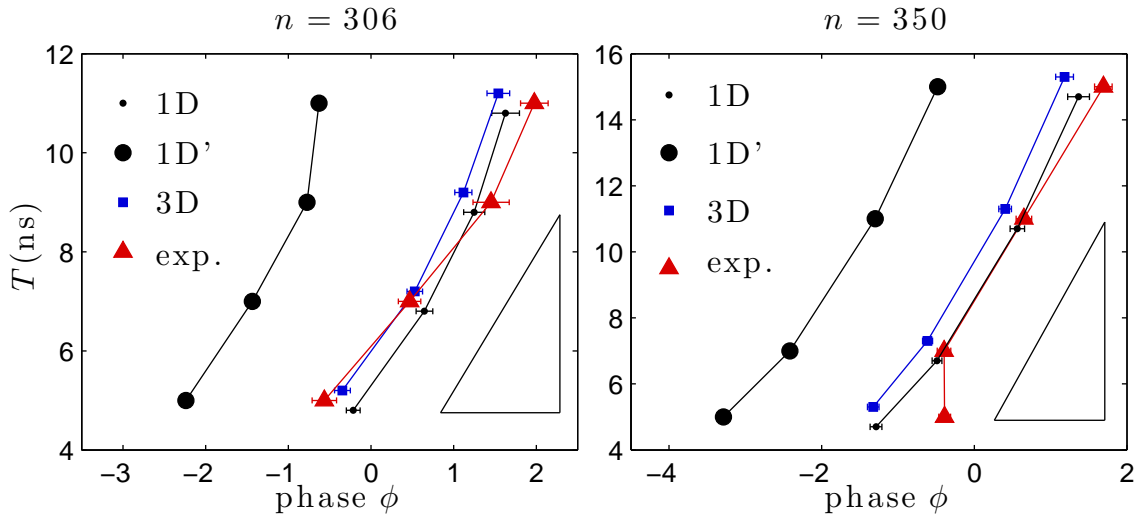


Figure 5.13: Phase shift data. Small shifts in $T$ are applied to 1D and 3D data to visually separate data markers.

diminished (by about a factor of two) from the 1D model.

The experimental data and its theoretical interpretation thus identifies the homoclinic tangle and its corresponding $E_{-1}$ turnstile lobe as the critical mechanism for promoting the bound electronic states to ionization. The turnstile geometry provides a framework for explaining the experimental results, for example, revealing the phase space origins of data trends and illustrating the growing importance of multiple impact ionization as the forcing duration $T$ increases. More broadly, these results place the turnstile mechanism in chaotic ionization within the same framework as other physical manifestations of chaotic dynamics, and demonstrate that kicked atomic systems provide a convenient laboratory model for such mechanisms.

# Chapter 6

# Hydrogen in Crossed Fields

Ionization of hydrogen in crossed fields has been of scientific interest for many years [12, 20, 23, 44, 50]. Not only is this a beautiful example of a chaotic system, but it is also widely considered a stepping stone to understanding the escape in the classic gravitational three body problem, because the electron's classical motion resembles the motion of the Moon in the Sun-Earth-Moon three body system [18]. One of the major challenges in studying chaotic ionization of hydrogen in crossed fields is to define a Poincaré surface of section (SOS) that captures all the allowed electron trajectories, but at the same time does not suffer from tangencies. In this chapter we will present a prescription for defining a Poincaré return map that defines a local SOS which captures the turnstile responsible for the ionization process.

## 6.1  Electron's equations of motion

Consider an electron moving in a magnetic field. Electron's trajectory is a circle (except in a very special case when the velocity of the electron is parallel to the magnetic field). Adding an electric field oriented perpendicular to the magnetic field changes the shape of a trajectory from a circle to a helix. Hence the motion is a combination of circular trajectory and the $E \times B$ drift. Further inclusion of Coulomb potential adds a wealth of complexity to the electron's motion. In this chapter we consider an electron moving in a potential created by the nucleus and external crossed electric and magnetic fields. The electric field is oriented in the $\hat{x}$ and the magnetic field is oriented in the $\hat{z}$ direction. Electron's motion in physical coordinates is then described by the following Hamiltonian in atomic units ($e = m_e = \hbar = 1$)

$$H = \frac{p^2}{2} + \frac{B}{2}L_z + \frac{B^2}{8}\left(x^2 + y^2\right) - \frac{1}{r} + Fx, \tag{6.1}$$

where $F$ represents the electric field, and $B$ is the magnetic field. Since the magnetic field is oriented in the $\hat{z}$ direction, it couples with the $z$ component of the electron's angular momentum which is represented by the $BL_z/2$ term in the Hamiltonian. We restrict ourselves only to electron motion in the $x - y$ plane, so $p^2 = p_x^2 + p_y^2$, and $r = \sqrt{x^2 + y^2}$. Finally, since the Hamiltonian is independent of time, the total energy is conserved in this system.

In order to avoid the Coulomb singularity at the origin, we again employ the use of the parabolic coordinates. The transformation to parabolic coordinates is more complex than what we have seen in Chapter 2, because the phase space dimension has increased

from two to four. The two position variables in the parabolic coordinates $u$ and $v$ can be found using the following equations:

$$u = \pm\sqrt{r + x} \qquad \text{and} \qquad v = \pm\sqrt{r - x}, \tag{6.2}$$

while the two conjugate momenta $p_u$ and $p_v$ can be found using:

$$p_u = vp_y + up_x \qquad \text{and} \qquad p_v = up_y - vp_x. \tag{6.3}$$

The inverse transformation is defined by

$$x = \frac{1}{2}\left(u^2 - v^2\right) \qquad \text{and} \qquad y = uv, \tag{6.4}$$

with

$$r = \sqrt{x^2 + y^2} = \frac{1}{2}\left(u^2 + v^2\right), \tag{6.5}$$

for the position coordinates, and by

$$p_x = \frac{up_u - vp_v}{u^2 + v^2} \qquad \text{and} \qquad p_y = \frac{vp_u + up_v}{u^2 + v^2}, \tag{6.6}$$

for the momenta. We also define a transformed Hamiltonian $h$, as

$$h = 2r(H - E), \tag{6.7}$$

where $E$ represents the energy so $h = 0$. The transformed Hamiltonian $h$ is then equal to

$$h = \frac{1}{2}\left(p_u^2 + p_v^2\right) + \frac{B}{4}\left(u^2 + v^2\right)\left(up_v - vp_u\right) + \frac{B^2}{32}\left(u^2 + v^2\right)^3 - 2 + \frac{F}{2}\left(u^4 - v^4\right) - \left(u^2 + v^2\right)E. \tag{6.8}$$

Transforming into parabolic coordinates transforms the time coordinate as well. The relationship between the physical ($t$) and transformed ($s$) time given by

$$\frac{dt}{ds} = \left(u^2 + v^2\right). \tag{6.9}$$

The equations of motion in the parabolic coordinates are:

$$\dot{u} = p_u - \frac{B}{4} v \left( u^2 + v^2 \right)$$

$$\dot{v} = p_v + \frac{B}{4} u \left( u^2 + v^2 \right)$$

$$\dot{p}_u = \frac{B}{4} \left[ 2uvp_u - p_v \left( 3u^2 + v^2 \right) \right] - \frac{3B^2}{16} u \left( u^2 + v^2 \right)^2 - 2Fu^3 + 2uE$$

$$\dot{p}_v = \frac{B}{4} \left[ -2uvp_v - p_u \left( u^2 + 3v^2 \right) \right] - \frac{3B^2}{16} v \left( u^2 + v^2 \right)^2 + 2Fv^3 + 2vE, \qquad (6.10)$$

where overdot represents the differentiation with respect to $s$. Unlike in Chapter 2 where we were able to solve the equations of motion by hand, these equations require heavy use of numerical machinery.

The Hamiltonian in the parabolic coordinates can be rewritten as

$$h = \frac{1}{2} \left| \vec{p} - \vec{A} \right|^2 - E \left( u^2 + v^2 \right) - 2 + \frac{1}{2} F \left( u^4 - v^4 \right), \qquad (6.11)$$

where

$$\vec{p} = [p_u, p_v]$$

and

$$\vec{A} = \frac{1}{4} B \left( u^2 + v^2 \right) [v, -u].$$

As a final note in this section, we observe that there are only two independent parameters in this system. We decide to use only the strength of the magnetic field and the electron energy and we scale out the strength of the electric field. This is equivalent to scaling the distances and lengths by $F^{1/2}$, momenta by $F^{-1/4}$, time by $F^{3/4}$, magnetic field by $F^{-3/4}$ and the energy by $F^{-1/2}$. In the remainder of this chapter we use these scaled coordinates (i.e., $F = 1$).
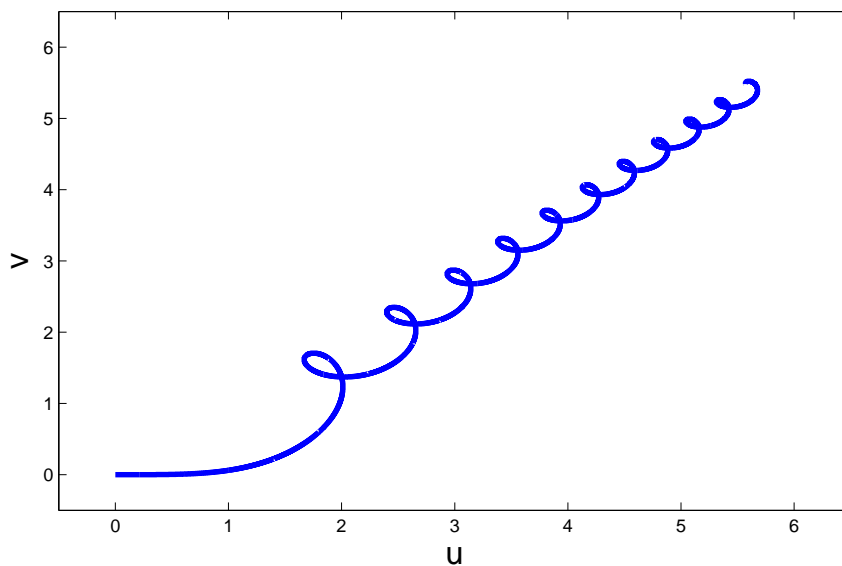
Figure 6.1: Representative trajectory launched away from the nucleus along the line $v = 0$. ($B = 1.5$, $E = -0.2$, where $B$ and $E$ are the magnetic field strength and the energy in scaled coordinates)

## 6.2   Definition of the Poincaré return map

Our approach for defining the Poincaré return map is based on the technique used in a system where the hydrogen atom is placed in external parallel electric and magnetic fields [34, 35, 38]. In the parallel fields problem, the Poincaré return map is defined by recording the electrons position and momenta at the time when its trajectory crosses the $v = 0$ line. This line corresponds to a unique trajectory that when launched towards the nucleus returns along the same trajectory upon bouncing off the nucleus. In the crossed fields system, there exists no such trajectory because the magnetic field $B$ causes the trajectories to curve. However, we choose a trajectory that is launched away from the nucleus at $u = v = 0$ ($x = y = 0$) in the direction of the Stark saddle (in our system the Stark saddle is located at a positive value of $u$, i.e. $x$ coordinate), along the line
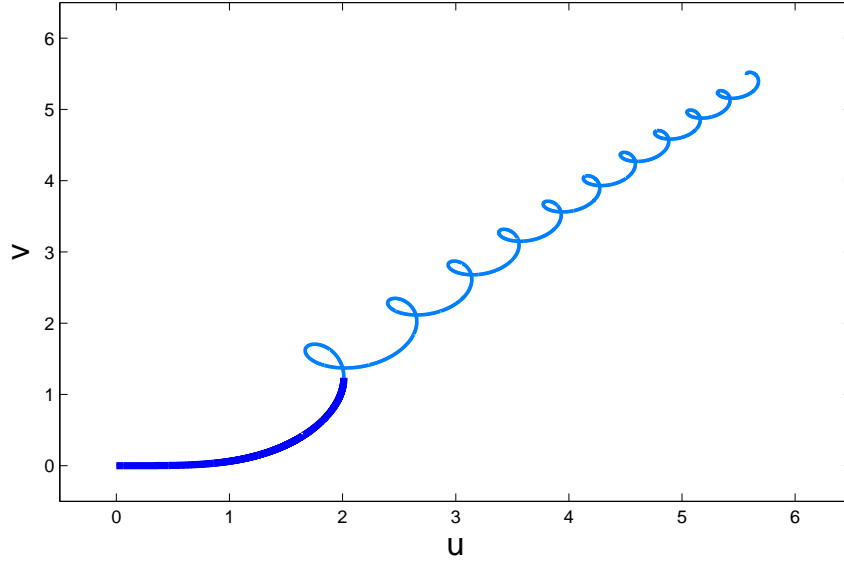
Figure 6.2: A portion of the representative trajectory launched away from the nucleus along the line $v = 0$ chosen to define SOS. ($B = 1.5$, $E = -0.2$, where $B$ and $E$ are the magnetic field strength and the energy in scaled coordinates)

$v = 0$. Locally at the nucleus this trajectory corresponds to the trajectory used to define the Poincaré return map in the parallel fields case. An example of a type of an orbit we are interested in is shown in Fig. (6.1). As we have already mentioned, there exist no trajectories that fall on the straight line in the crossed fields system. Instead, a type of the trajectories we are considering as candidates for defining the Poincaré return map resemble tapered helical shape with the larger radius closer to the nucleus (see Fig. (6.1)). Away from the nucleus, one can clearly observe the $E \times B$ drift.

Trajectories self intersect when projected onto $(u, v)$ space. Nevertheless, we take the portion of this trajectory from the nucleus ($u = v = 0$) up to the point where $\partial v / \partial u = \infty$, i.e., the tangent to the trajectory points in the $v$ direction in $(u, v)$ space. This portion of the trajectory is shown as a thick blue line in Fig. (6.2). Next, we extend this

portion of the trajectory to the remaining quadrants in $(u, v)$ space, by reflecting through the origin and about $u$ and $v$ axes. (See Fig. (6.3).) Reflecting about the origin corresponds to launching a trajectory from the nucleus along the $v = 0$ line in the opposite direction from the Stark saddle. On the other hand, reflecting about the $v = 0$ line is equivalent to time reversal. In Fig. (6.3), we show portions of the trajectories launched away from the nucleus in blue, and their time reversed equivalents in red. The arrows denote the direction of time along the trajectory.

We are now ready to define a local surface of section by recording the electrons' position and momenta at the moment when electron trajectories intersect either the red or the blue line while moving from the region labeled 1 to the region labeled 2. We do not consider crossings from region 2 to region 1 as part of the SOS. Note that this definition of the SOS results with four dimensional phase space. A little later in this section we will present a projection that reduces the SOS dimension from four to two.

As we have already mentioned, the blue line in the first quadrant represents the trajectory launched in the positive direction away from the nucleus, while the red line in the fourth quadrant represents that same trajectory but in the negative time direction. The system exhibits the symmetry about the nucleus which is represented by the oriented lines in second and third quadrants. The reflection about the $u = 0$ line can be understood by remembering that in the presence of the magnetic field a charged particle will experience a force proportional to $\vec{v} \times \vec{B}$, where $\vec{v}$ is the velocity of the charged particle. Hence two identical charged particles launched from the same point in space and with the same speed but with antiparallel velocity vectors are going to curve in opposite direction. This in
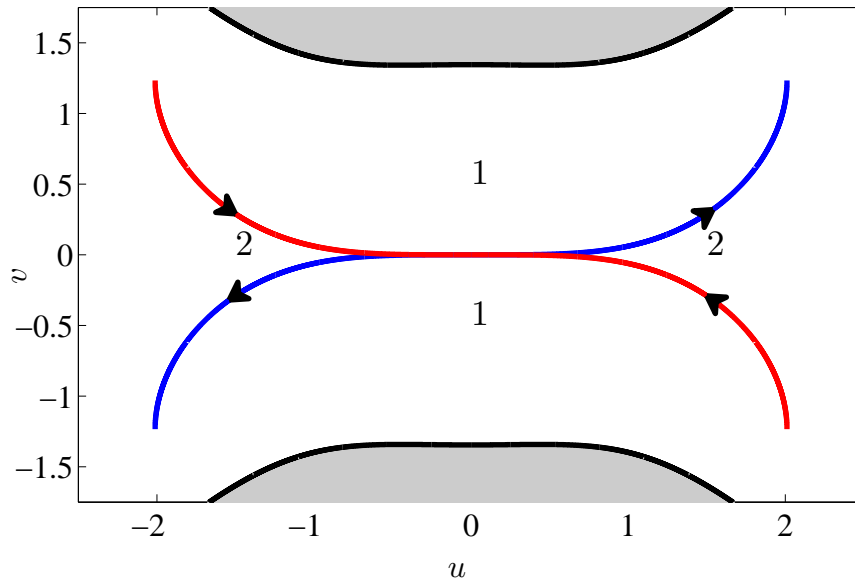
Figure 6.3: Representative Trajectory Defining the Surface of Section ($B = 1.5$, $E = -0.2$, where $B$ and $E$ are the magnetic field strength and the energy in scaled coordinates). The thick black line represents the boundary between the energetically allowed (white) and forbidden (shaded) regions.

turn allows us to identify the two blue lines with each other and two red lines with each other. On the other hand, reflection about the $v = 0$ line is equivalent to time reversal, and we can then identify the red and the blue lines. Thus, if we are careful about the time ordering, we only need to consider the blue line from the first quadrant when defining the surface of section.

This definition of the surface of section is free of tangencies because the line whose crossing defines the surface of section is a portion of a physical trajectory. All physical trajectories are solutions of a system of Hamilton's equations, and due to the uniqueness of the differential equation solutions, all trajectories are unique. Hence, no trajectory self intersects, nor does it intersect any other distinct trajectory in the full four dimensional phase space. When projected onto the position space $(u, v)$, the trajectories are allowed
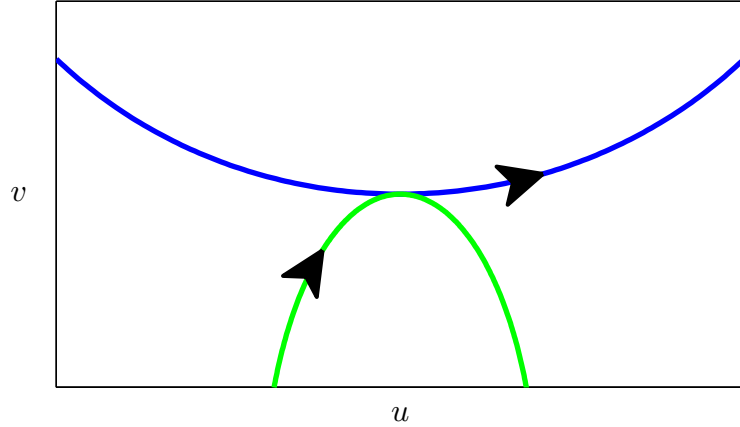
Figure 6.4: A sketch of two mutually exclusive trajectories.

to self intersect as well as intersect other trajectories. However, the scenario shown in Fig.(6.4) is not possible. If both the green and the blue trajectories were allowed solutions to the differential equations describing the electron motion, then both trajectories would have the same value of the tangent at the point of touching. Remember that the tangent to a trajectory in $(u, v)$ space is directly connected to the momenta $p_u$ and $p_v$. Hence the point where the blue and the green trajectories touch would have two different histories and two different futures which contradicts uniqueness of the solutions to the differential equations describing the electron's time evolution. Thus, we are free to conclude that our surface of section definition is free of tangencies.

The electron's behavior resides in the four dimensional phase space described by $(u, v, p_u, p_v)$ set of coordinates. In order to clearly visualize the electron's behavior, we reduce the dimensionality of system to two dimensions described by coordinates $(a, p_a)$, where $a$ represents the Euclidean length along the surface of section as measured from the nucleus. The momentum coordinate $p_a$ is defined by projecting the momentum $(p_u, p_v)$

onto the tangent line to the trajectory used to define the surface of section evaluated at the point where two trajectories intersect in the $uv$ space. We define the blue lines to have $a > 0$, and the red lines to have $a < 0$.
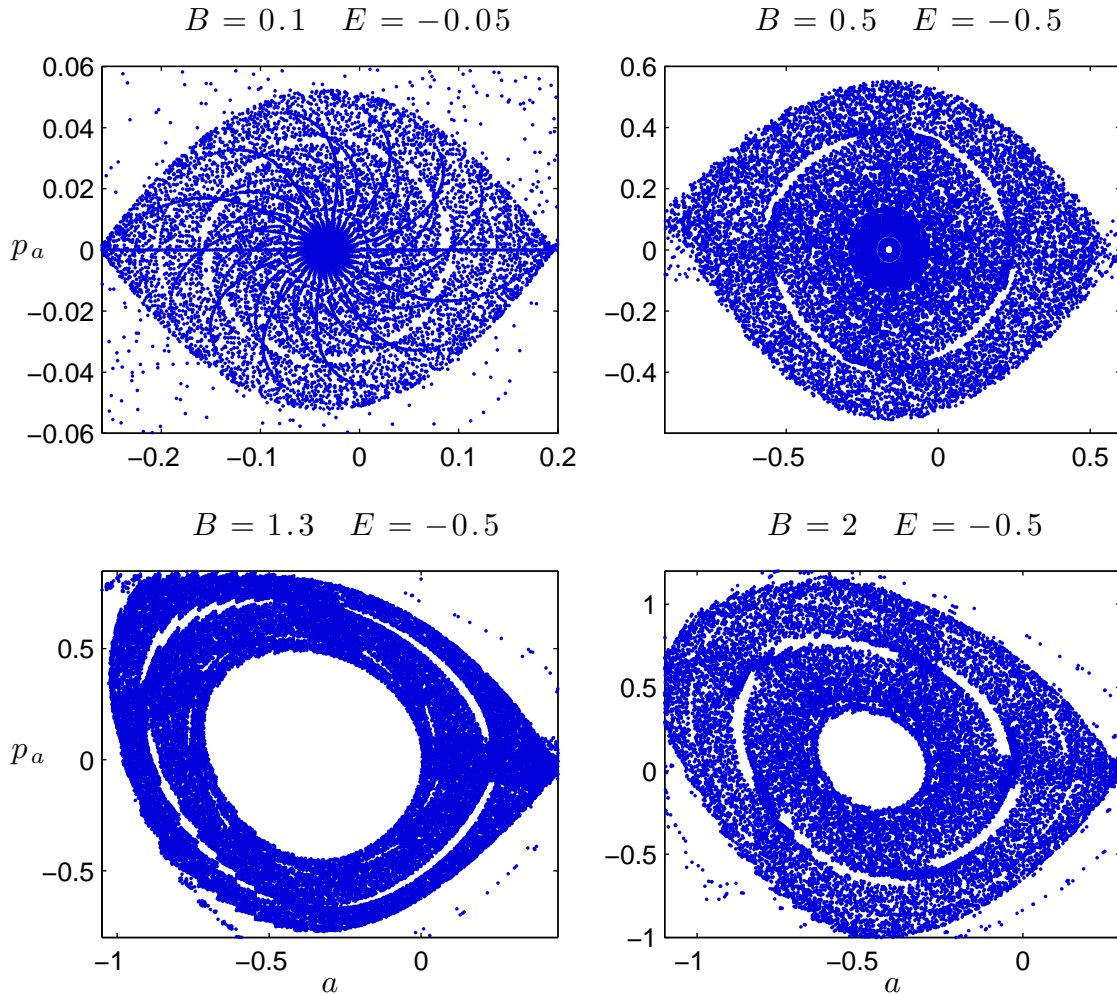


Figure 6.5: A sample of SOS plots for different values of the magnetic field. The values of the magnetic field $B$ and the energy of the starting ensemble $E$ are marked on top of the figures. Electric field $F$ is set to $-1$ in all four figures.

We are now in the position to define a map $(a, p_a) \rightarrow (a', p'_a)$ in the following way. The electron is launched from the surface of section with a given value of momentum, and

evolves under Hamilton's equations until it hits surface of section by crossing from region 1 into region 2, as labeled in Fig. (6.3).

A set of sample SOS plots are shown in Fig. (6.5). Similarly to what we have seen in the kicked Rydberg system, phase space is populated by stable islands immersed in the chaotic sea. The initial conditions were chosen in a way that both the increased density of the points and the void in the point distribution signal the presence of a stable island.

## 6.3   Finding a periodic orbit and its turnstile

The next step in the study of the ionization mechanism in this system is to find the unstable fixed point or unstable periodic orbit whose stable and unstable manifolds
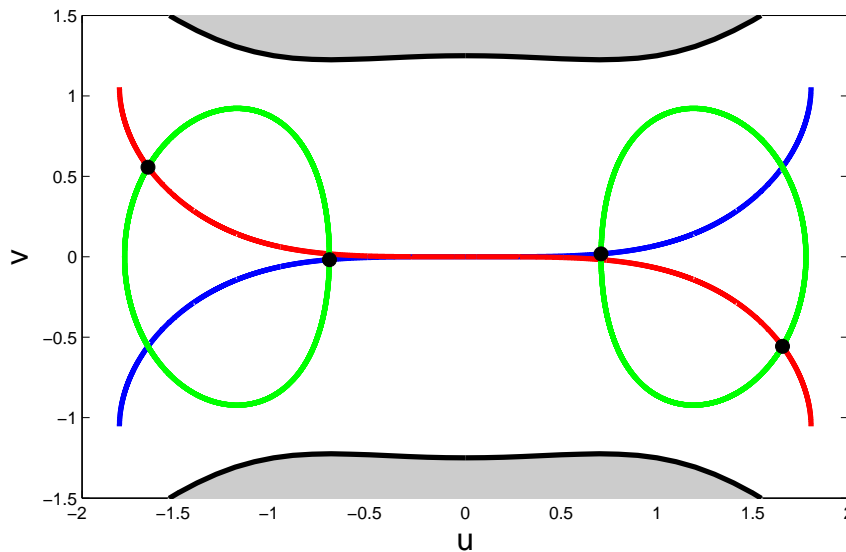


Figure 6.6: An unstable periodic orbit is shown in green. Sets of two big black dots mark the positions of the periodic orbit in the surface of section plot. The thick black line represents the boundary between the energetically allowed (white) and forbidden (shaded) regions.

define the turnstile. Figure (6.6) shows two symmetric periodic orbits in green, along with a curve that defines the surface of section. These periodic orbits form an unstable period two fixed point in the surface of section. Moreover, they define a transition state, meaning that all ionizing trajectories must pass through these orbits.

Figure (6.7) shows a summary of the main results of this section. Two big black dots mark the unstable period two fixed point corresponding to the trajectory shown in Fig. (6.6). Blue lines mark a portion of the unstable manifolds attached to this fixed point, and the red lines represent a portion of the stable manifolds. These stable and unstable
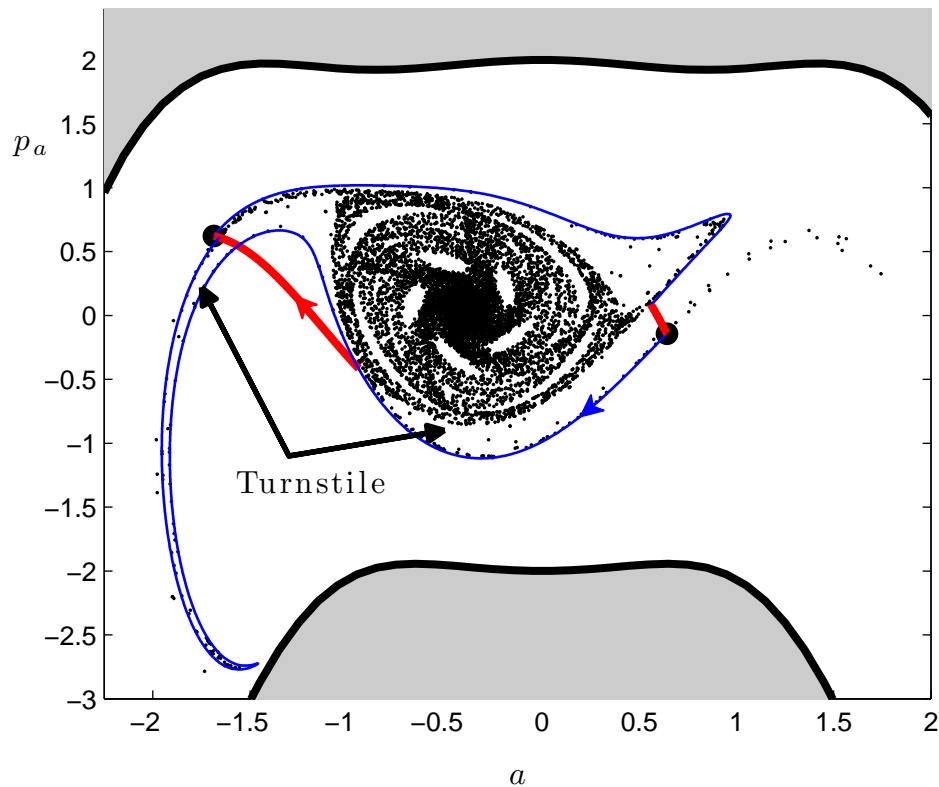


Figure 6.7: Surface of Section for $B = 1.5$, $E = -0.5$. Two big black dots represent the unstable period two orbit. The red line is the portion of the stable manifold, and the blue line is the portion of the unstable manifold. Thick black line defines the boundary between the energetically allowed (white) and forbidden (shaded) regions.
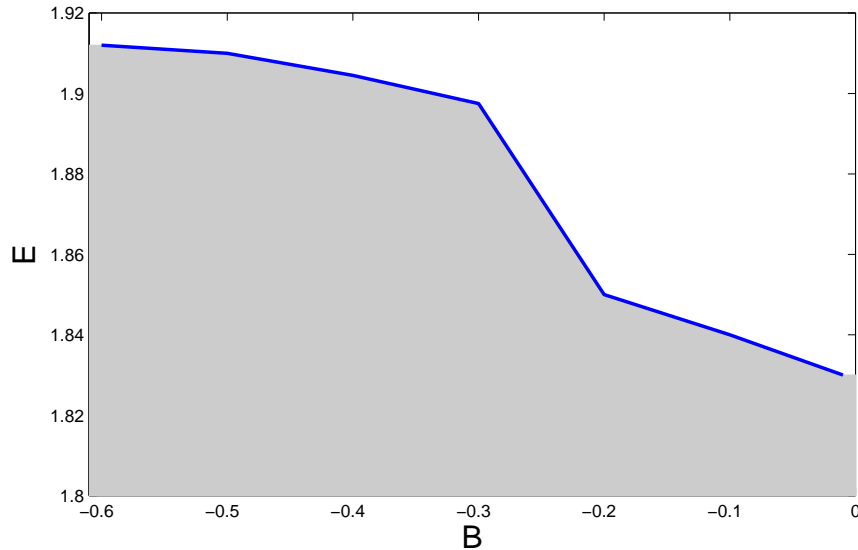
Figure 6.8: The shaded region represents the region in parameter space $(E, B)$ where the SOS definition is valid.

manifolds form a heteroclinic tangle whose turnstile organizes chaotic transport in this system. For clarity, we have labeled a turnstile portion of this heteroclinic tangle. To complete the picture, we have also included additional orbits in black that are contained inside the heteroclinic tangle. You can still notice a chain of prominent stable islands inside this heteroclinic tangle.

As we have mentioned earlier, this is not a global surface of section, rather it is valid only for a certain range of magnetic field strength and energy values. The region of validity in $(E, B)$ parameter space is shown in Fig. (6.8). The position of the boundary is determined in the following way. For a fixed value of energy increase in the magnetic field strength decreases the range of $a$ coordinate in our surface of section by decreasing the Larmor radius of a trajectory we use to define our return map. At the same time the unstable fixed period two point moves away from the nucleus and hence it increases
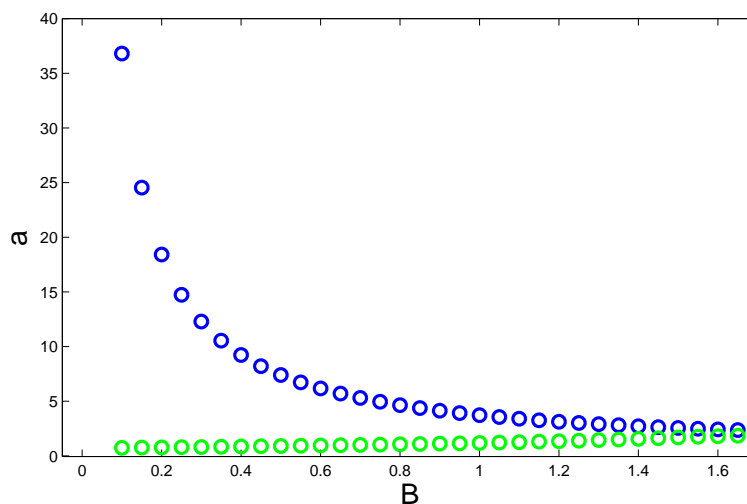
Figure 6.9: The blue data represents the value of $a$ at the edge of the surface of section, and the green data represents the largest of the two absolute $a$ values for a periodic orbit. ($E = -0.5$)

its $a$ coordinate, until it finally slips off the surface of section. Figure (6.9) shows this dependance of the position of the periodic orbit and the edge of the SOS definition on the magnetic field strength $B$. For a critical value of the magnetic field strength, the periodic orbit falls off the surface of section, and our approach breaks down. This happens at the value of B for which the blue and the green curves meet in Fig. (6.9). For $E = -0.5$ this failure occurs at $B = 1.91$.

Even though this approach fails for large magnetic field values, it still offers a valuable insight into chaotic transport in this system.

## 6.4    Extending the definition of SOS

The main reason why our definition for SOS from the previous section fails is because of the self intersecting nature of the trajectories in the $(u, v)$ space. The criterion

for the trajectory we use to define the SOS to self intersect when projected onto physical $(x, y)$ space (and for that matter the parabolic $(u, v)$ space) is that there exists a point along a trajectory where $v_x < 0$. Before we move on, let us quickly review the motion of a charged particle in perpendicular electric and magnetic fields. For a negatively charged particle with magnetic field oriented in positive $\hat{z}$ direction, and electric force $F$ oriented in positive $\hat{y}$ direction (electric field is pointing in negative $\hat{y}$ direction), we have

$$\frac{d\vec{v}}{dt} = \vec{F} - \vec{v} \times \vec{B}.$$

Hence,

$$v_x(t) = v_\perp \sin(Bt) + \frac{F}{B} \qquad \text{and} \qquad v_y(t) = v_\perp \cos(Bt),$$

assuming that at $t = 0$, $v_x = F/B$ and $v_y = v_\perp$. $x$ and $y$ are then equal to

$$x(t) = -\frac{v_\perp}{B} \cos(Bt) + \frac{F}{B} t + const. \qquad \text{and} \qquad y(t) = \frac{v_\perp}{B} \sin(Bt) + const.$$

Thus, the self intersections in $(x, y)$ space occur whenever $v_\perp < F/B$, or in terms of energy, when

$$E < \frac{F^2}{B^2}. \tag{6.12}$$

The idea for this section is to find a different coordinate representation of the same orbit we used to define the SOS in the previous section. The only requirement for the new pair of coordinates is that the orbit used to define the SOS has no self intersections when projected onto the space defined by these new coordinates. The two coordinate pair candidates for defining the space onto which we are going to project the orbit used to define the SOS are $(y, v_x)$, and $(x, v_y)$. In order to test the existence of self intersections

in $(y, v_x)$ space, we set $(y(t_1), v_x(t_1)) = (y(t_2), v_x(t_2))$.

$$\frac{v_\perp}{B} \sin(Bt_1) = \frac{v_\perp}{B} \sin(Bt_2)$$

$$v_\perp \sin(Bt_1) + \frac{F}{B} = v_\perp \sin(Bt_2) + \frac{F}{B},$$

which results in

$$t_1 = 2n\pi t_2.$$

Hence, we conclude that a trajectory projected onto the $(y, v_x)$ space always self intersects.

We now perform the same quick analysis for the projection onto $(x, v_y)$ space, so we set $(x(t_1), v_y(t_1)) = (x(t_2), v_y(t_2))$.

$$-\frac{v_\perp}{B} \cos(Bt_1) + \frac{F}{B}t_1 = -\frac{v_\perp}{B} \cos(Bt_2) + \frac{F}{B}t_2$$

$$v_\perp \cos(Bt_1) = v_\perp \cos(Bt_2),$$

which leads us to conclude that a trajectory projected onto the $(x, v_y)$ space never self intersects.

Figure (6.10) shows a trajectory used to define a SOS projected onto the $(x, p_y)$ space. Even though the value of the magnetic field is well past the boundary determined in the previous section, the trajectory does not self intersect, and this choice proves to be a good candidate for defining the SOS. However, more work needs to be done to produce a figure equivalent to Fig. (6.7) in these coordinates.

For the hydrogen atom in applied perpendicular electric and magnetic felds, we have presented a novel prescription for designing a surface of section upon which the dynamics is continuous and tangencies are avoided. Even though this is not a global surface
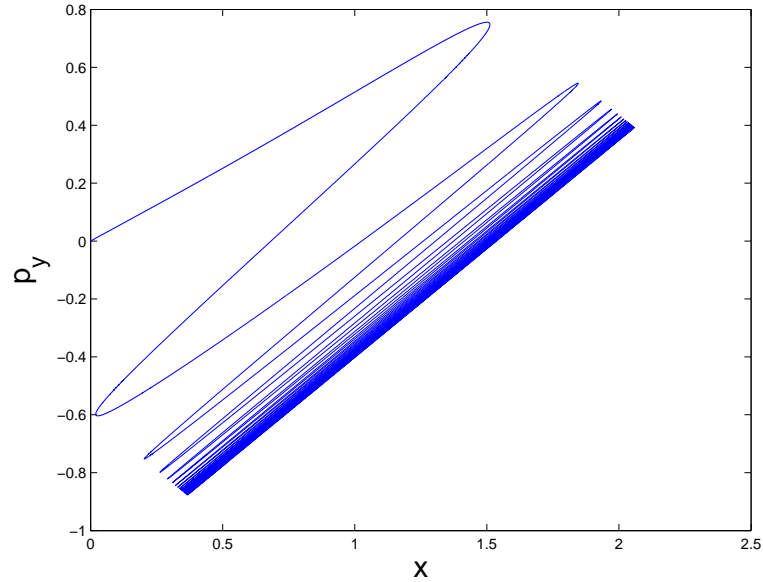
Figure 6.10: Trajectory defining the SOS in $(x, p_y)$ coordinates. $E = -0.5$, and $B = 2.25$

of section, it includes all of the important dynamics in the interaction region, including the unstable periodic orbit and its stable and unstable manifolds, which together form the heteroclinic tangle. This is very important because the ionization process is governed by the geometry of the heteroclinic tangle and its associated phase space turnstile. This work thus lays the foundation for future applications exploiting the turnstile approach to ionization.

# Bibliography

[1] F B Dunning ans J J Mestayer, C O Reinhold, S Yoshida, and J Burgdörfer. Engineering atomic rydberg states with pulsed electric fields. *J. Phys. B: At. Mol. Opt. Phys.*, 42:022001, 2009.

[2] J. E. Bayfield and P. M. Koch. Multiphoton ionization of highly excited hydrogen atoms. *Phys. Rev. Lett.*, 33(5):258–261, 1974.

[3] James E. Bayfield, Larry D. Gardner, and Peter M. Koch. Observation of resonances in the microwave-stimulated multiphoton excitation and ionization of highly excited hydrogen atoms. *Phys. Rev. Lett.*, 39(2):76–79, 1977.

[4] R. Blümel and W. P. Reinhardt. *Chaos in Atomic Physics*. Cambridge University Press, Cambridge, England, 1997.

[5] Pieter Collins. Dynamics forced by surface trellises. In *Contemporary Mathematics: Geometry and Topology in Dynamics*, page 6586. American Mathematical Society, Providence, RI, 1999.

[6] Pieter Collins. Symbolic dynamics from homoclinic tangles. *I. J. Bifurcation and Chaos*, 12(3):605, 2002.

[7] Pieter Collins. *Dyn. Syst.*, 19:1, 2004.

[8] Pieter Collins. *Dyn. Syst.*, 20:369, 2005.

[9] Pieter Collins. Forcing relations for homoclinic orbits of the smale horseshoe map. *Experimental Mathematics*, 14(1):75–86, 2005.

[10] Pieter Collins and Bernd Krauskopf. Entropy and bifurcations in a chaotic laser. *Phys. Rev. E*, 66(5):056201, 2002.

[11] Michael Courtney and Daniel Kleppner. Core-induced chaos in diamagnetic lithium. *Phys. Rev. A*, 53(1):178–191, 1996.

[12] R.H. Cushman and D.A. Sadovskií. Monodromy in the hydrogen atom in crossed fields. *Physica D: Nonlinear Phenomena*, 142(1-2):166–196, 2000.

[13] Michael J. Davis. Bottlenecks to intramolecular energy transfer and the calculation of relaxation rates. *J. Chem. Phys.*, 83:1016, 1985.

[14] Michael J. Davis and Robert E. Wyatt. Surface-of-section analysis in the classical theory of multiphoton absorption. *Chemical Physics Letters*, 86(3):235 – 241, 1982.

[15] M. L. Du and J. B. Delos. Effect of closed classical orbits on quantum spectra: Ionization of atoms in a magnetic field. i. physical picture and calculations. *Phys. Rev. A*, 38(4):1896–1912, 1988.

[16] F. B. Dunning, J. C. Lancaster, C. O. Reinhold, S. Yoshida, and J. Burgdörfer. The kicked rydberg atom. *Adv. At. Mol. Opt. Phys*, 52:49, 2005.

[17] Robert W. Easton. Trellises formed by stable and unstable manifolds in the plane. *Trans. Amer. Math. Soc.*, 294:719–732, 1986.

[18] Eugen Flöthmann and Karl H. Welge. Crossed-field hydrogen atom and the three-body sun-earth-moon problem. *Phys. Rev. A*, 54(3):1884–1888, 1996.

[19] J. Gao, J. B. Delos, and M. Baruch. Closed-orbit theory of oscillations in atomic photoabsorption cross sections in a strong electric field. i. comparison between theory and experiments on hydrogen and sodium above threshold. *Phys. Rev. A*, 46(3):1449–1454, 1992.

[20] Stephan Gekle, Jörg Main, Thomas Bartsch, and T. Uzer. Hydrogen atom in crossed electric and magnetic fields: Phase space topology and torus quantization via periodic orbits. *Phys. Rev. A*, 75(2):023406, 2007.

[21] J. Guckenheimer and P. Holmes. *Nonlinear Oscillations, Dynamical Systems, and Bifurcations of Vector Fields.* Springer-Verlag, New York, 2002.

[22] Paul Hansen, Kevin A. Mitchell, and John B. Delos. Escape of trajectories from a vase-shaped cavity. *Phys. Rev. E*, 73(6):066226, 2006.

[23] Charles Jaffé, D. Farrelly, and T. Uzer. Transition state theory without time-reversal symmetry: Chaotic ionization of the hydrogen atom. *Phys. Rev. Lett.*, 84(4):610–613, 2000.

[24] R. V. Jensen, S. M. Susskind, and M. M. Sanders. Chaotic ionization of highly excited hydrogen atoms: Comparison of classical and quantum theory with experiment. *Physics Reports*, 201(1):1 – 56, 1991.

[25] C. Jung and A. Emmanouilidou. Construction of a natural partition of incomplete horseshoes. *Chaos*, 15:023101, 2005.

[26] P. M. Koch and K. A. H. van Leeuwen. The importance of resonances in microwave "ionization" of excited hydrogen atoms. *Physics Reports*, 255(5-6):289 – 403, 1995.

[27] Tien-Yien Li and James A. Yorke. Period three implies chaos. *The American Mathematical Monthly*, 82(10).

[28] C. Lipp and C. Jung. A degenerate bifurcation to chaotic scattering in a multicentre potential. *J. Phys. A*, 28:6887, 1995.

[29] R.S. Mackay, J.D. Meiss, and I.C. Percival. Transport in hamiltonian systems. *Physica D: Nonlinear Phenomena*, 13(1-2):55 – 81, 1984.

[30] V. K. Melnikov. On the stability of the center for time periodic perturbations. *Trans. Mosc. Math. Soc.*, 12:1–57, 1963.

[31] J. J. Mestayer, W. Zhao, J. C. Lancaster, F. B. Dunning, C. O. Reinhold, S. Yoshida, and J. Burgdörfer. Transporting rydberg electron wave packets with chirped trains of pulses. *Phys. Rev. Lett.*, 99(18):183003, 2007.

[32] Davis Michael J and Stephen K. Gray. Unimolecular reactions and phase space bottlenecks. *J. Chem. Phys.*, 84:5389, 1986.

[33] K. A. Mitchell, J. P. Handley, J. B. Delos, and S. K. Knudson. Geometry and topology of escape. ii. homotopic lobe dynamics. *Chaos*, 13(3):892, 2003.

[34] K. A. Mitchell, J. P. Handley, B. Tighe, A. Flower, and J. B. Delos. Analysis of chaos-induced pulse trains in the ionization of hydrogen. *Phys. Rev. A*, 70(4):043407, 2004.

[35] K. A. Mitchell, J. P. Handley, B. Tighe, A. Flower, and J. B. Delos. Chaos-induced pulse trains in the ionization of hydrogen. *Phys. Rev. Lett.*, 92(7):073001, 2004.

[36] K. A. Mitchell, J. P. Handley, B. Tighe, S. K. Knudson, and J. B. Delos. Geometry and topology of escape. i. epistrophes. *Chaos*, 13(3):880, 2003.

[37] Kevin A. Mitchell. The topology of nested homoclinic and heteroclinic tangles. *Physica D: Nonlinear Phenomena*, 238(7):737–763, 2009.

[38] Kevin A. Mitchell and John B. Delos. The structure of ionizing electron trajectories for hydrogen in parallel fields. *Physica D*, 229:9–21, 2007.

[39] C. O. Reinhold, S. Yoshida, J. Burgdörfer, W. Zhao, J. J. Mestayer, J. C. Lancaster, and F. B. Dunning. Realization of the kicked atom at high scaled frequencies. *Phys. Rev. A*, 73(3):033420, 2006.

[40] V. Rom-Kedar. Transport rates of a class of two-dimensional maps and flows. *Physica D: Nonlinear Phenomena*, 43:229–268, 1990.

[41] V. Rom-Kedar. Homoclinic tangles - classification and applications. *Nonlinearity*, 7:441–473, 1994.

[42] B. Rückerl and C. Jung. Hierarchical structure in the chaotic scattering off a magnetic dipole. *J. Phys. A*, 27:6741, 1994.

[43] B. Rückerl and C. Jung. Scaling properties of a scattering system with an incomplete horseshoe. *J. Phys. A*, 27:55, 1994.

[44] Christopher R. Schleif and John B. Delos. Monodromy and the structure of the energy spectrum of hydrogen in near perpendicular electric and magnetic fields. *Phys. Rev. A*, 76(1):013404, 2007.

[45] C. L. Stokely, J. C. Lancaster, F. B. Dunning, D. G. Arbó, C. O. Reinhold, and J. Burgdörfer. Production of quasi-one-dimensional very-high-n rydberg atoms. *Phys. Rev. A*, 67(1):013403, 2003.

[46] B. E. Tannian, C. L. Stokely, F. B. Dunning, C. O. Reinhold, S. Yoshida, and J. Burgdörfer. Kicked rydberg atom: Response to trains of unidirectional and bidirectional impulses. *Phys. Rev. A*, 62(4):043402, 2000.

[47] A. Tiyapan and C. Jaffé. Classical atomdiatom scattering: Self?similarity, scaling laws, and renormalization. *J. Chem. Phys.*, 99:2765, 1993.

[48] A. Tiyapan and C. Jaffé. Classical s?matrix theory for chaotic atomdiatom collisions. *J. Chem. Phys.*, 101:10393, 1994.

[49] A. Tiyapan and C. Jaffé. Chaotic scattering: An invariant fractal tiling of phase space. *J. Chem. Phys.*, 101:5499, 1995.

[50] G. Wiebusch, J. Main, K. Krüger, H. Rottke, A. Holle, and K. H. Welge. Hydrogen atom in crossed magnetic and electric fields. *Phys. Rev. Lett.*, 62(24):2821–2824, 1989.

[51] S. Wiggins. *Chaotic Transport in Dynamical Systems*. Springer-Verlag, New York, 1992.

[52] S. Yoshida, C. O. Reinhold, E. Persson, J. Burgdörfer, and F. B. Dunning. Steering rydberg wave packets using a chirped train of half-cycle pulses. *J. Phys. B*, 38:S209, 2005.

[53] W. Zhao, J. J. Mestayer, J. C. Lancaster, F. B. Dunning, C. O. Reinhold, S. Yoshida, and J. Burgdörfer. Engineering very-high-$n$ polarized rydberg states using tailored half-cycle-pulse sequences. *Phys. Rev. Lett.*, 95(16):163007, 2005.

[54] W. Zhao, J. J. Mestayer, J. C. Lancaster, F. B. Dunning, C. O. Reinhold, S. Yoshida, and J. Burgdörfer. Bidirectionally kicked rydberg atoms: Population trapping near the continuum. *Phys. Rev. A*, 73(1):015401, 2006.

[55] W. Zhao, J. J. Mestayer, J. C. Lancaster, F. B. Dunning, C. O. Reinhold, S. Yoshida, and J. Burgdörfer. Navigating localized wave packets in phase space. *Phys. Rev. Lett.*, 97(25):253003, 2006.

# Appendix A

# Jacobi Elliptic Solutions to

# $\ddot{u} = Eu - 2Fu^3$

Differential equation that appears in the Kicked Rydberg system for the position $u$ in the parabolic coordinates is

$$\ddot{u} = Eu - 2Fu^3, \tag{A.1}$$

where $E$ is the electron energy and $F$ is the kicking force. The solutions to this equation are Jacobi elliptic functions. The type of the function depends on the signs of $E$ and $F$. Thus, we have four different cases to consider. Each of the four sections in this appendix treats one of the cases.

## A.1   $E < 0$ and $F < 0$

The appropriate differential equation to consider in this case is

$$\frac{d^2y}{dx^2} = -\left(1 + k^2\right)y + 2k^2y^3. \tag{A.2}$$

The solution to this equation is of the form $y(x) = A\,\text{sn}(ax + \phi, k)$, where $A$, $a$, and $\phi$ are

constants. Hence

$$\frac{d^2y}{dx^2} = -a^2\left(1 + k^2\right)y + \frac{2a^2k^2}{A^2}y^3. \tag{A.3}$$

We now connect this to our differential equation A.1. Equation A.3 implies that

$$-a^2\left(1 + k^2\right) = E \qquad \text{and} \qquad -F = \frac{a^2k^2}{A^2},$$

resulting in the relationship

$$a^2 = FA^2 - E.$$

We get the other two equations that determine the constants by using

$$A\,\text{sn}(\phi, k) = u_0 \qquad \text{and} \qquad Aa\,\text{cn}(\phi, k)\,\text{dn}(\phi, k) = p_0, \tag{A.4}$$

where $u_0$ and $p_0$ are the initial values of the position and momenta in parabolic coordinates.

Using the identities with Jacobi elliptic functions, we get that the equation for $A$ can be

written as

$$\pm A\sqrt{1 - \frac{u_0^2}{A^2}}\sqrt{FA^2 - E + Fu_0^2} = p_0, \tag{A.5}$$

where the sign depends on the sign of $p_0$. Solving this equation for $A$ allows us to solve

for $a$, as well as for $\phi$.

Once we have full expressions for $u$ and $p$, we have to solve a differential equation

$$\frac{ds}{dt} = \frac{1}{u^2}$$

in order to propagate the electron forward in time. However, inverting the equation for $s$ poses numerical challenges that caused us to abandon this approach in our system. In the remainder of this Appendix we present the solutions for the remaining three sign combinations of $E$ and $F$.

## A.2   $E < 0$ and $F > 0$

The appropriate differential equation to consider in this case is

$$\frac{d^2y}{dx^2} = -\left(1 - 2k^2\right)y - 2k^2y^3. \tag{A.6}$$

The solution to this equation is of the form $y(x) = A\operatorname{cn}(ax + \phi, k)$. Hence

$$\frac{d^2y}{dx^2} = -(1 - 2k^2)a^2y - 2\frac{k^2a^2}{A^2}y^3. \tag{A.7}$$

We repeat the same steps as in the previous section to get

$$a^2 = -E + 2FA^2,$$

$$A\operatorname{cn}(\phi, k) = u_0, \tag{A.8}$$

and

$$\pm A\sqrt{1 - \frac{u_0^2}{A^2}}\sqrt{Fu_0^2 - E + FA^2} = p_0, \tag{A.9}$$

where again the sign depends on the sign on $p_0$.

## A.3    $E > 0$ and $F > 0$

The appropriate equation to consider in this case is

$$\frac{d^2y}{dx^2} = (2 - k^2)y - 2y^3, \tag{A.10}$$

whose solution is of the form $y(x) = A\,\mathrm{dn}(ax + \phi, k)$. Then

$$\frac{d^2y}{dx^2} = a^2(2 - k^2)y - 2\frac{a^2}{A^2}y^3. \tag{A.11}$$

Again, doing the same analysis, we get

$$a^2 = FA^2,$$

$$A\,\mathrm{dn}(\phi, k) = u_0,$$

and

$$\pm A^2\sqrt{F}\sqrt{2 - \frac{E}{FA^2}}\sqrt{1 - \frac{u_0^2}{A^2}}\sqrt{\frac{u_0^2}{A^2} + 1 - \frac{E}{FA^2}} = p_0, \tag{A.12}$$

where the sign depends on the sign of $p_0$.

## A.4    $E > 0$ and $F < 0$

This is the most complicated case of them all. The solution in this case is of the form

$$y = -A\frac{\mathrm{sn}(ax + \phi, k)}{\mathrm{cn}(ax + \phi, k)}.$$

Then

$$\frac{d^2y}{dx^2} = Aa^2\left[(1 + k^2)\frac{y}{A} + 2k^2\frac{y^3}{A^3}\right]. \tag{A.13}$$

This results with

$$a^2 = E + FA^2,$$

$$-A\frac{\text{sn}(\phi, k)}{\text{cn}(\phi, k)} = u_0,$$

and

$$-A\sqrt{E + FA^2}\,\frac{1 - \frac{u_0^2}{E + FA^2}}{\sqrt{1 - \left(1 + \frac{FA^2}{E + FA^2}\right)\frac{u_0^2}{4A^2}\left(2 - 2\sqrt{1 + 4A} + 4A\right)}} = p_0. \qquad (A.14)$$